Development and integration of high throughput detector systems for photon-based diagnostics at Karlsruhe Research Accelerator

Zur Erlangung des akademischen Grades eines

DOKTORS DER INGENIEURWISSENSCHAFTEN (DR. -ING.)

von der Fakultät für Elektrotechnik und Informationstechnik
des Karlsruher Instituts für Technologie (KIT)

genehmigte

DISSERTATION

von

M.Sc. Meghana Mahaveer Patil

geb. in Bangalore

Zusammenfassung

Der Karlsruhe Research Accelerator (KARA) ist ein Elektronen-Speicherring und erzeugt kurze Elektronenpakete, die intensive Strahlung im Terahertz-Bereich (THz) aussenden. Diese Strahlung wird in Pulsen (bursts) emittiert, die durch Fluktuationen und Instabilitäten in der Ladungsverteilung verursacht werden. Eine detaillierte Kenntnis des Energie-Zeit-Phasenraums der Elektronen ist für ein besseres Verständnis des Phänomens und schließlich für eine Kontrolle und Stabilisierung der Erzeugung intensiver THz-Strahlung unerlässlich. Um eine Phasenraumtomographie für jeden Umlauf der Elektronenpakete (electron bunches) zu erhalten, wird eine synchronisierte longitudinale und transversale Strahldiagnostik durchgeführt. Bei der Messung beider Strahlprofile besteht die Herausforderung darin, dass sie in einer Einzelschussmessung (Messung in jedem einzelnen Umlauf ohne Mittelwertbildung) und mit hoher Wiederholrate (2,7 MHz im Single-Bunch-Betrieb bei KARA) erfasst werden müssen. Konventionell werden longitudinale Bunch-Profile mit einem Streak-Kamera-System gemessen. Dabei wird die zeitliche Intensitätsverteilung der Synchrotronstrahlung im sichtbaren Lichtbereich gemessen, indem die zeitliche in eine räumliche Verteilung übertragen wird. Der Port „Visible Light Diagnostics" (VLD) an KARA ist für Experimente zur Strahldiagnostik vorgesehen und mit einer Streak-Kamera und einer „Fast Gated Intensified Camera" ausgestattet. Der VLD-Port ermöglicht die Messung von sichtbarer und ultravioletter Strahlung, die von den im Speicherring zirkulierenden Elektronen erzeugt wird. Während die Streak-Kamera sehr präzise Messungen der gemittelten longitudinalen Bunch-Profile ermöglicht, sind ihre Möglichkeiten für Einzelaufnahmen begrenzt. Dennoch sind diese Messungen für den Vergleich mit anderen Techniken wie der elektro-optischen Abtastung und der Messung von kohärenter Synchrotronstrahlung mit THz-Detektoren unerlässlich.

Für Einzelschussmessungen ist an KARA als erstem und einzigem Elektronen-Speicherring der Welt ein elektro-optischer Bunch-Profil-Monitor installiert worden und in Betrieb. Durch das Einprägen der longitudinalen Elektronenpaket-profilen in gechirpte Laserpulse ist eine Einzelschussdetektion möglich. Die Grenzen der verfügbaren Nachweissysteme stellen jedoch eine Herausforderung dar. Das am KIT entwickelte KALYPSO-System, eine spezielle ultraschnelle Photodetektor-Zeilenkamera, ermöglicht die direkte Detektion von ps-Pulsen bei MHz-Wiederholraten über lange Zeiträume. Die transversale Diagnostik sichtbarer Lichtstrahlen in einem dispersiven Abschnitt in einem Dipolmagneten ermöglicht den Zugang zur Energieausbreitung über die Messung der Synchrotronstrahlungsprofile und damit die Bestimmung der zweiten Achse des Phasenraums. Gegenwärtig wird eine verstärkte schnelle Gate-Kamera verwendet, um das horizontale Strahlprofil zu erfassen, indem ein schnelles optisches Gate zur Aktivierung eines Bildverstärkers verwendet wird. Um die zeitliche Entwicklung des Strahlprofils zu erfassen, wird das horizontale Strahlprofil durch einen rotierenden Spiegel auf dem Sensor der Kamera verschoben. Diese Messung ist jedoch durch die Drehung des Spiegels und die Größe des Detektors limitiert (und damit ist die Anzahl der aufeinanderfolgenden Profile begrenzt). Um diese Einschränkung zu überwinden und die horizontalen Profile mit hoher Wiederholungsrate und über lange Zeiträume zu messen, wird ein neuer Ansatz mit KALYPSO verfolgt. Die derzeitige Version der KALYPSO-Platine mit Si-Sensoren ermöglicht die Erfassung im sichtbaren Bereich, und erste Tests damit haben gezeigt, dass horizontale Strahlprofile am VLD-Port erfasst werden können. Für präzise Messungen in dieser neuen Anwendung waren jedoch erhebliche Verbesserungen der Elektronik und des optischen Aufbaus erforderlich.

Ein Schwerpunkt der Dissertation ist einerseits ein zukünftiges KALYPSO-System für die Messung von horizontalen Einzelschussprofilen mit hoher Wiederholrate am Speicherring KARA. Zum anderen konzentriert sich die Dissertation auf das Design, die Auslegung und die Charakterisierung eines neuen Photodetektor-Arrays mit Low-Gain Avalanche Detectors (LGAD). Diese neuartigen Sensoren werden für räumliche und zeitliche Auflösungen von Mikrometern bzw. Nanosekunden optimiert. Um alle analogen Signale des LGAD-Sensors zu erfassen

und zu verarbeiten, ist ein leistungsfähiger Front-End-Elektronik-ASIC erforderlich. Ein weiteres Thema der Doktorarbeit ist daher der Entwurf und das Layout eines analogen Front-End-Auslese-ASICs, um die schnellen Impulse zu verarbeiten, die von LGAD-Sensoren mit hoher Bildrate und für lange Zeitskalen erzeugt werden. Die Ergebnisse dieser Dissertation führen zu neuartigen Sensoren, Front-End-Elektronik und der Integration des neuen Systems in die sichtbare Synchrotronstrahlungsdiagnostik. Eine Überprüfung zwischen den klassischen Methoden (Streak-Kamera und Fast-Gated-Intensified-Kamera) und den neuen Detektoren ist für eine fundierte Bewertung unerlässlich und daher ein weiteres Ziel. Eine zentrale Herausforderung für die Phasenraumtomographie von Elektronenpaketen liegt in der Synchronisation mit Pikosekunden-Genauigkeit der verschiedenen Messverfahren. Hier ist der Einsatz der KALYPSO-Technologie für beide Arten von Messungen von Vorteil, dennoch ist die Synchronisation anspruchsvoll, da die Messplätze räumlich voneinander getrennt sind: Die EO Messungen (Electro Optic) finden in der Vakuumröhre bzw. deren Analyse im EO-Labor statt, während am VLD-Port die emittierte Synchrotronstrahlung gemessen wird. In dieser Arbeit wird ein präzises Zeitsynchronisationssystem für die verschiedenen Experimentierstationen unter Verwendung von FPGA-Logik und speziellen optischen Referenzsignalen entwickelt. Ebenso wichtig ist die Analyse der gesammelten synchronisierten Daten.

Acknowledgement

I would like to thank Prof. Dr. Marc Weber for being my supervisor and giving me insight and support throughout the writing of this thesis.

I would like to express my utmost gratitude to Prof. Dr. Anke-Susanne Müller for welcoming me into the THz group and supporting me through my doctoral studies.

I would like to express my deepest gratitude to Dr. Erik Bründermann, you have been my supporter throughout these years, thank you.

Needless to say, one person without whom this thesis would not have been possible, is Dr. Michele Caselle. The door to Michele's office has always been open when I had trouble getting things to work. He would work next to me until we fixed the problem. Thank you for your support.

To Dr. Gudrun Niehues, I can't express how thankful I am for your support and patience. You have always helped me with basically everything I needed throughout this thesis both technical and bureaucratic stuff.

To Dr. Johannes Steinmann, my office mate, for proofreading this thesis and always clarifying my accelerator physics doubts, thank you.

Special thanks to Pia Steck, for readily helping me with all the numerous KALYP-SOs we wire-bonded.

To all my THz group and IPE colleagues, thank you for being there!

To Ole, you were my biggest support, both emotionally and sometimes with my Python problems. Thank you so much for proofreading the thesis in one sitting so that I could make the deadline.

And lastly, my parents, who are 7400 km away from me, made sure I was fine every week and encouraged me endlessly to pursue what I wished for. Thank you, Amma, Appa.

Contents

1   Introduction

When a charged particle such as an electron is accelerated, electromagnetic (EM) radiation is produced. The radiation thus produced is called synchrotron radiation (SR). The SR can be tuned in energy, wavelength, intensity, and pulse length. This allows the radiation to be used in various applications related to material science, biology, physics, chemistry, medicine etc.[1, 2].

The SR is obtained by the superposition of the radiation emitted by a group of individual electrons (electron bunch). The emitted radiation becomes coherent when it is longer than the RMS electron bunch length. The intensity of this coherent radiation is quadratically proportional to the number of electrons in the bunch. The coherent nature of SR can be generated by squeezing the bunches below one picosecond bunch length. This SR, a part of the electromagnetic spectrum, lies between visible light and microwaves from 0.3 to 3 THz. The THz radiation has become an exciting and popular source for applications as diverse as spectroscopy and wireless communication. Accelerators have a huge advantage as THz sources due to their capability to generate highly brilliant pulsed THz radiation with a high repetition rate in comparison to commercial THz sources.

Emission of *coherent THz radiation* in a synchrotron occurs during a short bunch operation mode, i. e. a bunch length of a few picoseconds with a certain unstable behaviour of the bunches. The unstable behavior occurs when the radiation emitted interacts with the Coulomb field of the electron bunch [3, 4]. This 'self-interaction' is often characterized by the formation of microstructures on the longitudinal phase-space of the electron bunch. This behaviour is often referred to as micro-bunching instability (MBI) [5, 6, 7, 8, 9].

The bunch's energy spread and longitudinal phase space (energy and phase) distribution are vital parameters to describe and analyze the micro-bunching instability. Energy spread studies are performed by investigating the horizontal bunch size of the electron bunch as it is coupled to the energy spread in a dispersive section of the accelerator [10]. The evolution of the longitudinal phase space can be studied by various methods, including electro-optic detection techniques. These methods allow for precise time-resolved measurements of the emitted radiation [12, 11].

These *diagnostic methods* state the requirements for detecting microbunching instability and in turn, studying the Thz emission. The diagnostic methods for the above-mentioned measurements use a line array camera as the final detector. The main limitation, posed at several accelerator facilities, is the performance of this line camera. Commercially available line cameras [90, 89, 91, 92] have several disadvantages, a few of them being low acquisition rate, sensitivity, sample sizes, etc. Hence a custom-designed line camera is the best solution.

As a part of this thesis, two new versions of the previously existing line camera KA-LYPSO - KArlsruhe Linear arraY detector for MHz rePetition-rate SpectrOscopy have been developed. This thesis aims to provide a system capable of working at MHz framerates, wide dynamic range and relatively low noise.

The main parameters/specifications the line cameras should meet to qualify for accelerator diagnostics are described below:

- **Acquisition rate**: Particle accelerators operate with repetition rates in the MHz regime. For example, the repetition rate of the electron bunches in single bunch mode at KARA is 2.7 MHz. In a multi-bunch environment, the rate can vary from tens to hundreds of MHz.

- **Spatial resolution**: The EO method for longitudinal bunch profile measurement, converts timing information into spatial information using a spectrometer. A line scan detector with a pitch of at least 50 m and, at best, 25 m is necessary to reach a ps-fs resolution.

- **Noise requirement**: The intensity of the visible light radiation emitted to study energy spread studies is relatively low during single bunch mode and at the detector's noise performance limit.

- **Dynamic range**: The capability of measuring radiation at extremely low and high currents is necessary for analyzing the evolution of electron bunch dynamics.

- **Data acquisition and processing**: The line camera must be able to stream the data continuously for hours to study the dynamic changes in the electron bunch. This results in several Gb/s of data that must be streamed/saved on the local memory devices.

The following topics form the central part of the author's thesis:

- **Development of advanced sensors based on LGAD**: LGADs (Low Gain Avalanche Detectors) are PN-junction diodes with an additional doped implant. These diodes thereby provide an internal gain as well as improved timing resolution. *Chapter 4* will provide more insight into the design, simulation, and performance evaluation of such a sensor.

- **System Integration**: Developing the line camera KALYPSO involves several stages, including designing and fabricating the PCB (Printed Circuit Board), choosing the sensor, and its interconnection with the ASIC. Clock and data flow planning, firmware development, and finally, software for the user interface. *Chapter 5* will explain these various components in detail.

- **Experiment integration and results**: The systems developed under this thesis have been tested and evaluated for performance at KARA, the Karlsruhe Research Accelerator. Three experimental beamlines dedicated to studying longitudinal bunch profiles using EOSD, studying energy spread of bunch using horizontal bunch profile measurement, and measurement of THz pulses using EO far-field method, have been used as benchmark experiments for the first experimental data evaluation. *Chapter 6* will explain these setups, the integration of KALYPSO at these stations, and the results acquired during the short bunch operation at KARA.

2 Beam diagnostics at KARA

This chapter discusses various beam diagnostics methods implemented or planned for resolving dynamics in ultra-short electron bunches at KARA. Beam diagnostics at a research accelerator like KARA refer to the measurement and analysis of the properties of a particle beam as it travels through the accelerator. These measurements can be used to optimize the accelerator's performance and study the underlying bunch dynamics or instabilities or even control them.

2.1 KARA

The Karlsruhe Research Accelerator (KARA) is an accelerator test facility and synchrotron light source at the Karlsruhe Institute of Technology.

KARA consists of a storage ring with a circumference of 110.4 m. It can store electrons at an energy of up to 2.5 GeV. This is achieved by an *electron gun* that accelerates electrons to an energy of 90 keV. These electrons then pass through a linear accelerator (Linac) placed between two dipole magnets in the *racetrack microtron* until they reach an energy of 53 MeV. Then at the *booster synchrotron*, the final energy of 1.3 GeV is reached. The three stages described above are known as the *pre-accelerator*.

In the main KARA storage ring electron bunches are injected from the pre-accelerator. The 40 quadrupole magnets focus the electron bunches after being deflected by 16 dipole magnets. The radio frequency (RF) system consists of two cavities and is used to accelerate the electrons longitudinally with a frequency of roughly 500 MHz. A compact list of parameters of KARA is shown in table 2.1.

Figure 2.1: CAD drawing of the KARA storage ring. The storage ring consists of 16 dipole magnets (yellow) used for deflecting the electron bunches and 40 quadrupole magnets (brown) to focus the electron bunches. Image courtesy: Ursula Herberger.

KARA is focused on research and development in particle acceleration and radiation sources, particularly emphasising terahertz (THz) radiation [13, 14]. THz radiation has a frequency range from 0.3 to 3 THz (far IR). It has a variety of potential applications, including imaging, spectroscopy, and communication. Laser-based THz sources are a method to generate intense THz radiation. However, these methods are often limited by their repetition rate, tunability and control [15]. THz radiation generated by an accelerator can have several advantages:

- High power: Accelerators can generate extremely high-power THz radiation.

- High brilliance: The high brilliance of accelerator-generated THz radiation makes it possible to use it for applications requiring a high-resolution level, such as imaging.

circumference	110.4 m
beam energy	0.5 GeV to 2.5 GeV
beam current	up to 200 mA
RF frequency	499.74 MHz
harmonic number	184
revolution time	368.2 ns

Table 2.1: Overview of the main parameters concerning the operation regimes at KARA. The circumference is the total length through the vacuum beam pipe. The beam energy is the final energy the accelerated electrons achieve; the harmonic number is total the number of consecutive electron bunches that can be stored in the storage ring. Revolution time is the time one bunch needs to make a complete traverse of the circumference once.

- Versatility: Accelerators can generate THz radiation with various pulse shapes and durations.

Overall, using an accelerator to generate THz radiation offers several advantages in power, frequency, brilliance, and versatility. The following section briefly explains how accelerator-based THz radiation is generated.

2.2 Synchrotron radiation

Deflection of highly relativistic particles, such as electrons in accelerators due to the bending magnets, leads to the emission of Synchrotron radiation (SR), see Fig. 2.2. The emitted SR has a broad spectrum ranging from X-rays to infrared (IR) [16].

KARA can operate in several operating energy modes, including short bunch operation (In this thesis, measurements were performed at final working energy of 1.3 GeV). The longitudinal (direction of travel) bunch length σ_z is squeezed to a few picoseconds during this mode of operation [17]. This operating condition is also called *low-α_c mode*, derived from the momentum compaction factor α_c. The bunch length σ_z is proportional to the square root of α_c and the RF voltage V_{RF}.
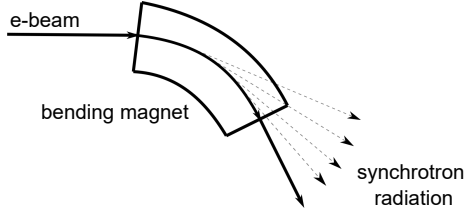
Figure 2.2: Illustration of a radiation cone generated by an electron beam when it travels along a bending magnet.

For highly relativistic particles, the relation between bunch length and momentum compaction factor is given by

$$\sigma_z = \frac{c\sigma_\delta \mid \alpha_c \mid}{2\pi f_s} = \frac{c}{\sqrt{2\pi} f_{rev}} \sqrt{\frac{\alpha_c E_0}{heV_{RF}}} \sigma_\delta \tag{2.1}$$

The momentum compaction factor α_c is given by

$$\alpha_c = \frac{1}{L} \int \frac{D(x)}{R(x)} dx \tag{2.2}$$

where σ_δ is the relative energy spread of the bunch given by $\frac{\sigma_E}{E_0}$, σ_E is the rms energy spread, f_s the synchrotron frequency, f_{rev} is the revolution frequency, E_0 is the electron energy, V_{RF} the RF voltage, h is the harmonic number, L is the circumference of the storage ring, D is the dispersion, and R is the bending radius.
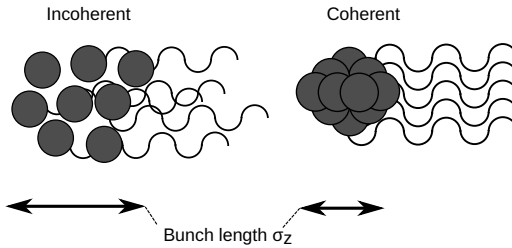

Figure 2.3: Depiction of the relationship between bunch length and the emitted synchrotron radiation.

The emitted SR contains two components the *coherent synchrotron radiation (CSR)* and *incoherent synchrotron radiation (ISR)*. The ISR component of the radiation is linearly proportional to the number of electrons in the bunch (N_e) and depends only on the bending radius and electron energy. On the other hand, the CSR component relies on the square of the number of electrons in the bunch (N_e^2); hence, the emitted CSR power is significantly higher than that of ISR.

From [18], the power spectral density of the SR emitted by a bunch of N_e ultra-relativistic electrons is given by

$$P(\omega) = (N_e + N_e(N_e - 1)F(\omega))P_e(\omega) \tag{2.3}$$

where $N_e \cdot P_e(\omega)$ is the incoherent part and $N_e{}^2 F(\omega) \cdot P_e(\omega)$ is the coherent part of the total spectral intensity of the synchrotron radiation emitted, $P_e(\omega)$ is the radiation power of a single electron. One additional factor the CSR depends on is the form factor $F(\omega)$, which in turn depends on the bunch length. It can be approximated close to 1 for wavelengths much higher than the bunch lengths.

Figure 2.4 shows the distribution of coherent synchrotron (CSR) and incoherent synchrotron (ISR) radiation spectrum. The CSR intensity of short electron bunches is orders of magnitudes higher than the ISR intensity.

In an accelerator, the emitted SR has a self-interaction with the Coulomb field of the electron bunch, which is characterized by the formation of small-scale fluctuations or 'microbunches' in the longitudinal phase space of the electron bunch. This phenomenon, also known as *microbunching instability*, has, in turn, an effect on the emitted CSR, leading to a fluctuating THz radiation emission as seen in Fig. 2.5. These microstructures can be visualized in simulations as well as experimentally. One example simulation performed using the Vlasov-Fokker-Planck solver INOVESA [19] can be seen in Fig. 2.6, which shows the formation of the microbunches. It can hence concur that the formation and damping of the substructures cause the sawtooth bursting of the THz radiation.
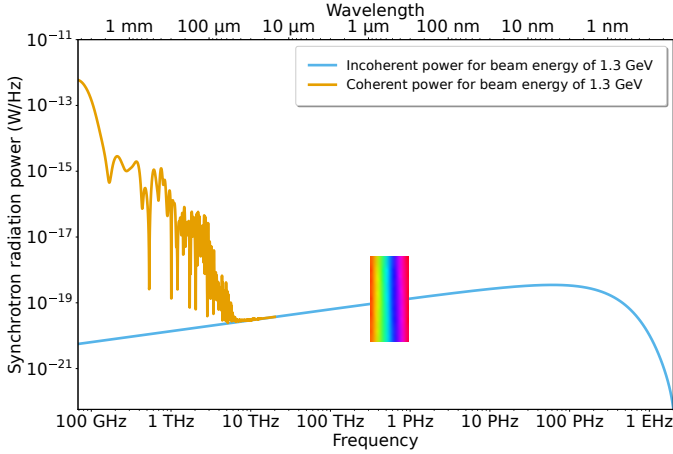
Figure 2.4: Synchrotron radiation power spectrum for a beam energy of 1.3 GeV. The CSR power (yellow) is calculated based on the bunch profile measured, and the blue plot gives the ISR power. The emitted radiation corresponding to the visible region of the spectrum is highlighted with the rainbow. Data courtesy: J. L. Steinmann.

For the radiation to be suitable for user experiments, it is necessary to control the fluctuations in the emission of THz radiation. Hence, studying and understanding the beam dynamics of short electron bunches is important. The study of microbunching instability poses several timing and resolution requirements, namely,

- Sub-ps resolution: it is necessary to resolve the microbunches in the longitudinal bunch profile.

- MHz repetition rate: is necessary to resolve every bunch when operating in single bunch mode. The revolution period of the electron bunch at KARA is 368 ns. The diagnostic must operate at least 2.7 MHz to study every bunch.

- Long acquisition period: it is necessary to study slow changes in beam dynamics over the beam current decay, especially in the bursting regime, which could last for a few hours.
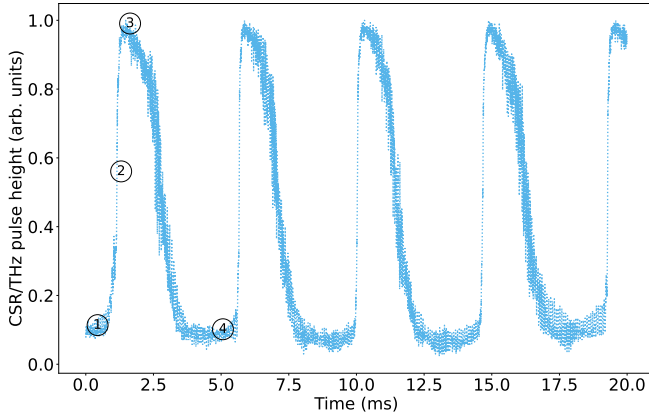
Figure 2.5: THz radiation measured using a Schottky diode at a bunch current of 1.5 mA. The typical sawtooth bursting pattern of the THz intensity can be seen. To understand the bursting behaviour, the marked positions are linked to an example of the stimulation of a bunch profile in Fig 2.6. Data courtesy: J. L. Steinmann.

- Single-shot: it is necessary to resolve single bunch characteristics with good SNR without averaging.

- Synchronized operation: must be implemented for several diagnostics which study the different 'dimensions' of the electron beam. Synchronized measurements make correlating the occurring dynamics at different diagnostic stations much easier.

- Feedback: it is necessary to apply inference signals on the accelerator once the underlying beam dynamics are studied to control the instabilities or to improve the operation efficiency.

The primary electron beam diagnostics that fulfil the above requirements for resolving microbunching instabilities are introduced in the following sections.
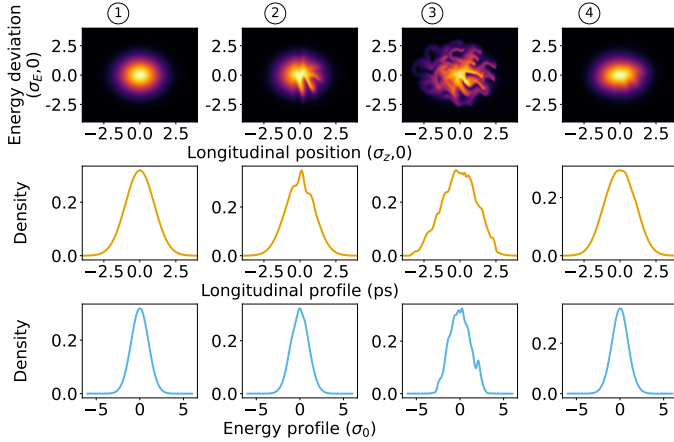
Figure 2.6: Inovesa simulation depicting the formation of the substructures during low alpha operation mode. The first row shows the longitudinal phase space distribution. The middle and bottom rows show the longitudinal and energy profile, respectively. The simulation parameters include: $E_0 = 1.3\,\text{GeV}$, $\alpha_c = 4 \cdot 10^{-4}$, $f_s = 11\,\text{kHz}$, $I_b = 0.4\,\text{mA}$.

2.3   Electron bunch diagnostics

The distributed diagnostic network at KARA, see Fig. 2.7, consists of synchronized detector systems for measuring the longitudinal bunch profile, the energy spread (horizontal bunch profile), and the temporal profile of the THz emission. Although standard diagnostics and detectors exist to measure these parameters, they lack the requirements mentioned in section 2.2. Hence custom setups have been designed/developed for each of these diagnostic stations. One of the motivations of this distributed network is to be capable of reconstructing the phase density of the electron bunch.

The following sections will provide a deep insight into these diagnostic networks and their working principles.
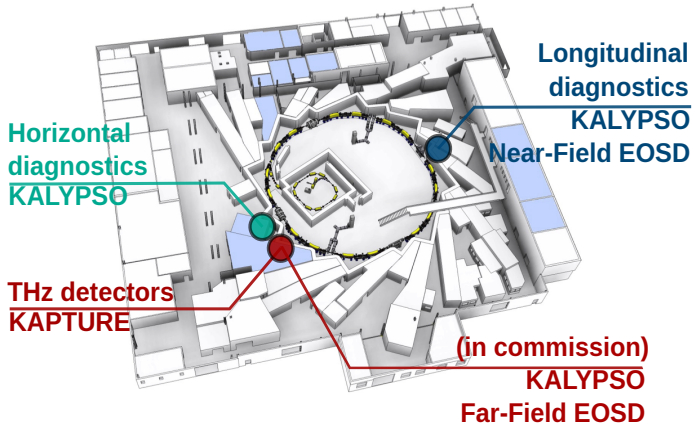
Figure 2.7: Illustration of beam diagnostic distribution network at KARA. Longitudinal and horizontal diagnostics employ KALYPSO as the instrument for single-shot measurements. THz diagnostics employ two approaches to measure the CSR, originally KAPTURE sample card together with a Schottky diode to sample the THz pulses. Presently in commission is a far-field EOSD (Electro Optic Spectral Decoding) set up to be used alongside KALYPSO to measure the spectrum of the CSR. Image courtesy: Ursula Herberger.

2.3.1 Longitudinal bunch diagnostics

The time-dependent electron bunch density can be measured with longitudinal bunch diagnostic tools. These diagnostics help resolve the electron bunch profiles with a resolution down to a few hundred femtoseconds. The most common device used for longitudinal bunch profile measurements is the streak camera[1]. In brief, a streak camera converts temporal information into spatial information via a light deflecting technique explained in detail in [93]. The capability of streak cameras to measure bunch profiles in particle accelerators has already been demonstrated [20].

However, a streak camera has certain limitations; firstly, its sensitivity is low for a single bunch measurement. Hence it is necessary to average the streak image over several turns. Secondly, it has a meagre frame rate, e.g. during the data acquisition

---

[1]   Hamamatsu C5680 streak camera

by streak camera, the time between single acquisitions can be in the range of 100 to 500 s, which leads to a frame rate in the kHz range. To study beam dynamics and the evolution of microstructures, it is necessary to have a diagnostic tool that can provide fs-ps time resolution with excellent spectral sensitivity and MHz frame rate [21].

2.3.1.1 Electro-optical spectral decoding

Electro-optic methods exploit a linear effect called the "Pockels effect", where the refractive index n of the medium changes proportionally to the electric field [22, 24, 23]. This effect is mainly seen in non-centro symmetric crystals, namely lithium niobate ($LiNbO_3$), lithium tantalate ($LiTaO_3$), and compound semiconductors like gallium arsenide (GaAs) and indium phosphide (InP).

The change in the refractive index induced by the electric field as a result of Pockels effect is described by [25],

$$\triangle\left(\frac{1}{n^2}\right) = \sum_{j=1}^{3} r_{ij}E_j \qquad (2.4)$$

where n is the refractive index of the crystal, r_{ij} corresponds to the electro-optic tensors, i ranges from 1 to 6.

From the above equation, we see that the change induced in the refractive index is directly proportional to the electric field. The electric field needed for such modulation can be the near-field (Coulomb field) or far-field (CSR) [26]. The detection of this modulation can be either by a technique called Electro-optic Sampling (EOS) or by EOSD (electro-optic spectral decoding). In EOS, the modulated signal is readout directly by a photodiode combined with an oscilloscope, whereas, in EOSD, the modulated signal is spectrally defracted by the use of a grating. The EOSD measurement setup has been explained in detail below.

Note: EOSD was first implemented in a linear accelerator to detect the Coulomb field of electron bunches [22]. The setup implemented at KARA is the world's first near-field EOSD for a storage ring [23].

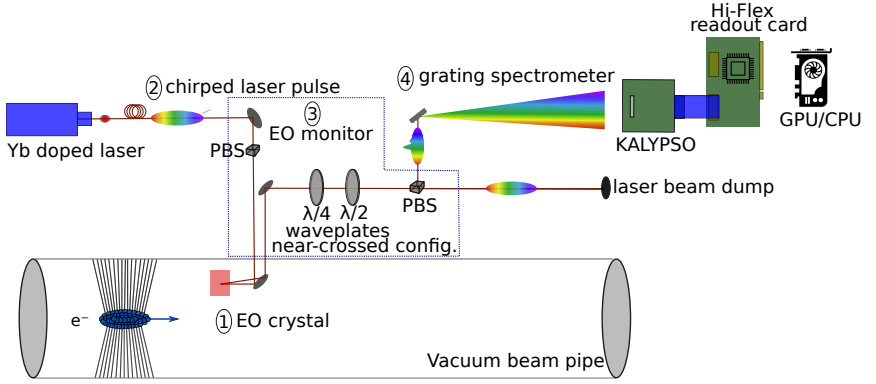Figure 2.8 shows the overall near-field EOSD setup installed at KARA [23].

Figure 2.8: Illustration of the working principle of the EOSD setup at KARA.

1. A self-built ytterbium-doped (Yb) fiber laser [27, 23], with a central wavelength around 1060 nm generates femtosecond laser pulses which are then transported into the storage ring with an optical fiber of length 35-meters, which in turn also behaves like a pulse stretcher by increasing the pulse length from a few femtoseconds to picoseconds. The laser pulse passes through the GaP crystal moved into the vacuum beam pipe in close vicinity to the electron bunch and is transported back to the measurement lab. When the electron bunch and laser pulse are synchronized, a birefringence is induced in the GaP crystal proportional to the electric field (Pockels effect). This results in the bunch profile being imprinted on the spectrum of the laser pulse. With the use of waveplates, the polarization is changed from

linear to elliptical. The relation between the phase retardation introduced and the incident electric field is given by

$$\Gamma = \frac{\omega d}{c} n^3 r_{41} E \qquad (2.5)$$

where Γ is the phase retardation, ω is the laser frequency, n is the refractive index, r_{41} is the electro-optic tensor for GaP crystal, E is the electric field strength [28].

2. The choice of crystal for the EOSD setup at KARA is a 5 mm thick GaP (Gallium Phosphide), as it exhibits a good phase matching between the electric field and the laser. This crystal is movable via controllable motors into the vacuum beam pipe during measurements without the beam's energy loss; hence, this method is also non-destructive.

3. The EO monitor: There are several methods to detect induced phase retardation, namely balanced detection, near-crossed polarised, or crossed polarized scheme. In the current setup, we use a near-crossed polarized scheme for decoding the information. The resulting phase retardation is converted to linear intensity modulation in a near-crossed polarisation scheme. The laser pulse is sent through polarization optics working in a nearly crossed polarization mode. The optics consist of a $\lambda/4$-waveplate used to compensate for the intrinsic birefringence exhibited by the GaP crystal, and a $\lambda/2$-waveplate and a polarizing beam splitter. The polarization changes due to the Pockels effect (electric field of the electron bunch) in the crystal are thus converted into intensity modulation of the spectral components of the laser [23]. Jonas calculus then calculates the final laser intensity given by equation (2.6) [29].

$$I_m = \frac{1}{2} I_l (1 - cos(\Gamma - 4\Theta)) \qquad (2.6)$$

where I_m is the laser power after the modulation at the final position in the setup, I_l is the laser power at the beginning of the setup entering the EO

monitor, Γ is the phase retardation calculated from equation (2.5), Θ is the angle of the half waveplate.
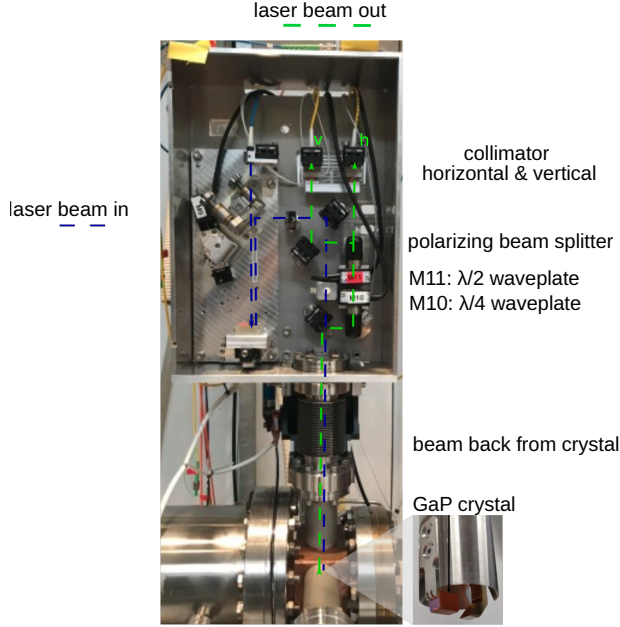

Figure 2.9: Photograph of the EO monitor located near the vacuum pipe of the KARA storage ring.

4. To decode the spectral components of the modulated laser pulse, a grating spectrometer is used. A line array camera later reads this out - KALYPSO [30, 31]. More about KALYPSO will be explained in chapter 5. Three dataset types are needed to calculate the modulation and, thereafter the longitudinal profile. The background signal I_b gives the camera offset along with the existing dark noise, which later needs to be subtracted from the unmodulated signal I_u (signal without bunch profile information) and modulated I_m (signal with bunch profile information). The EOSD signal can be determined by equation 2.7 [32]. A systematic time calibration measurement is necessary to convert spectral information into timing

information. This is performed by changing the phase/delay of the laser pulse—the pulses with the lower wavelength move towards the higher wavelength and vice versa. Datasets are acquired with different delays and are processed offline. A Gaussian fit is applied to the modulation, and the centroid is extracted. The slope of the wavelength (pixel) of the centroid versus delay setting gives the relation between wavelength and time. A more detailed description of the methodology is described in [23].

$$S_{mod} = \frac{I_m - I_b}{I_u - I_b} \approx 1 + \frac{sin(4\Theta)}{1 - cos(4\Theta)}\Gamma \qquad (2.7)$$

Figure 2.10 depicts a measurement of the evolution of the longitudinal bunch profile performed at EOSD setup at KARA using KALYPSO. The longitudinal bunch profile, hence measured, can be used for non-destructive reconstruction of the electron bunch's phase space distribution (PSD) by using filtered back-propagation. The PSD reconstruction method has also been validated using simulations performed with INOVESA. The corresponding paper [33] explains the complete reconstruction algorithm. Figure 2.11 depicts such a reconstruction performed for 6000 revolutions of the electron bunch.
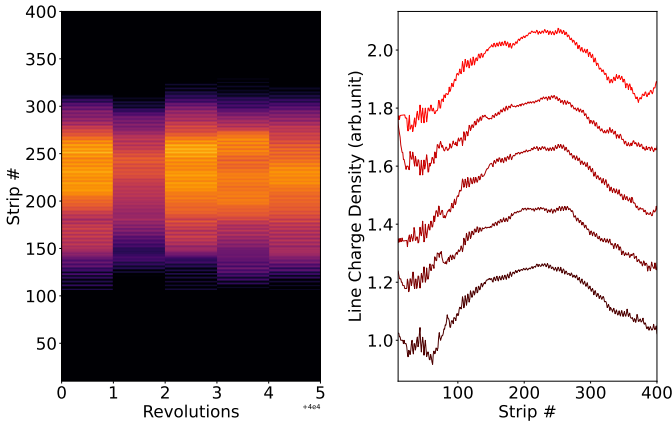

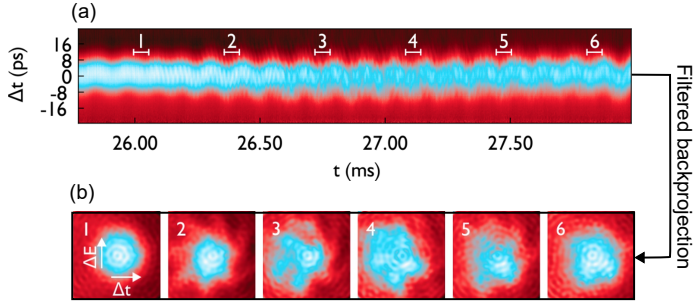**Figure 2.10:** Longitudinal bunch profile measured with KALYPSO at the EOSD setup at KARA.

Figure 2.11: (a) A revolution plot (acquired by KALYPSO) consisting of 6000 consecutive longitudinal bunch profile measurements. The y-axis is the longitudinal bunch size (in raw data corresponds to microstrip numbers) obtained by time calibration measurement, the x-axis corresponds to the revolution time. (b) Corresponding phase space density reconstruction for the time intervals marked in (a), the x-axis corresponds to the longitudinal bunch size, and the y-axis corresponds to the relative energy deviation. Courtesy: S. Funkner

2.3.2   Horizontal bunch diagnostics

As explained in the previous sections, during the low alpha mode, the microbunch-
ing instability starts at a certain current threshold, during which strong CSR bursts
are emitted (bursting regime) [34]. This SR is unstable, and hence so is the energy
spread. There is no known method to measure this energy spread directly. Hence
at KARA, at the Visible Light Diagnostics Port (VLD port), an indirect method
based on measuring the horizontal bunch size and qualitatively studying the energy
spread has been implemented [10]. In the dispersive section of an accelerator,
e.g. 5°-port of a dipole bending magnet, the energy spread increases with the
horizontal bunch size. This relation is given by [18]

$$\sigma_\delta = \frac{1}{D}\sqrt{\sigma_x^2 - \beta_x \epsilon_x}.$$ (2.8)

where σ_δ is the energy spread, σ_x is the horizontal bunch size, D is the horizontal
dispersion, ϵ_x is the horizontal emittance and β_x is the horizontal beta function of
a beam size at a certain point.

To measure the horizontal bunch size, a Fast Gated Camera (FGC) setup has been
installed in the VLD port. The first setup was developed during the course of the
thesis of [10]. Extensive measurements and the upgrading of the optical setup
have been reported in the thesis of B. Kehrer [35]. The experimental setup consists
of a commercial camera[2] with 1200 x 512 pixels and a fast-rotating galvanometric
mirror. Figure 2.12 shows the current optical setup.

With the upgrade of the optical setup, only a single off-axis paraboloid (OAP)
mirror has been used to reduce the induced distortion. The incoherent radiation
coming out of the diaphragm is focused with the help of a paraboloid and planar
mirror, followed by two lenses providing focus in both horizontal and vertical
planes. A wavelength splitter is placed before the OAP mirror to enable parallel
measurements between the streak camera and the FGC. A Time-correlated Single
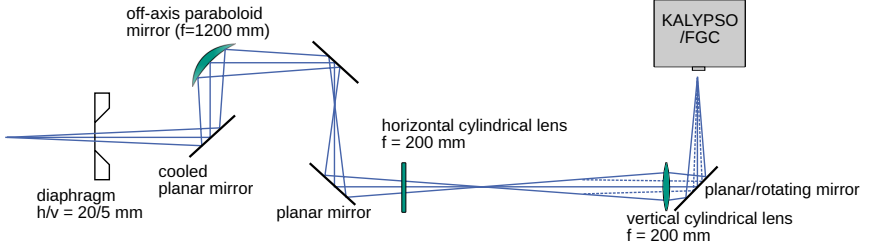
---

[2]   Andor iStar 340T

Figure 2.12: Schematic depicting the optic setup used for the horizontal bunch profile measurements using KALYPSO and FGC. Courtesy of B. Kehrer.

< 400 nm	TCSPC
400 - 550 nm	FGC/KALYPSO
> 550 nm	Streak Camera

Table 2.2: Beam splitting configuration employed for different wavelengths.

Photon Counter (TCSPC) [36] is placed as well for filling pattern measurements [37]. The scheme for the wavelength splitter is described in Table 2.2.

The FGC can pick one in every 6th turn in a single-bunch operation mode, as this depends on the galvanometric mirror's rotation frequency. In contrast, the camera's shutter speed is 2 ns, so it can pick a single bunch in a multi-bunch operation mode. The sensor size limits the number of bunch profiles captured to 80, which is one of the limiting factors, and thus not every turn can be resolved. Figure 2.13 shows an example of data taken from the FGC setup. To resolve every bunch in every turn, the FGC needs to have a repetition rate of 2.7 MHz, which is not the case and the limitations posed by the rotating galvanometric mirror reduces the number of spots that the sensor of the FGC can image.

To overcome this limitation, the FGC is replaced by KALYPSO. Unlike the FGC, KALYPSO is a 1D camera; hence the image is focused only in the horizontal plane during a single measurement.

An algorithm has been developed as a part of the thesis of B. Kehrer [35], to calculate the energy spread from the image acquired from FGC/KALYPSO, where the horizontal bunch size is first calculated. To do so, the filament beam spread
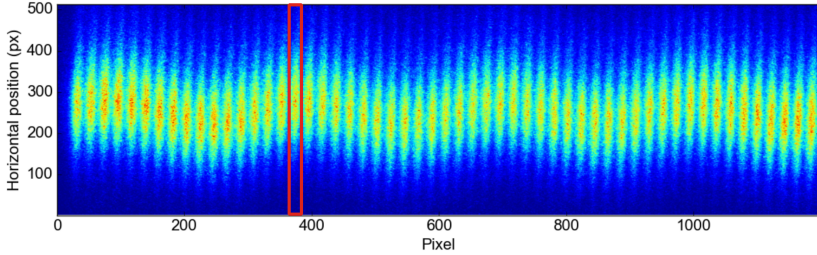
Figure 2.13: Horizontal measurement data obtained with the FGC setup. The highlighted window corresponds to a single bunch profile with an acquisition rate of 125 kHz. Courtesy of B. Kehrer.

function (FBSF) and the horizontal magnification m_{hor} need to be known. FBSF is similar to a point spread function (PSF), which describes the response of an imaging system to a point source, and in the current case, to a 'moving point source' [38]. These are calculated using the optics simulation software Optalix. The image taken from the camera results from the convolution between the FBSF and horizontal bunch size. Once the horizontal bunch size σ_x is known, the energy spread σ_δ can be calculated using equation 2.8. The values of D, β_x, ϵ_x are known via synchrotron optics and are constant throughout the measurement.

3   Semiconductor detectors and front-end electronics

The capability of matter to interact with different charged particles can be exploited, to detect the type, position (flight of path), timing as well as the energy of the impending particle. Almost all forms of matter have been used in order to detect charged particles including solids (semiconductors, scintillators), liquids (liquid Argon), and gases (Geiger-Müller tubes). In most of the materials, charged particles ionize the material thus generating free charge carriers which can be measured and analysed. In particle physics and synchrotron radiation measurement, solid-state detectors based on semiconductor material are quite common. This chapter will briefly describe semiconductors, detectors based upon them, and the front-end architecture used to readout these detectors.

3.1   Semiconductors

Solid-state materials can be grouped into three classes, namely insulators, semiconductors, and conductors. A semiconductor is a material intermediate in conductivity between a conductor and an insulator. Semiconductors are used in a wide range of electronic devices, including transistors, solar cells, and diodes, which are vital components in electronics. Semiconductors are made from elements such as silicon, germanium, and gallium arsenide. The conductivity of a semiconductor can be controlled by introducing impurities into the material which is also known as doping. Doping the semiconductor with impurities such as phosphorus or boron

can create an excess or deficiency of electrons (also known as holes), respectively, which allows the material to conduct electricity [39].

The following subsections will explain the model of a semiconductor and its underlying working principle.

3.1.1 Energy band model

An energy band model depicts how the various energy states in a crystal lattice are occupied. The energy band model consists of a valence band and a conduction band. In a semiconductor, at low temperatures, the valence band is completely occupied with electrons bound to their respective crystal lattices. The conduction band mostly remains empty or could have a few stray electrons due to defects in the crystal lattice. Once the temperature is increased a few electrons located in the valence band gain enough energy and get excited to the conduction band. This is also referred to as thermal excitation. Once they reach the conduction band, they are capable of being conduction carriers. The minimum energy required by the electrons in the valence band to get excited into the conduction band is called the energy band gap of the semiconductor E_g. The conductive property of the semiconductor depends on the energy band gap. If a solid-state material has a very high energy band gap, e.g. 5 eV, they come into the insulator category. In semiconductors, this energy band gap lies between 0.1 eV to 4 eV. Figure 3.1 depicts how electrons were excited from the valence band into the conduction band. When an electron leaves its lattice, the unoccupied place is often referred to as a hole. In semiconductors, both holes and electrons account for the conductivity.

The free electrons (n) and holes (p) density is described with the equation [39]

$$n = n_i e^{E_F - E_i / k_B T} \text{ and } p = n_i e^{E_i - E_F / k_B T} \tag{3.1}$$

with intrinsic density n_i and intrinsic energy E_i and E_F is the Fermi energy level, which lies halfway between the valence and conduction band and whose probability of being occupied is 1/2.
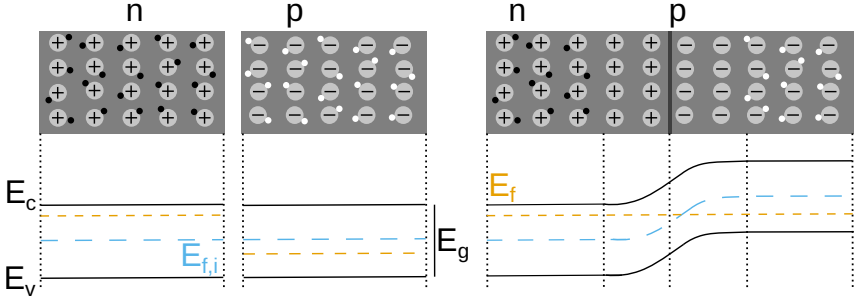
Figure 3.1: Illustration of an energy band in semiconductors. E_C and E_V are the energy levels at the conduction and valence band. E_g is the energy band gap given by $E_g = E_C - E_V$. The labels n, p refer to the type of doping in the material, with n being electrons and p being holes. Adapted from [39].

The charge carriers, electrons and holes are transported in a semiconductor by means of drift and diffusion. For a semiconductor with an electrical field $\overrightarrow{E}$, the average velocity attained by electrons and holes also known as the drift velocity of free charge carriers is given by the equation

$$v_n = -\mu_n \overrightarrow{E} \text{ and } v_p = \mu_p \overrightarrow{E} \tag{3.2}$$

where v_n and v_p are the drift velocities of the electrons and holes, respectively [39]. μ_n and μ_p are the electron and hole mobility, respectively.

Diffusion occurs mainly due to the random motion in a region of non-uniform charge carrier concentration. The carrier flux F in the non-uniform region is given by

$$F_n = -D_n \overrightarrow{\nabla} n \text{ and } F_p = -D_p \overrightarrow{\nabla} p \tag{3.3}$$

where D is the diffusion coefficient related to the carrier mobility by $D = kT\mu/q$ [39]. The total current in the semiconductor is equal to the sum of the drift and diffusion current. The drift-diffusion current is given by,

$$J_{n,p} = J_{n,p|drift} + J_{n,p|diffusion} \tag{3.4}$$

$$J_{n,p} = q \, \mu_{n,p}(n, p)E + D_{n,p}\nabla(n, p) \tag{3.5}$$

3.1.2   P-N Junction

One of the essential semiconductor structures is the p-n junction (see Fig. 3.2), which is formed by oppositely doped regions in a wafer of silicon. This structure is equivalent to a diode, and the current flows in only one direction. To understand the complete working principle let's consider three working regions: thermal equilibrium, application of external voltage and irradiation with light.
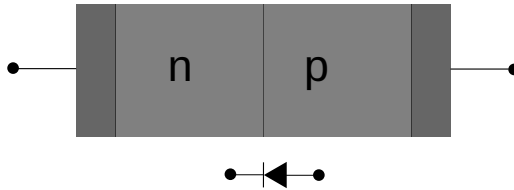

Figure 3.2: Illustration of a simple PN junction.

3.1.2.1   Thermal equilibrium

Consider a homogeneously doped p- and n-regions separated initially and in a state of thermal and electrical equilibrium, i. e. electrons and holes are equally distributed in their respective regions. Once the regions are in contact, electrons move towards the p-region and holes towards the n-region through diffusion. An excess of opposite charges are created in the p- and n-regions, creating an internal electric field and preventing further charge diffusion. Thus, a space-charge region devoid of mobile charge carriers is formed, and the voltage corresponding to the potential difference is called the built-in voltage V_{bi}, which acts as a potential barrier, preventing any further flow of charges[39]. This region is also called the depletion region.

3.1.2.2 Influence of external bias voltage

When an external voltage is applied across the P-N junction, the semiconductor regions no longer remain in a state of thermal equilibrium. When a forward bias is applied, the junction voltage will decrease from V_{bi} by the external voltage V > 0 to V_{bi} - V. The space-charge region shrinks, resulting in a flow of diffusion current, at this point the drift current remains unchanged. When a forward voltage is applied the depletion region shrinks and it increases when a reverse voltage is applied. The width of the depletion region is given by [40, 41]

$$d = \sqrt{\frac{2\epsilon\epsilon_0(N_A + N_D)}{qN_AN_D}(V_{bi} - V)} \qquad (3.6)$$

where N_A and N_D are the acceptor and donor concentrations, ϵ_0 is the permittivity in vacuum equal to 8.845×10^{-14} F cm^{-1} and ϵ is the relative permittivity of silicon ϵ_{si}/ϵ_0 equal to 11.8.

When a reverse voltage is applied to the junctions, the holes and electrons in the p-region and n-region respectively will be attracted towards the electrode away from the junction thus creating a region devoid of any free charge carriers, also called the depletion region. Only a small amount of diffusion current exists at this state. The PN-junction now starts to behave like a detector and signals are generators only with the influence of external stimuli. The break-down voltage V_{bd} defines the limit to the maximum applicable reverse voltage value, after which the diode enters the breaks down region with an increased amount of diffusion current and becomes conductive [39].

3.1.2.3 Irradiation with light

When a semiconductor is reversed-biased, a region devoid of any free charges called the depletion region is formed. When light (photons) with enough energy strikes the semiconductor, it can release an electron-hole pair. The electrons

move toward the positive potential and holes towards the negative potential thus generating a photon current, see Fig. 3.3.
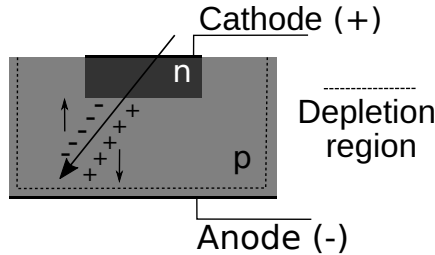
Figure 3.3: Illustration of light interaction with a reversed bias P-N Junction.

The next sections detail the interaction process of radiation with different energies with a semiconductor.

3.1.3 Interaction of electromagnetic radiation with semiconductors

When charged particles pass through matter, they interact with the material's atoms, losing some of their energy, referred to as ionizing or non-ionizing energy loss. Photons interact with the atoms of the semiconductor by transferring their inherent energy to the electrons, hence lifting the electron from the valence band to the conduction band. The processes that mainly define the interaction of a photon with a semiconductor material are the photoelectric effect, Compton scattering (incoherent scattering), and pair conversion of photons. The other photon interactions including Rayleigh scattering, Thomson scattering, and photo-nuclear reactions are not been explained in this section as these processes do not result in any energy transfer from photons into the matter (i. e. no ionization takes place) and only result in the deflection of the incoming photon.

3.1.3.1 Photoelectric effect

When an electromagnetic wave of a short wavelength interacts with a surface of matter, the incoming radiation is absorbed to release electrons. This is called the photoelectric effect. The photon from the incoming radiation disappears after being absorbed by an inner shell electron, transferring all its energy to the interacting electron as shown in Fig 3.4. This process results in the ejection of the electron from the atom.
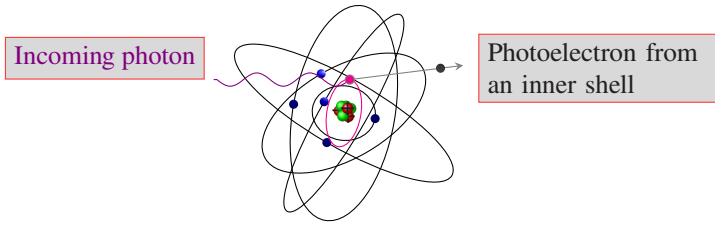
Figure 3.4: Schematic illustrating the process of the photoelectric effect. An incoming photon interacts with matter releasing an electron from the innermost shell. Adapted from [94].

The photon energy is divided between two consecutive processes, first to overcome the electron's band gap energy and then to provide the electron with kinetic energy. In semiconductors, this electron may go on to create more electron-hole pairs as secondary ionization. The probability of photoelectric absorption (τ), is given by [42],

$$\tau \; \alpha \; \frac{Z^n}{(h\nu)^3} \tag{3.7}$$

where Z is the atomic number of the material and n varies between 3 and 4, h is the Plancks constant, and ν is the photon frequency which is equal to c/λ, c being the speed of light in vacuum, and λ the wavelength of the incident photon.
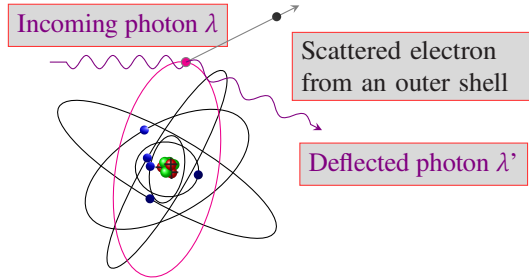
Figure 3.5: Schematic illustrating the process of Compton scattering. A photon with wavelength λ interacts with the electron in the outermost shell of an atom liberating an electron and the photon then deflects away from its path with a wavelength of λ'. Adapted from [94].

3.1.3.2 Compton scattering

Compton scattering also known as incoherent scattering, occurs when a photon interacts with an electron in the outer shell of an atom. The outer electron is liberated and recoils from its position. The photon is not absorbed but deflected into a new path due to this interaction, as shown in Fig 3.5. The energy of the deflected photon is equal to the energy of the incident photon minus the kinetic energy gained by the electron plus its binding energy. The Compton scattering relation is given by [43],

$$\Delta\lambda = \frac{hc}{mc^2}(1 - cos\theta) \tag{3.8}$$

where, $\Delta\lambda = \lambda'-\lambda$, λ' being the wavelength of the deflected photon, λ being the wavelength of the incident photon, and θ is the angle of the deflected photon, h is the Planck constant.

3.1.3.3 Pair production

In addition to the photoelectric effect and Compton scattering, there is one additional process where photons lose energy by interacting with matter. This process is called pair production/conversion. Pair production occurs at high energies. When a high-energy photon (e.g. gamma ray) interacts with an electron or nucleus, it

produces an electron-positron pair as shown in Fig 3.6. The following equation describes this interaction,

$$hv = A_+ + A_- + 2mc^2 \tag{3.9}$$

$$2mc^2 = 1.022 MeV \tag{3.10}$$

When a high-energy (hv) gamma ray interacts with an electron it produces a positron (A_+) and an electron (A_-). The electron has a rest mass equivalent to 0.511 MeV. To overcome this energy a minimum gamma energy of 1.022 MeV is required for the pair production [44].
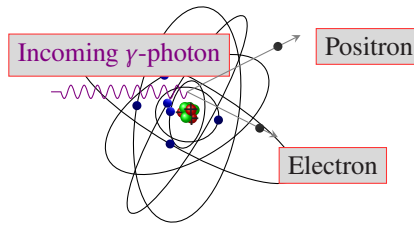
Figure 3.6: Schematic illustrating the process of pair production. A high energy γ-photon interacts with matter producing an electron-positron pair. Adapted from [94].

3.1.3.4 Probability of interaction

The two critical factors that affect the probability of the above photon interactions with matter are the photon's energy (E), the atomic number (Z) and the material's electron density. The main quantities used to qualify the interactions are the linear attenuation coefficient (μ) and the mass attenuation coefficient (μ/ρ). The linear attenuation coefficient is the probability of a photon interaction per distance travelled by the photon through matter. It is given by the sum of the probabilities of the photoelectric effect (τ), Compton scattering (σ) and pair conversion (κ), $\mu = \tau + \sigma + \kappa$. The mass attenuation constant is defined as the ratio of the linear attenuation constant to the density of interacting matter. Given a photon beam of

intensity I_0 interacting with the matter of thickness x, the attenuated intensity of the photon beam is given by the following relation:

$$I(x) = I_0 \ e^{(-x\mu)} \tag{3.11}$$

where the linear attenuation constant μ is given by

$$\mu = \eta_A \sigma_{tot} \tag{3.12}$$

where η_A is the total number of atoms per unit mass and σ_{tot} is the cumulative cross-section of all the interactions mentioned above. Figure 3.7 shows the probability of a photon interaction as a function of its energy in various photon interactions described before.
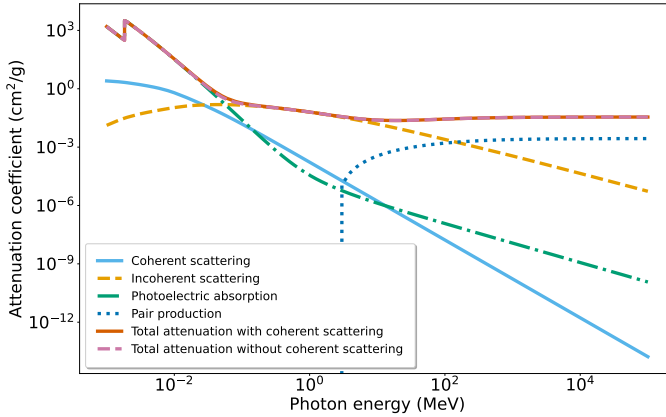
Figure 3.7: Interactions of electromagnetic radiation with a cross-section of silicon depicting coherent (Rayleigh) scattering, incoherent scattering, photoelectric absorption and pair production. Data taken from [95].

3.1.4 Choosing the right semiconductor

Several factors influence the choice of a semiconductor device for a particular application, namely the detector's active area, signal-to-noise ratio (SNR), and cost. Other characteristics such as the spectral sensitivity (wavelength), the light intensity, and frequency of the light in case of pulsed sources/radiation will influence one or more of the main three factors. The main factors considered in the applications mentioned in the later chapters are spectral sensitivity and charge collection time. There are three central regions of interest, near-ultraviolet (NUV) (300-400 nm), visible (400-700 nm), and near to mid-infrared (NIR-mid IR) (800-5000 nm).

For NUV and visible light-based applications, silicon is the first and best choice. Beyond 1080 nm due to the increasing penetration depth, the photons pass through with less probability of producing any charge pairs in the silicon. Hence for applications in the NIR region corresponding to wavelengths up to 2500 nm, indium gallium arsenide (InGaAs) is a good solution. For wavelengths beyond 2500 nm, extending into the mid-infrared regions semiconductors based on lead sulphide (PbS), lead selenide (PbSe), thermopiles, indium arsenide (InAs), or mercury cadmium telluride ($Hg_{1-x}Cd_xTe$) can be employed. Figure 3.8 is an example of the spectral responsivity of semiconductors in the NIR spectral region. It should be noted that some semiconductors only operate at sub-0 °C temperatures while our applications require them to operate with good noise performance at room temperature.

One of the key parameters for high-speed applications is the semiconductor's charge collection time (CCT). CCT is defined as the time interval for the integrated charges generated after the interaction with an ionizing particle, to increase from 10 % to 90 % of its final value. Silicon and InGaAs have a CCT of around 20 ns depending on the topology, PbSe and PbS have a broader charge collection time of a few ms, which is a disadvantage for applications requiring MHz repetition rate.
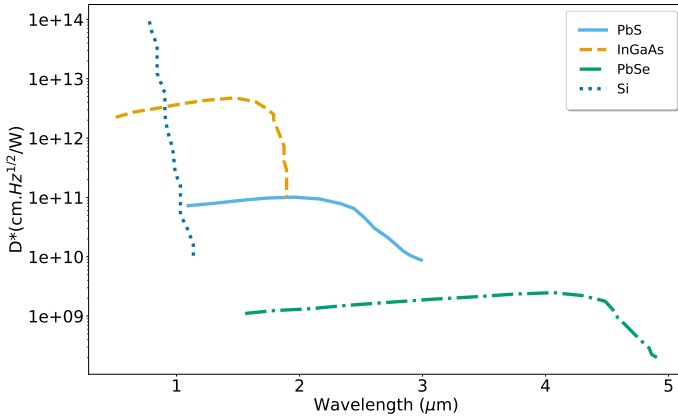
Figure 3.8: Spectral responsivity D* of Si, InGaAs, PbS, PbSe based semiconductors. Adapted from [45].

The detector's active area also plays an important role, especially for intensity measurements requiring the semiconductor to accommodate the beam spot completely. Most silicon detectors employed in tracking (detecting the position of particles) have a diameter of a few centimeters. A smaller area decreases the junction capacitance and affects the overall SNR. Figure 3.9 shows the size and dimensions of the available semiconductors.

It also has to be noted that there are three operational detectors: photovoltaic, photoconductive and photoemissive. An electrical signal is generated in photovoltaics due to the PN junction explained in section 3.1.2, e. g. silicon, InGaAs. In photoconductive detectors, the conductivity of the material changes with the intensity of the incoming photons carried on the electrical current signal when the sensor is biased by a constant voltage, e. g. PbS, PbSe. Photoemissive detectors are based on the photoelectric effect, where the detector consists of a photocathode that absorbs photons and generates photoelectrons, e. g. photomultiplier tubes (PMTs).
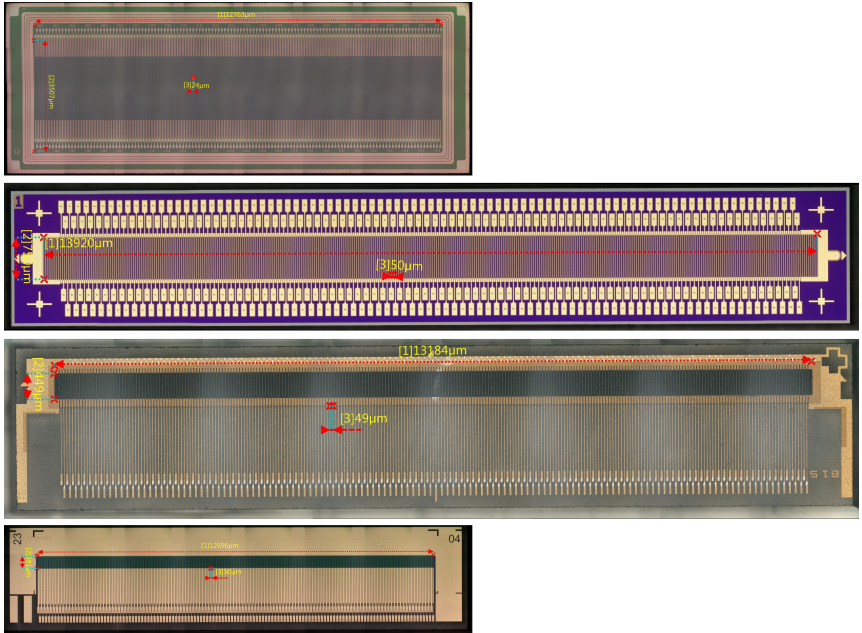
Figure 3.9: Micro-photograph of (top to bottom): Si, InGaAs, PbS, PbSe microstrip sensors.

3.2 Detectors for intensity and position measurement
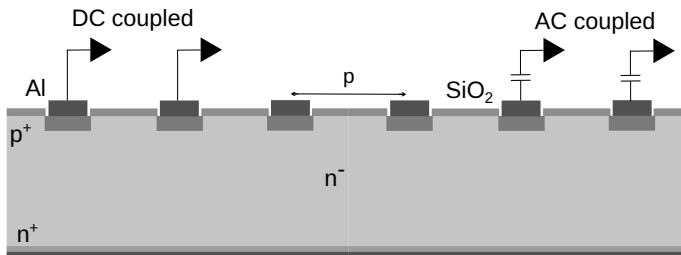
Figure 3.10: Illustration of a cross-section of a segmented semiconductor sensor.

35

The energy loss of radiation or particle is proportional to the ionization process in the semiconductor. The intensity of the radiation can be obtained from a front-end ASIC (Application specific integrated circuit), which can convert incoming charges into a reference voltage. The impact position of the radiation can be determined by segmented 1-dimensional (strip) or 2-dimensional (pixel) diode structures, see Fig. 3.10.

The position or spatial resolution of a measurement or the detector's resolution is mainly given by the pitch of the diode structures. For a detector with a pitch p, the precision of measurement is given by [46],

$$\langle \Delta x^2 \rangle = \frac{1}{p} \int_{\frac{-p}{2}}^{\frac{p}{2}} x^2 \, dx \tag{3.13}$$

The pitch of a detector can vary from a few hundred microns down to a few tens of m.

For position measurements, the resolution of the readout based on the threshold from a single strip 'x' is given by [48, 47],

$$\sigma_x = \frac{p}{\sqrt{12}} \tag{3.14}$$

And for an analog readout on multiple strips, the resolution is given by [48, 47],

$$\sigma_x = \frac{p}{SNR} \tag{3.15}$$

However, the energy resolution of a detector is dependent on the energy of the incoming radiation and the statistical variance in the number of charges generated inside the detector due to this radiation. The Fano factor is used to describe this variance and is given by $F = \sigma^2 \epsilon / E$. F is the Fano factor, σ^2 is the variance, ϵ is the ionization energy and E is the energy of the incoming radiation. The energy resolution is usually expressed in terms of the FWHM (Full Width Half Maximum)

of the energy spectra. The energy resolution can then derived in terms of the Fano Factor as [49],

$$E_{FWHM} = 2.355\sqrt{F \cdot E \cdot \epsilon} \tag{3.16}$$

All segmentations, strips or pixels, are connected to a front-end ASIC via a capacitor (AC coupled) or directly (DC coupled) as shown in Figure 3.10. The bias voltage is either provided by a metal implant on the backplane or via front side biasing [50]. In scenarios where there is a scarcity in the number of readout channels in the front end, it is possible to implement resistive or capacitive charge division.
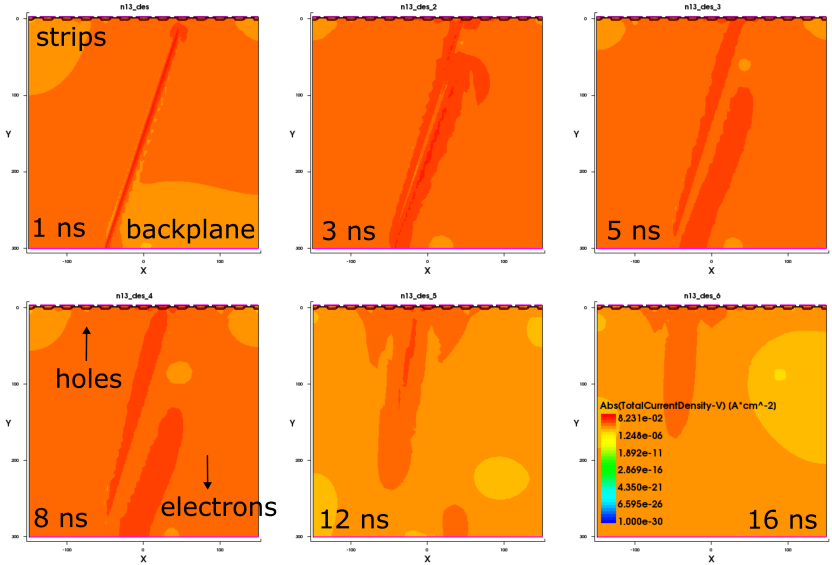
Figure 3.11: Simulation of the total current density charge in a Si microstrip sensor due to the stimuli of a NIR beam. Holes are collected by the top metal pads on the strips and electrons are collected by the backplane. The charge generation and collection are studied for a time of 20 ns, a selected time sequences are noted in the individual frames.

The working mechanism of such a sensor can be simulated using TCAD (Technology Computer Aided Design). Figure 3.11 shows the simulation of total current

density in a microstrip sensor. This sensor has a thickness of 300 m and a pitch of 25 m. The voltage bias of the sensor is provided via the backplane and its value is held at 150 Volts for this simulation. The bulk is made of n-type and the strip/implant is of p-type semiconductor and is fully depleted at 40 Volts. Photons with a wavelength of 1050 nm are applied on the sensor's surface. This leads to the generation of electron-hole pairs. The number of these pairs ($N_{e,h}$) depends on the intensity of the beam or the total number of photons incident per second. The holes then start to drift towards the charge collection node (p-side) and the electrons are collected at the backplane (n-side) of the sensor. It is evident from this simulation that electrons as charge carriers have higher mobility than holes and hence are collected faster.

In reference to the simulation work carried out in the master thesis by the author, sensor production by a dedicated engineering run was performed for fabricating the sensors with several geometries and channel pitch sizes. The sensors were fabricated at *Fondazione Bruno Kessler: FBK - Trento*[1]. In addition to the fabrication, a special anti-reflection coating layer (ARC) consisting of a sandwich of SiN_x and SiO_2 was applied to improve the overall absorption efficiency of the sensor in the NUV, visible and NIR range. A wafer from this production run is shown in Fig. 3.12.

3.2.1 LGAD basic principles

In the previous sections, the working principle of silicon detectors based on PIN diodes has been explained. In brief, a depletion region is formed in a PIN diode when operated in reverse bias voltage, which then allows it to generate a signal which is proportional to the intensity of photons incident on the PIN diode. Conventional detectors based on PIN diodes are the most widely used detector for measuring a wide spectral range of radiation. They are capable of high spatial resolution due to segmentation (pixels, strips), and high quantum efficiency for a

---

[1]   https://www.fbk.eu/
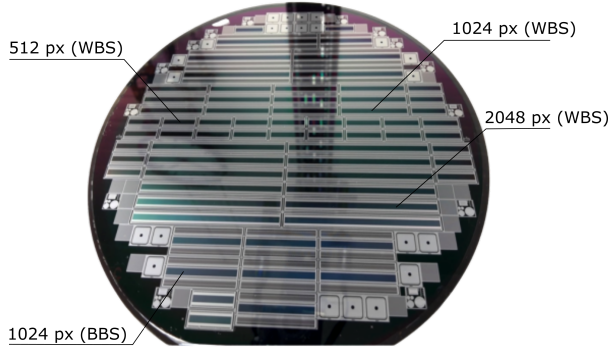
Figure 3.12: A silicon wafer with several microstrip geometries designed at KIT and fabricated at FBK. WBS refers to wire bondable sensor, BBS refers to bump bondable sensor.

wide wavelength range. But when used to detect low-intensity radiation, the noise in these detectors dominates the overall signal formation, resulting in low SNR in the subsequent measurements.

This limitation can be overcome by an Avalanche Photodiode (APD). This type of diode exhibits an internal gain between 100-1000, hence allowing the detection of radiation of low intensity. However, APDs have disadvantages concerning the high leakage current, which is not easy to handle by modern readout electronics, requiring additional quenching circuits. The noise associated with the APDs multiplication process is still quite high, hence they have high dark noise compared to conventional PDs.

The possible solution to this limitation is to reduce the gain to a tenth order through doping. Such a detector will have a linear response and be easily integrated into existing readout electronics. Such a device is also called a Low Gain Avalanche Detector (LGAD).

The basic structure of an LGAD in contrast to a conventional PIN diode is shown in Fig. 3.13. LGADs have an additional diffusion called a 'gain' implant underneath the standard implant. This results in the additional localized electric field region. Conventional PIN diodes need a high reverse bias voltage to achieve a high electric

39
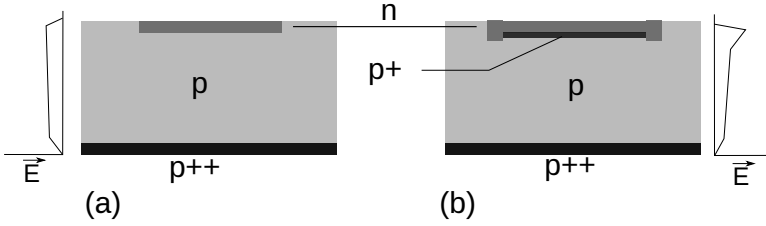
Figure 3.13: Illustration comparing structure and electric field distribution between (a) conventional Si micro-strip sensor and (b) Si low gain avalanche detector.

field. Still, the additional gain region in the case of LGAD allows it to achieve a very high electric field even at a low reverse bias voltage. Figure 3.13 also depicts an example of electric field distribution across the bulk of the sensor. It shows that the PIN diode has a uniform electric field distribution, contrary to LGAD where the gain layer has a significantly higher electric field. LGADs have a very high electric field in the range of $300\,\mathrm{kV\,cm^{-1}}$.
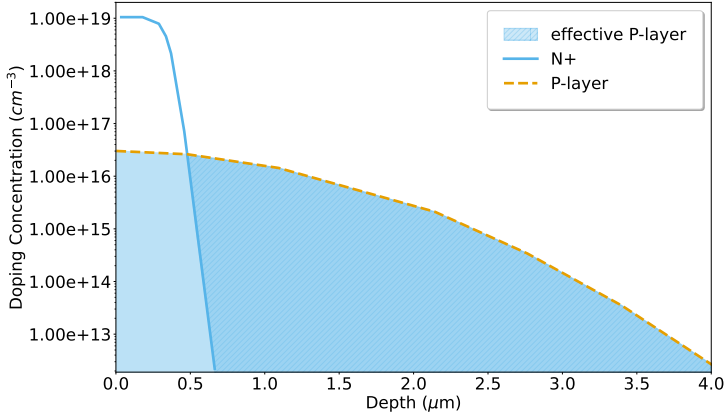
Figure 3.14: An example doping concentration profile for a low gain avalanche detector, reproduced from [51].

3.2.1.1 Avalanche mechanism models

Section 3.1.3 describes how radiation interacts with matter, especially silicon. In an LGAD, the generated charge multiplies exponentially when it drifts into the regions with high electric fields. The number of charges generated by such an avalanche mechanism is given by [52],

$$N_{e,h}(d) = N_{e,h}(0)e^{\alpha_{n,p}d} \tag{3.17}$$

where, $N_{e,h}(d)$ is the number of electron-hole pairs generated, d is the depth of the radiation travelled inside the high electric field region, $\alpha_{n,p}$ is the coefficient of impact ionisation

Several impact ionisation models are used to estimate the LGAD behaviour using TCAD simulations. The two most common models are the Van Overstraeten model [53] and Massey model [54], both of which use the Chynoweth law (equation 3.18) for calculating the impact ionization rate. In addition, there are also the Bologna model [55] and Okuto model [56] which use independent parameters. The Chynoweth law model is described by,

$$\alpha = a \cdot e^{-\frac{b}{E}} \tag{3.18}$$

where, a is a constant equal to the maximum number of electron-hole pairs that can be generated, b is a constant that depends on the temperature, E is the electric field strength

In the design of an LGAD, the depth of the gain implant plays an important role. Figure 3.15 shows the three different types of gain implants: (a) *broad doping*, the gain layer is in contact with the n-electrode. (b) *shallow doping*, the gain layer is separate from the n-electrode but in close proximity. (c) *deep doping*, the gain layer is far away from the n-electrode [52].
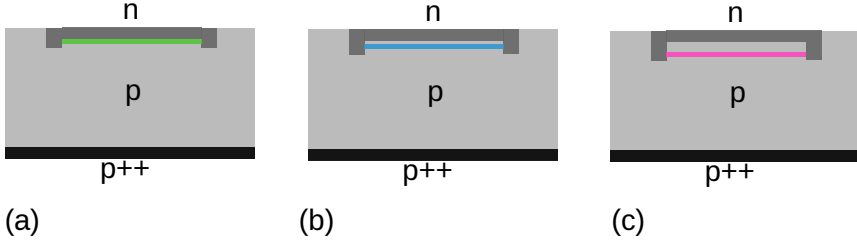
Figure 3.15: Illustration of three different types of doping mechanisms used for LGADs (a) broad doping, (b) shallow doping, (c) deep doping.

Ramo-Schockley's theorem is the basis for calculating the amount of induced current transferred to an electrode by the moving charge in its vicinity [57, 58]. The induced instantaneous current i collected by the electrode is given by

$$i = E_v \, q \, v \tag{3.19}$$

where, v is the drift velocity of the charge q, E_v is the electric field, and q is the charge of an electron.

Assuming a diode with the electrode much larger than the thickness of the sensor the maximum current at the electrode can be then derived as [59]

$$i_{max} = Nq\frac{1}{d}v = n_{e,h} \, d \, q \, \frac{1}{d} \, v = n_{e,h} \, q \, v \tag{3.20}$$

where, N is the total number of e-h pairs generated for a sensor with thickness d and is given by the product between the sensor thickness (d) and the number of e-h pairs generated per unit length ($n_{e,h}$) of the sensor. Equation 3.20 shows that the maximum current induced at an electrode depends only on the drift velocity of the electron-hole pairs and not the thickness of the sensor. $n_{e,h}$ is proportional to the thickness of the sensor d, however, the weighting field E is inversely proportional to d, therefore each $n_{e,h}$ (e-h pairs generated per unit length) contributes less current with the increasing thickness.

To study the basic LGAD charge generation and collection behaviour simulation was performed for an LGAD structure with 50 m thickness, 3 strips, and deep

doping for the gain layer. A maximum bias of 160 Volts was applied. A MIP (minimum ionizing particle) was simulated on the centre strip to excite charge formation.
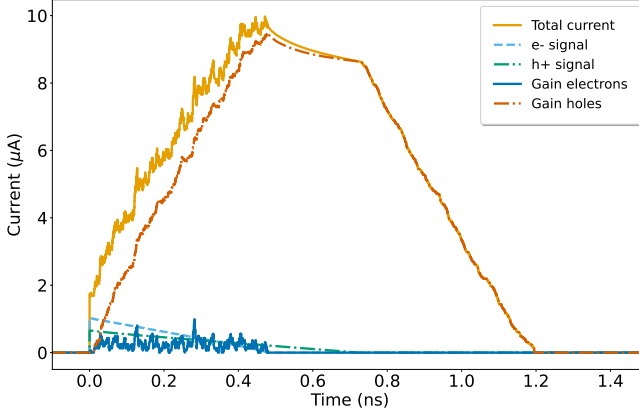
Figure 3.16: Simulated signal formation in an LGAD, 'Total current' refers to the signal generated accounting for both electrons and holes, 'e- signal' and 'h+ signal' refers to signal accounting to the electrons and holes individually.

Figure 3.16 shows how a signal was formed from the simulation. The primary charge carrier's electrons and holes drift toward the n and p electrodes respectively. When the electrons reach the gain layer the avalanche mechanism begins and secondary electron-hole pairs are generated. This process occurs very close to the connection node and thereafter the multiplied electrons are collected very fast. The holes must travel through the entire bulk and contribute to most of the signal. Electrons have higher mobility than holes, hence electrons are collected faster than holes. Hence the rising edge of the 'Total current' is the electrons collected by the cathode. The almost flat region is where the holes are still drifting through the bulk, and the signal decreases when the holes are collected at the anode.

The current after the avalanche mechanism can be estimated as [59]

$$\frac{dI_{gain}}{dt} \propto \frac{G}{d} \tag{3.21}$$

43

where $\frac{dI_{gain}}{dt}$ is the signal slew rate, G is the total gain, and d is the thickness of the sensor

The equation 3.21 implies that the slew rate of the sensor is inversely proportional to the thickness of the detector. Hence thinner sensors are faster and have high gain, see Fig. 3.17. Hence such sensors are beneficial in experiments that require high temporal resolution.
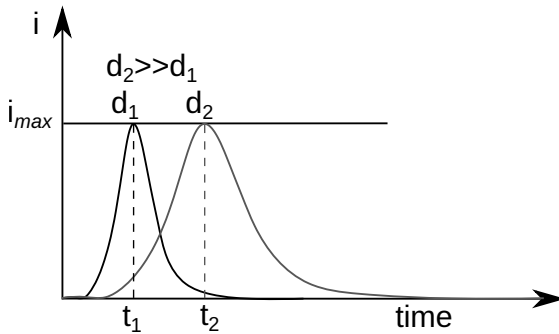
Figure 3.17: Illustration of relation between the thickness of a detector and the slew rate. The two curves show the signal response of LGADs with bulk thickness d_1 and d_2 with $d_2 \gg d_1$. The time label t_1 and t_2 is the time taken by the detector to reach maximum amplitude. Adapted from [59].

3.3 Front-end electronics

A front-end ASIC is a device consisting of a sequence of blocks to amplify
and condition the signal for precise conversion to digital signals in the later
stages. Figure 3.18 gives a standard representation of an ASIC for reading out
and conversion of the charges generated by a semiconductor microstrip detector.
The first stage of such an ASIC is a charge-sensitive amplifier (CSA), followed
by either a shaper or a correlated double sampling (CDS), a channel buffer, and a
multiplexer.
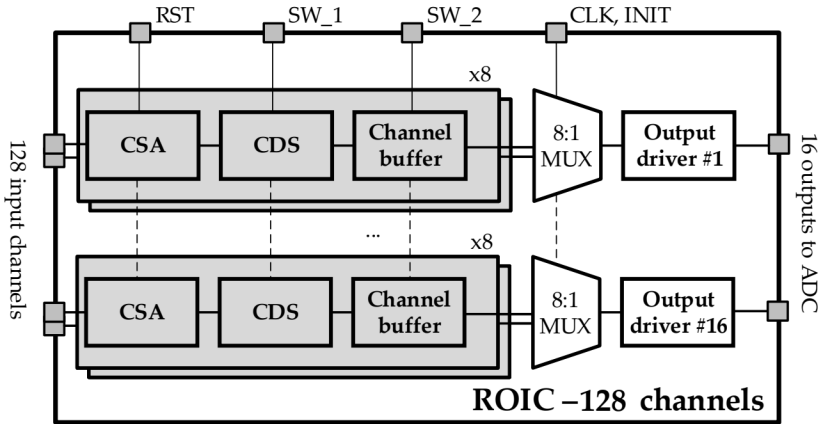
Figure 3.18: Block diagram of a typical ASIC used for converting and reading out the charges generated
by a microstrip detector. Taken from [31].

3.3.1 Charge sensitive amplifier (CSA)

The charge-sensitive amplifier represented in Fig. 3.19 consists of an inverted
amplifier, which outputs a voltage proportional to the charge and the feedback
capacitance C_f. C_D is the detector capacitance, and C_i is the input capacitance
dominated by the transistor's gate capacitance.

45
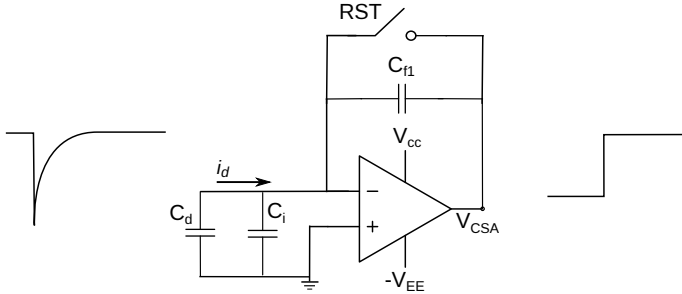
Figure 3.19: Typical schematic and output of a CSA.

The basic transfer function of the CSA with a gain A can be represented by

$$V_{out} = -AV_{in} \tag{3.22}$$

The charge Q_{in} generated by the semiconductor is integrated by keeping the RST switch open and the RST is closed during the readout of this integrated charge. The use of a switch allows for synchronous readout usually controlled by an external signal of an experimental setup. The voltage appearing at the output of the CSA is given by

$$V_{out} = -\frac{Q_{in}}{C_f + \frac{C_D+C_f+C_i}{A}} \tag{3.23}$$

Assuming a large amplification A, the charge will be transferred completely from the detector to C_f, and the output of the CSA is then given by

$$V_{out} = -\frac{Q_{in}}{C_f} \tag{3.24}$$

The total noise introduced by the CSA stage is dominated by the noise generated at the input transistor. The noise can be divided into series and parallel noise as depicted in Fig. 3.20. The serial noise component of the CSA corresponds to the presence of an output voltage, even in the absence of an input charge. Parallel noise, however, is mainly contributed by the detector itself, wherein the leakage current introduces statistical fluctuations in the output voltage of the CSA.
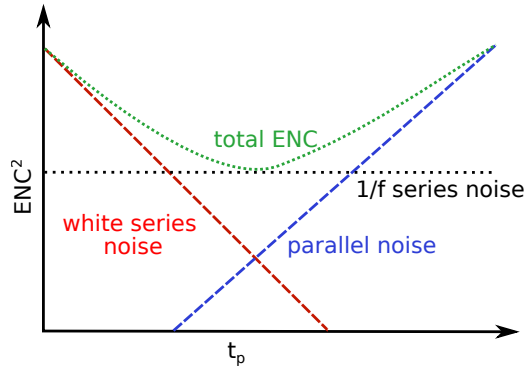
Figure 3.20: Evolution of series and parallel noise (Equivalent Noise Charge - ENC) as a function of the peaking time (t_p) at the input stage. The time constant of the stage is given at the point where the series and parallel noise is equal.

3.3.2 Noise shapers
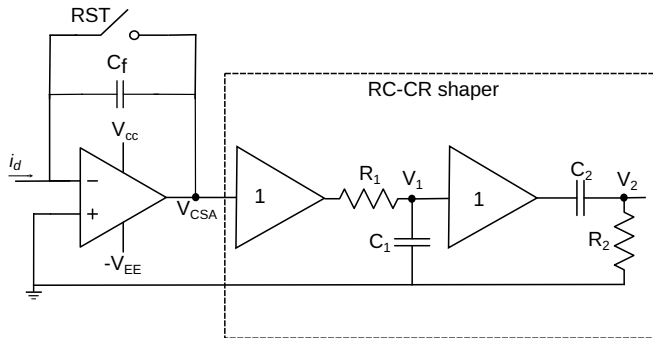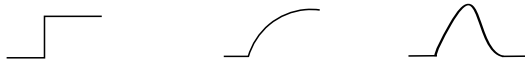
Figure 3.21: Typical schematic and outputs of an RC-CR shaper.

The input transistor in the CSA contributes to most of the noise evaluated in the complete ASIC. To improve the SNR and reduce interference, a filter/shaper stage

is implemented. It can be based on a time-invariant RC-CR filter, whose frequency response is fixed in time, or a time-variant filter whose frequency response changes during the operation of the detector. Figure 3.21 depicts the RC-CR filter following the CSA stage.

For the amplified output voltage from equation 3.24, the shaper stage performs an RC integration and then a CR differentiation. The resulting output voltage has a time constant given by

$$\tau = R_1 C_1 = C_2 R_2 \tag{3.25}$$

The voltage V_2 at the output of the shaper stage is given by

$$V_2 = V_{CSA} \frac{t}{\tau} e^{-\frac{t}{\tau}} \tag{3.26}$$

$$V_2 = \frac{Q_{in}}{C_f} \frac{t}{\tau} e^{-\frac{t}{\tau}} \tag{3.27}$$

3.3.3 Correlated double sampling
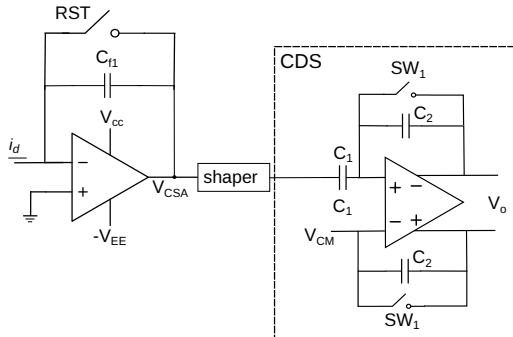
Figure 3.22: Typical schematic of a correlated double sampling (CDS) stage.

Figure 3.22 depicts a fully differential correlated double sampling (CDS) stage following the CSA. This is a stage in the readout cycle of the ASIC where two samples are taken. The first sample is taken in the reset stage at t_0 when *RST* is

open and *SW1* is closed and the second sample is taken at t_1 when the signal charge has been transferred to the readout node. The two samples are in differential and the output of the CDS stage is the difference between the two signals. The CDS stage effectively eliminates fixed pattern noise (FPN), which is quite common in silicon imaging sensors [60].

The transfer function of the CDS stage is given by

$$V_o(t) = -\frac{C_1}{C_2}(V_2(t_0) - V_2(t_1)) \tag{3.28}$$

$\frac{C_1}{C_2}$ gives the gain of the CDS stage. Since the input to the CDS stage is single-ended, to convert into a differential output, the positive input is connected to the output of the CSA stage and the negative input is connected to a common-mode voltage V_{CM} which is set to be half the power supply $\frac{V_{cc}}{2}$.

3.3.4 Channel buffer

The channel buffer is the stage after the CDS where it can sample and hold the signal value during the readout phase. This is implemented using a unity gain sampler, similar to a voltage follower configuration, but with additional switches that control the sample and hold. A simple representation of such a stage is shown in Fig. 3.23.

The working principle of this stage is as follows. In the first step, the switches *SW2*, *SW4* are closed, and *SW3* are open. The voltage V_1, V_0 is 0 and the voltage across C_1 is equal to V_{in}. The second step is to open *SW4*, which transfers the charge at the capacitor C_1 into V_1. The third step is to open *SW2*, now, since *SW4* is also open, it makes node V_1 floating. And when *SW3* is closed, C_1 holds its voltage. The charge across the capacitor is given by

$$q_1 = C_1(V_0 - V_1) \tag{3.29}$$

Since V_1 is a virtual ground

$$V_{in} = V_0 = \frac{q_1}{C_1} \tag{3.30}$$
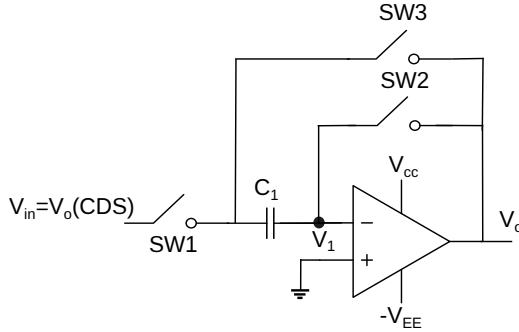
Figure 3.23: Typical schematic of an output buffer. Adapted from [31].

3.3.5 Channel Multiplexer

Designing and fabricating the complete signal conditioning stage for sensors with hundreds to thousands of channels can be difficult in terms of line rate, power consumption and complexity in layout. Hence frequently if readout speed is not critical input channels are grouped by an analog multiplexer.

A typical schematic of an analog multiplexer is shown in Fig. 3.24. A series of D flip-flops (DFF) controls the transmission of analog signals, one for each output analog signal. Each analog signal group is connected to a single output driver, and only one signal can be transmitted at a time. A high-to-low signal transmitted on the INIT node enables the first DFF to transmit the analog signal. After the first analog signal is transmitted, the second analog signal is transmitted with the second pulse of the CLK signal, and so on for the rest of the group.
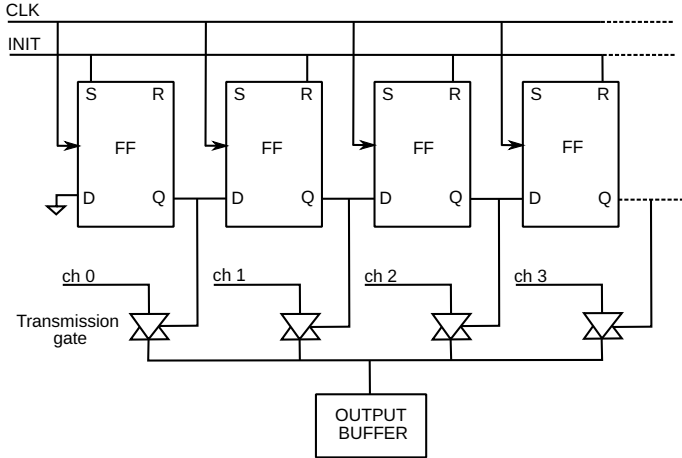
Figure 3.24: Typical schematic of an analog multiplexer. Adapted from [31].

3.3.6 Output Driver

An output driver usually concludes the final stage of the ASIC. This stage connects the ASIC to the PCB via metalized pads. These pads are then further connected to an ADC for further processing the analog signal. The output driver can be in a source follower or a push-pull configuration. This stage's main requirement is low output impedance, fast slew rate, low settling time and minimum cross-talk between other output drivers. A typical output driver in a fully differential class-AB amplifier is shown in Fig. 3.25. The gain of this stage is given by the ratio of R2 and R1, thus making the output voltage $V_0 = \frac{R2}{R1} \cdot V_{in}$.
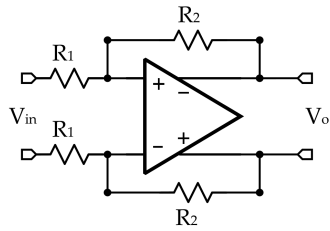
Figure 3.25: Typical schematic of an output driver. Taken from [31].

4 Development of advanced sensors and ASICs

Developing a new detector has crucial factors, including complexity, design, and fabrication costs. Hence it is vital to use device simulation tools to study and optimize the design parameters for the detector. This chapter mainly focuses on the simulation methodology used to understand LGAD microstrip sensors, the characterization of the TI-LGAD sensors and layout of the Gotthard-KIT ASIC.

4.1 TCAD

TCAD (Technology Computer Aided Design) is a platform used for simulating semiconductor processes and structures. It collectively provides a way to perform finite element analysis (FEM) and Monte Carlo simulations to study the semiconductor's electrical properties. In this thesis, two tools have been used to study the behaviour of detectors based on LGAD, Sentaurus TCAD [96] and Weightfield [97].

Figure 4.1 represents the simple process flow in TCAD. At first, the physical structure and its constraint parameters, including doping concentrations, metalization, and geometry, are designed using the structure editor. To perform the device simulations using the finite element method in the next step, it is necessary to define a meshing strategy. The smaller the mesh, the more accurate the device calculation; however, a smaller mesh requires higher computing power and longer run-time. Hence a non-uniform meshing is applied to optimize the simulation throughput. The crucial parts of the detector, e.g. the charge collection nodes, and
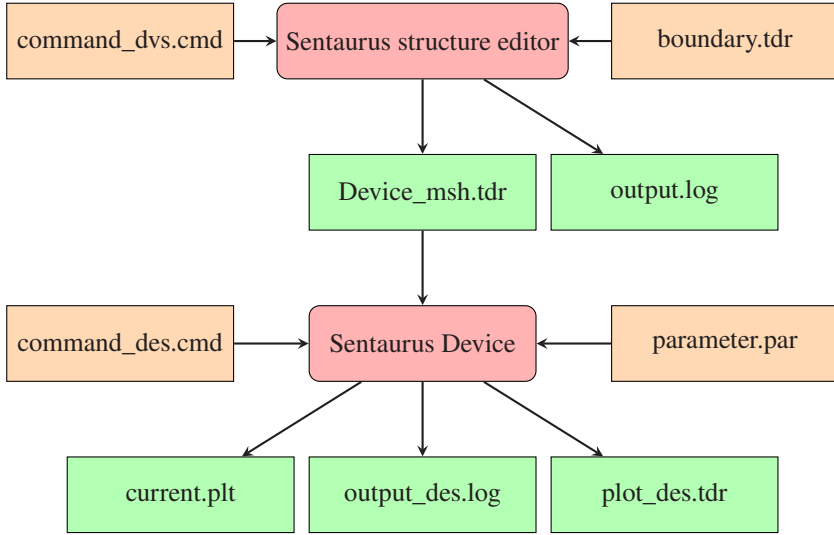
Figure 4.1: Depiction of the TCAD simulation workflow. The red blocks indicate the tools used, the orange block includes the input files which contain the structure design, simulation parameters and boundary conditions, and the green blocks indicate the output of a simulation run, including the raw output datasets, plots, run and error logs.

backplane contact, have a smaller mesh area than the rest of the bulk. An example of such a strategy is shown in Fig. 4.2.

The meshed structure is then fed as input to the sentaurus device tool, which runs the simulation. The nature of the simulation defines the kind of behavioural models to be used. Some of the models included during the simulation of the LGAD are DopingDep, ElectricField, eAvalanche (vanOverstraeten), etc. The next step is to define the simulation conditions, including the temperature, area factor (size the 2D device into the third dimension), node voltages, etc.

Based on these conditions, steady state, quasi-stationary and transient analysis is performed on the device. Steady-state analysis is performed at a specific node voltage, and physical properties such as space charge and electric field density are studied at the particular voltage. The quasi-stationary analysis includes studying the I-V characteristics of a device by increasing the node voltage until a maximum

value specified is reached and calculating the corresponding steady-state current. The transient simulation includes keeping the node voltage constant but calculating current at specific time intervals. This analysis is especially useful when providing the device with an external stimulus like a heavy ion or optical beam impinging on the structure.
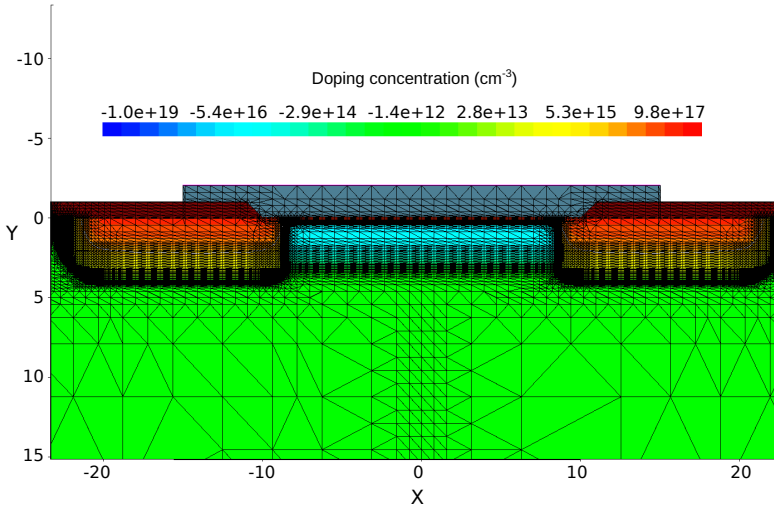
Figure 4.2: The 2D triangular meshing design adapted for the TCAD simulation. The critical region around the junction has a denser mesh placement to provide more accuracy.

The results of these analyses will be discussed in the upcoming sections of this chapter.

4.2 LGAD - Simulation

Simulating the LGAD with TCAD first requires the physical definitions of the device, such as the thickness of the bulk, dimensions of the microstrip, doping concentrations, and metal contacts. Once the structure has been defined with

Property	Value
Bulk thickness	50 m
Bulk doping concentration (Boron)	1×10^{12} cm^{-3}
n implant doping concentration (Phosphorus)	1×10^{19} cm^{-3}
p implant doping concentration (Boron)	1×10^{16} cm^{-3}
p implant depth	0.7, 1.7, 2.3 m
Implant pitch	50 m
Bias voltage	-100, -200, -300 −400 V
Transient analysis time	15 ns

Table 4.1: Detail list of physical parameters used for the simulation of the LGAD.

absolute or variable parameters, the device is activated with external stimuli such as bias voltage and optical illumination and the device's behaviour's studied. To reduce computing resources, 2D simulations have been performed.

4.2.1 Physical design parameters

To simulate the behaviour of an LGAD, the physical parameters of Table 4.1 have been used.

Figure 4.3 is an example of an LGAD structure generated by the Sentaurus structure editor[1]. For the simulation, an n-type LGAD has been devised, i. e. the bulk of the LGAD is modelled with silicon doped with a p-type impurity and the implant is doped using an n-type impurity. The structure designed has been created for 2D simulations. A two-strip structure (1 full strip, two half-strips) has been implemented with a pitch of 100 m. The bulk of the structure is made up of boron-doped silicon. The structure also includes a shallow phosphorus-doped implant, with wide and deep doping on the edges of the implant, which make up

---

[1] Note: The structure is just one example of simulated devices. Since Sentaurus uses a parent tree structure, a variation of the parameters mentioned in Table 4.1 has been simulated. In this chapter, only a selected few simulations have been shown.

the JTE (Junction termination extension). Below the implant is the boron-based p-type gain layer, which is the multiplication implant. Variants in this implant's depth, width and concentration have been simulated to achieve a reasonably high electric field. One major challenge posed by n-type LGADs is the isolation between adjacent n+/n+ strips. Due to the fixed positive charges trapped under the Si/SiO_2 junction, an accumulation layer is formed between strips leading to a conduction path between adjacent strips. This can be avoided by implementing a p-spray/p-stop as an electrical insulation between the strips. A p-spray is a uniform layer applied throughout the surface, whereas a p-stop is a smaller structure between the strips with a higher doping concentration [61]. The biasing has been implemented on the backplane of the structure. It is also possible to implement front-side biasing utilizing the conductive properties at the edge of the structure by implementing a metal deposition. The process of front-side biasing is advantageous for fabrication and assembly processes [50]. The additional elements of the structure include the oxide layer as a passivation layer for insulation and surface protection. The strips have an aluminium contact with the front-end read-out electronics.

4.2.2 Electric field simulation

The electric field at the junction of the implants is an important parameter that controls the structure's gain and breakdown voltage. Figure 4.4 shows an example of a high electric field distribution at the n-implant and p-multiplication implant junction. The breakdown field of silicon is $300 \, \text{kV} \, \text{cm}^{-1}$. The high electric field is necessary for the onset of the avalanche process, and charge multiplication occurs in this localised high electric field region. The JTE comes into play here as the peripheral electric field is high and must be reduced by proper edge design. JTE is designed by a region connected to main implant but with a lower doping concentration. This results in the equipotential lines present in the bulk of the LGAD to spread-out from the implant region towards the surface, hence reducing high electric fields at the edges of the implant and the surface [62]. This subsequently extends the breakdown voltage of structure [63].
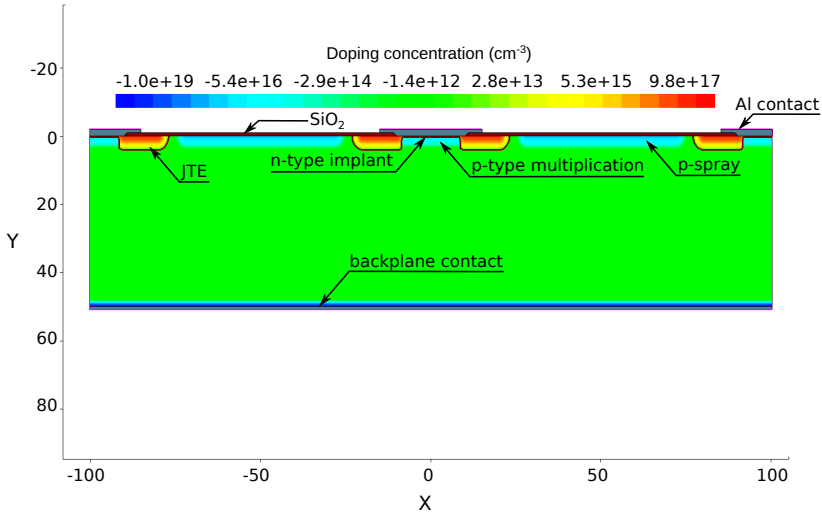
Figure 4.3: Cross-section of a typical LGAD, depicting the microstrip region with the n-implant and p-multiplication region. The bias is provided via the backplane contact, the strips are readout by the metal deposition on the n-type implant. The color bar indicates the doping concentrations across the LGAD region.

4.2.3 LGAD doping comparison

The p-multiplication implant is crucial in the electric field distribution, affecting the structure's gain and overall performance. This section compares doping types and their corresponding electric field and timing performance. There are three types when it comes to the type of multiplication implant: shallow, where the p-implant is broad and in contact with the n-implant, standard, where the p-implant is marginally in contact with the n-implant, deep, where there is a prominent gap between the n-implant and the p-implant as described in chapter 3. Such doping types are shown in Fig. 4.5.

The type of diffusion affects the gain obtained by the avalanche process. The profile is distinguishable when comparing the electric field at the junction of all three doping profiles. The shallow and standard doping has a short steep peak,
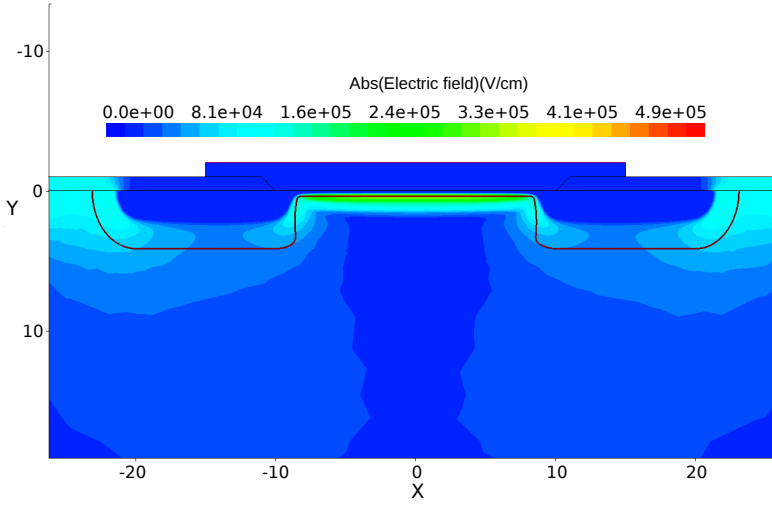
Figure 4.4: Electric field distribution at the junction of the n-type implant and p-type gain region. The peak electric field is slightly above $300 \, \text{kV} \, \text{cm}^{-1}$ which is the minimum field required for the avalanche process.
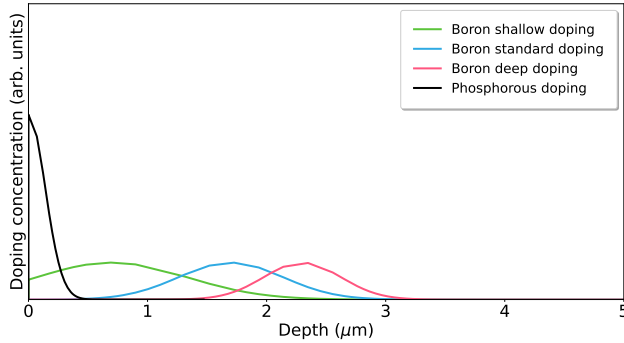
Figure 4.5: Doping concentration profiles for the implant regions for shallow doping (green), standard doping (blue), deep doping (pink). The main implant is an n-type semiconductor doped with Phosphorous, and the gain implants are p-type semiconductors doped with Boron.

whereas the deep doping profile has a broader plateau. In Fig. 4.6, the electric field

profiles extracted from the simulation can be seen[2]. A mean free path is an average distance traversed by a particle before changing its direction or energy. In an LGAD this region refers to the depth of the implant and gain region and affects the overall gain of the device. The relation between the gain of the LGAD G, the depth of the implant d and the impact ionization coefficient α is given in equation 4.1 [64], with E being the electric field strength, T being the temperature and ϕ being the fluence. The mechanism of charge multiplication has been explained in chapter 3. As seen from Fig. 4.6, the deep doping profiles provide higher mean free paths than the shallow and standard doping profiles. Hence for the same junction electric field strength, the gain of a device with deep doping concentration is higher than the other profiles.

$$G(E, T, \phi, d) \propto e^{\alpha(E,T,\phi)*d} \tag{4.1}$$
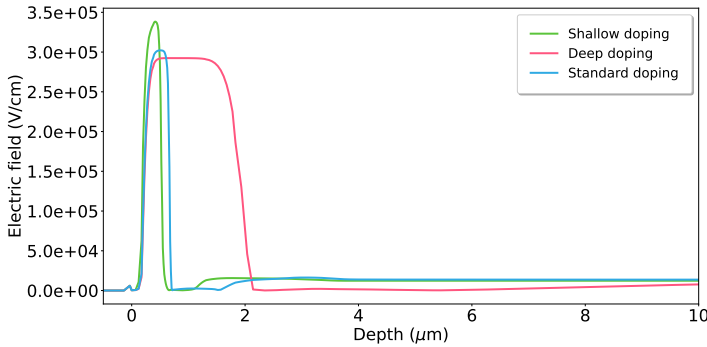
Figure 4.6: Electric field distribution for shallow doping (green), standard doping (blue), and deep doping (pink). The plateau, which results in a larger mean free path, can be seen for the deep doping device, unlike the sharp shallow and standard doping profiles.

The structure is front-illuminated by a narrow optical beam to study charge collection characteristics. The effect of the doping type on the charges collected by the node can be seen in Fig. 4.7. The structure with deep doping leads to a

---

[2]   The parameters such as the implant depth were varied to obtain similar peak electric field strengths.

higher charge than shallow and standard doping. The time required by the device
to reach a charge saturation is 500 ps.
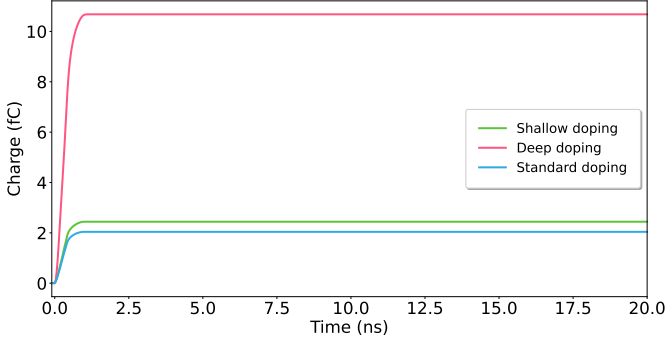
Figure 4.7: Charges generated by illuminating LGADs with different doping profiles. Due to the higher
mean free path in the deep doped LGAD, higher charges by a factor of five are generated compared to
the shallow and standard doped LGADs.

To simulate the signal formation in such structures, another 2D simulator tool called
Weightfield2 has been used [97]. This tool has the advantage of an easy interface
and fast calculations. The integrated front-end circuit helps in the analysis of the
transient behaviour of the sensor. Figure 4.8 shows the output of a charge-sensitive
amplifier connected to one of the implant's charge collection nodes. Fig. 4.8
shows the timing response of the devices with deep doping, shallow and standard
doping. To simulate the timing response, a generic CSA connected to a 2 GHz
scope was used in the Weightfield simulator. The peaking time of such a device,
regardless of the doping profile, is close to 1.14 ns. The timing performance shown
is highly dependent on the gain-bandwidth product of the CSA and hence is only
an estimated value.

A central problem associated with traditional LGAD structures with JTE is shown
in Fig. 4.9. The first problem is the width of the JTE itself which hinders
having microstrip pitch less the 100 m. Hence achieving the acceptable resolution
required in photon science applications is complex. The second is related to
charge collection in the presence of a JTE. The charge collection process for an
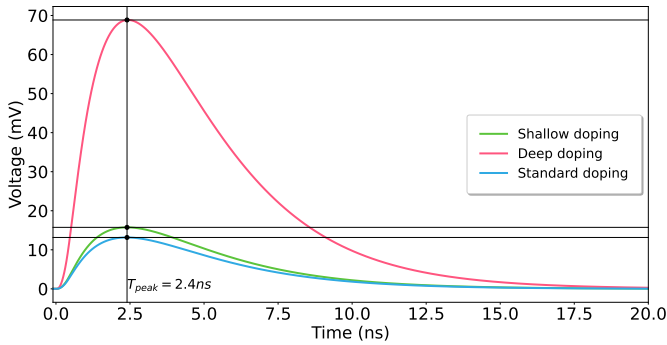
Figure 4.8: Signal formation after an amplifier stage for LGADs with different doping profiles. The time at which the signal reaches of the maximum amplitude is indicated.

optical beam incident on the centre region of the strip is shown in Fig. 4.9. The simulation indicates that the node collects most charges in 2.5 ns. However, it also presents one of the problems associated with this kind of LGAD structure. It can be seen that a significant part of the charges are pulled away from the gain region by the JTE, and only a small fraction of the charges pass through the gain region for multiplication. The charges passing through the JTE do not undergo any multiplication. One way to overcome or partially reduce the effect is to place the JTE slightly away from the gain region; however, this results in further degradation of the spatial resolution and the dead area between implants, resulting in a low fill factor (defined by the ratio of the active physical area to the active area of the microstrip sensor).

To overcome this limitation, an LGAD based on trench isolation (TI) has been developed within the RD50 collaboration and fabricated by FBK, Trento, in Italy. KIT contributed towards manufacturing microstrip sensors with pitch 50 and 100 m. The following section will introduce the sensors received by KIT and the initial characterization measurements.
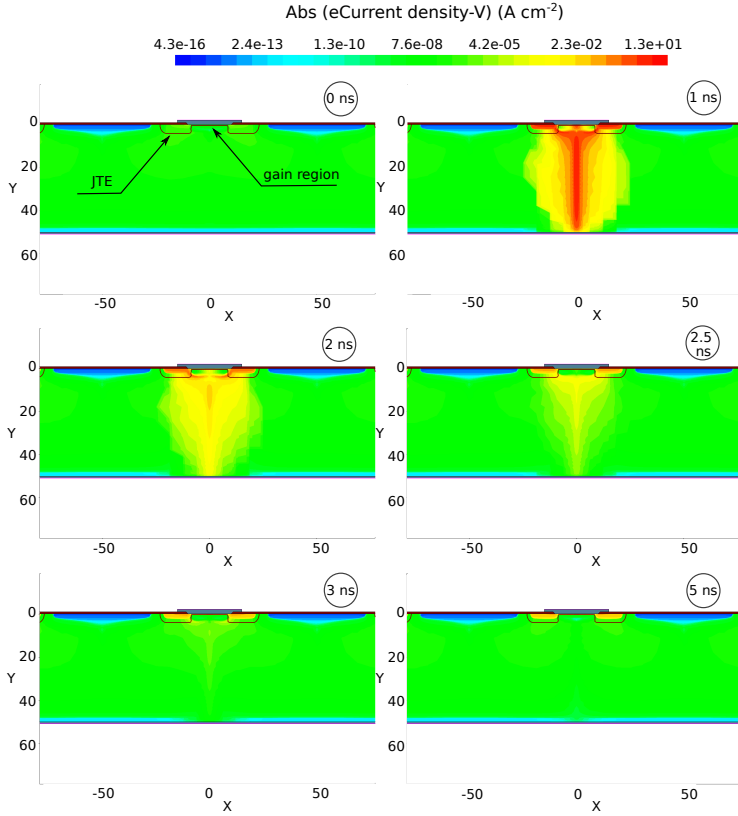
Figure 4.9: Electron charge density distribution in an LGAD upon the incidence of an optical beam over a period of 5 ns.

4.3 TI-LGAD

TI-LGADs overcome the limitations imposed by traditional LGADs concerning the spatial resolution and fill factor. In a TI-LGAD, the JTE is replaced by deep trenches filled by SiO_2. The trenches have a depth of a few microns and around 1 m in width. The trenches act as a physical barrier isolating the neighbouring strips or pixels, similar to the STI (Shallow Trench Insolation) of modern CMOS technology. The physical dimensions achievable with current fabrication technology allow higher spatial resolution. Figure 4.10 shows a detailed micrograph of a microstrip sensor based on TI-LGAD with a pitch of 50 m.
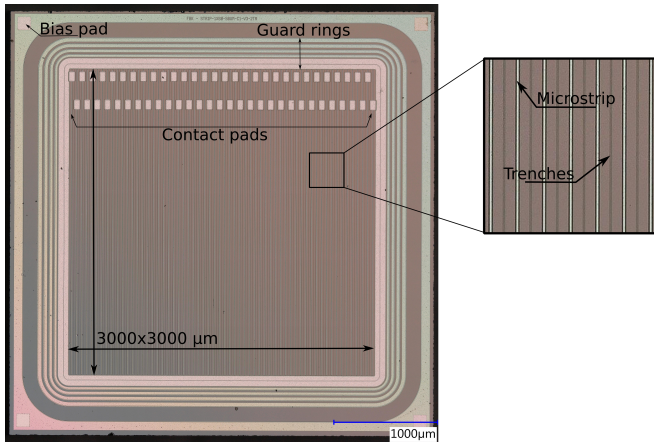
Figure 4.10: Microphotograph of a TI-LGAD. The complete sensor has an area of 3000 x 3000 m^2, the pitch of the microstrips is 50 m, and the sensor has metal limited only to the contact pads to reduce the reflectivity and thus improve the photon absorption efficiency. Front-side biasing is adapted for this structure and the guard rings provide a smooth potential drop across the edge of the sensor. This version has two trenches for isolation between the microstrips.
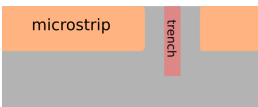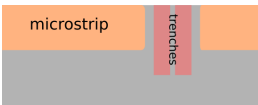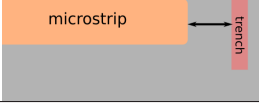
Contact type (C)	Trench version (V)	Number of trench (T)
C1	V1	T1
	microstrip trench	microstrip trench
C2	V2	T2
	microstrip trench	microstrip trenches
	V3	
	microstrip trench	

Table 4.2: Layout options implemented on TI-LGAD.

4.3.1 Layout options

Several geometries and process options were utilized in the fabrication of the sensor. The KIT version of the sensor included four types of microstrip sensors with an area of 4 mm × 4 mm, 2 mm × 2 mm and a pitch of 50 m, and 100 m. These sensors also vary in their layout with respect to features such as type of contact (C), version of the trench (V), and the number of trenches (T). This distinction is reported in Table 4.2. The layout combination received includes C1V3T1, C1V3T2, and C2V3T1. C1 is the code for the sensor with metallization distributed along the whole strip, whereas C2 has only two positions, one at each periphery of the strip. V1 is the code for the sensor where the distance between the trench and the strip is aggressive or minimal, V2 and V3 are the sensors with more distance applying a more conservative approach. T1 code is used for sensors that have one oxide-filled trench, while T2 is the sensor with two consecutive oxide-filled trenches

4.3.2 Initial sensor characterization

To study the dark current behaviour of the various TI-LGAD structures, a simple PCB with options to provide bias and grounding to the sensor has been fabricated. One such PCB with the mounted TI-LGAD is shown in Fig. 4.11. All three types of devices have been mounted and tested in ideal dark conditions at room temperature.
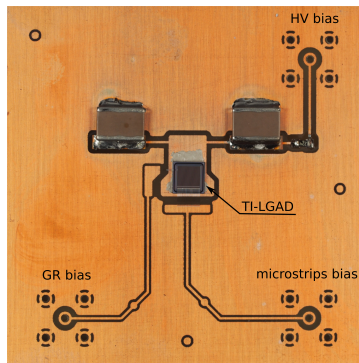
Figure 4.11: Test PCB with TI-LGAD sensor and various bias voltage conditions.

As seen in Fig. 4.11, there are three connections of interest, namely the HV bias where a reverse bias up to $-200\,V$ is given, the GR bias where the guard ring can either be left floating or given $0\,V$ and lastly the microstrip bias where all the microstrips are biased with $0\,V$ together. The bias voltage and grounding are provided by three separate SMUs (Source/Measurement Unit)[3]. To measure the dark current, negative reverse bias is applied and incremented in steps until an initial breakdown condition on the device is reached. The breakdown of the device is mainly recognised by the steep increase in the dark current measured by the SMU. While incrementing the bias voltage, the current measured by the other two SMUs connected to the GR and the microstrips is noted.

---

[3]   2x Keithley 2400, 1x Keysight Source Meter B2910BL are the SMUs used.
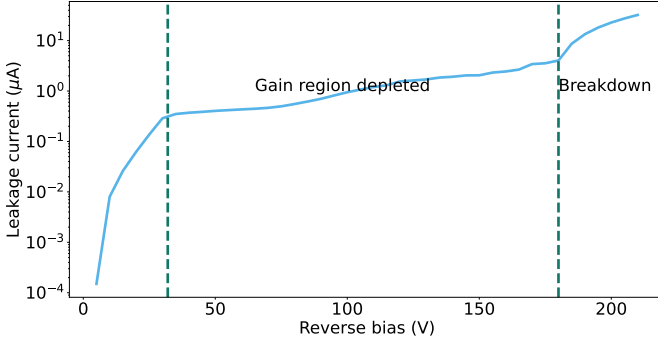
Figure 4.12: Dark current vs Voltage (I-V) characteristics measured for a TI-LGAD of type C2V3T1.

The measured currents from the SMUs should follow the formula below,

$$I_{bias} = I_{GR} + I_{microstrip} \tag{4.2}$$

Although this is just the verification process, the microstrip's current gives the active area's dark current. The dark current measured for one of the devices is shown in Fig. 4.12. It can be seen from the measurements that the dark current for this device is around 1 A for 64 channels. The device is completely depleted at a voltage of -30 V and it enters into the breakdown region at a voltage of -180 V. All structures listed in Table 4.2 show similar dark leakage current values. However, under constant illumination, the structures exhibit certain variations, see Fig. 4.13.

Figure 4.13 shows the I-V characteristics of devices with the two different contact types C1 and C2. It can be seen that the device with contact C1 has a higher strip current compared to contact C2, this could be because C1 has a higher surface area and collects more charges compared to C2. Hence C1 has better gain characteristics. Figure 4.14 shows the I-V characteristics of devices with two different trench types T1 and T2, T1 being a single trench and T2 being a double trench isolation between strips. It can be observed that trench type T1 has a better gain characteristic than double trench T2. One other characteristic visible in the I-V characteristics is the 'knee' specifically found in LGAD devices. This knee
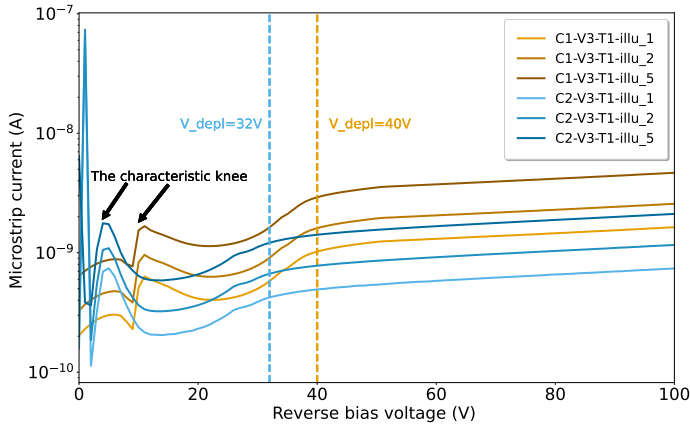
Figure 4.13: TI-LGAD comparing contact types C1 and C2. Lights with three illumination settings were used with 1 being the lowest intensity and 5 being the highest. Data by J. Deutsch.

can be found in the voltage region between 0 to 30 V. The first onset of increasing current occurs as the bulk of the LGAD is being depleted and the second occurs when the gain region is completely depleted. The dips in both the I-V curves are due to the trench isolation, also showing the transition into the completely depleted region. The sensor type with contact C2 reaches a fully depleted state at a lower voltage than contact C1. In the case of trenches, the T2 type reaches the earliest depletion. A more detailed characterization has been performed in the thesis of J. Deutsch [65].
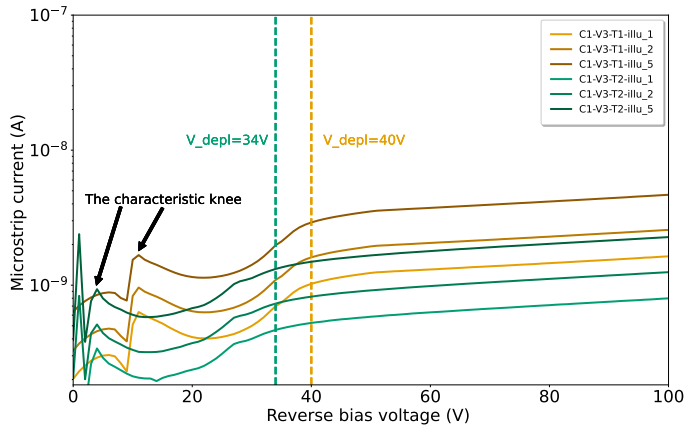
Figure 4.14: TI-LGAD comparing trench types T1 and T2. Lights with three illumination settings were used with 1 being the lowest intensity and 5 being the highest. Data by J. Deutsch.

4.4 Photon transfer curve characterization

For the majority of detector systems, noise is a limiting factor. This *Noise* is most times a measurable quantity. For detectors, there are two main categories for measuring noise, one under completely dark conditions (no ionization event), and the other under the influence of ionizing particles.

4.4.1 Photon Transfer Curve (PTC)

Photon transfer (PT) is a methodology employed to test, characterize and optimize solid-state sensors and camera systems. Table 4.3 enlists the sensor performance parameters that a PTC can extract. There are several methods to plot a photon transfer curve which are included in the photon transfer family in order to study the noise characteristics of a detector. One methodology that can be employed is to plot a log-log plot of the signal versus the noise. The signal intensity can be either measured from the source or can be extracted from the measurement from the detector in ADC counts (DN). It is also possible to plot the signal versus noise on a linear scale. In the following sections, the latter has been implemented for the photon transfer curve.

Performance parameter	Symbol/Unit
Quantum efficiency	QE (e^-/incident photons)
Charge collection efficiency	CCE
Dynamic range	DR
Readout noise (thermal noise)	σ_{read}
Shot noise	σ_{shot}
Signal non-linearity	NL_S
ADC sensitivity	$K_{ADC}(e^{-1}/DN)$

Table 4.3: Types of performance parameters that can be extracted from a PTC. Highlighted parameters in the grey sections have been calculated from the PTC measurements in the further sections.

The above parameters use absolute units, but the camera performance is measured in relative units in the form of Digital Numbers (DN) or ADC counts. In this chapter, the highlighted performance parameters will be measured and evaluated.

The function block diagram of an imaging system is shown in Fig. 4.15.
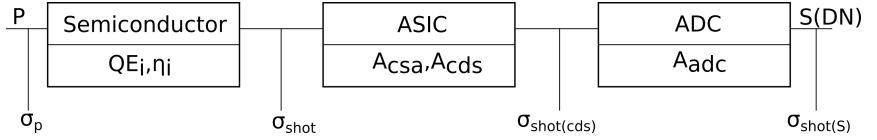
Figure 4.15: A typical functional block diagram of a camera.

The photon transfer function of this imaging system is given by,

$$\frac{S(DN)}{P} = QE_i \eta_i A_{CSA} A_{CDS} A_{ADC} \tag{4.3}$$

S(DN) is the signal generated at the output of the signal conditioning sequence block, P is the total number of input photons incident on the imaging system, $A_{CSA}, A_{CDS}, A_{ADC}$ are the gains of the individual blocks of the system. QE_i is the interacting quantum efficiency and η_i is the quantum yield gain (the ratio of electrons generated and the no. of photons incident). The product $QE_i \cdot \eta_i$ is referred to as the quantum efficiency (QE).

A typical PTC of a camera system is shown in Fig. 4.16. The first region corresponds to the random read noise measured under dark conditions. The second region corresponds to the shot noise measured with increased illumination on the camera. The third region corresponds to fixed pattern noise (FPN) and finally, the fourth region is the saturation region or full-well region [66]. A camera has several noise sources influencing the signal and variance.

- *Readout noise (σ_{read}):* Readout noise is a type of noise that affects the contrast resolution that a camera can achieve and is an accumulation of all noise sources independent of the signal. Lower read noise levels result in clearer images, as the camera can see smaller differences in signal amplitude. This is especially important in low-light situations, where smaller details
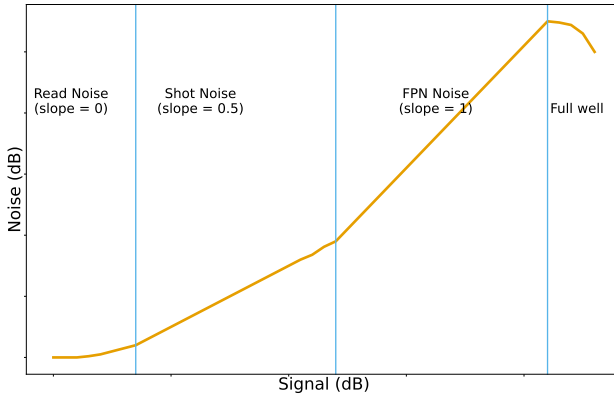
Figure 4.16: An example of a photon transfer curve with the different noise components.

are more easily detectable. Read noise is also essential in expressing a camera's sensitivity. A lower read noise level means the camera can see smaller contrast differences, which makes it more sensitive.

- *Shot noise (σ_{shot})*: Shot noise is a fundamental limitation in photodetectors and CCD cameras. It is a quantum effect due to the discrete nature of photons and electrons. This affects the overall SNR of the photodetector.

- *Fixed pattern noise (σ_{FPN})*: The generated photoelectrons are collected by the pixels of the photodetector. Pixel-to-pixel differs in sensitivity due to several fabrication defects or material impurities, causing the charge collection process to be different because some pixels collect charge more effectively than others. This noise is referred to as fixed pattern noise since it has the same spatial fingerprint from image to image and does not have a random effect.

Figure 4.17 shows the statistic distribution of the dark noise of the TI-LGAD-based KALYPSO measured by the acquisition of 10000 samples. This noise distribution

follows a normal distribution which is the case for detectors where the entire array/pixels are read out at once[4].
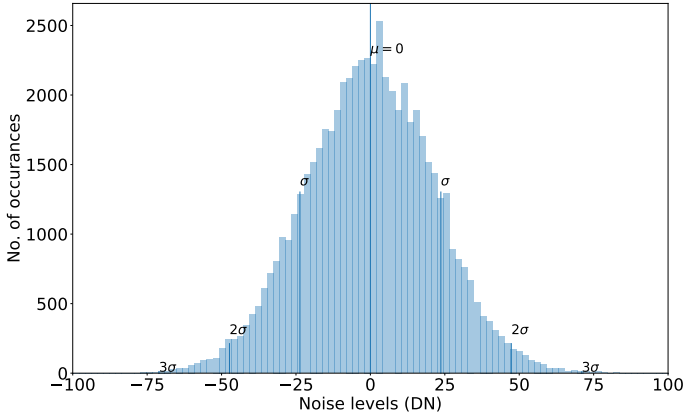
Figure 4.17: Statistical dark noise distribution of the TI-LGAD-based KALYPSO system at the highest gain setting.

4.4.2 PTC measurement steps

This section explains the procedure to plot a PTC for a line array camera. At first, the camera is set up with a fixed integration time and gain. In the case of KALYPSO, an integration time of 16 ns and the highest gain setting of 2 were used. All measurements are ideally performed in a dark environment. The base offset of the ADC is measured and subtracted from subsequent measurements. In the next step, the sensor is illuminated with a large FOV (Field of view) uniform light source [98]. A light source with a uniformity better than 1 % is necessary for FPN measurements. The average signal (averaged over strips/pixels) S is calculated for a fixed intensity, and the offset level is removed.

---

[4]   A CMOS detector has a readout circuit per column and hence follows a skewed distribution.

$$S = \frac{\sum_{px=0}^{px=N_{px}} S_{in}}{N_{px}} - S_{offset} \tag{4.4}$$

where N_{px} is the total number of pixels or strips, S_{in} is the signal without offset correction, S_{offset} is the averaged offset signal measured under dark conditions.

The noise for the signal σ_{total} is then found by calculating the standard deviation of S. Then the intensity of the light source is increased, and data sets are acquired for each intensity. This step is performed until saturation is reached. The steps are then repeated for the different gains of the camera.

For a PTC, the shot noise, FPN noise, total noise and the dynamic range is given by the following equations,

$$\sigma_{shot} = \sqrt{S \cdot \eta_i} \ \ and \ \ \sigma_{FPN} = P_N S \tag{4.5}$$

$$\sigma_{total} = \sqrt{\sigma_{read}^2 + \sigma_{shot}^2 + \sigma_{FPN}^2} \tag{4.6}$$

$$Dynamic \ range \ (DR) = \frac{S_{FW}}{\sigma_{read}} \tag{4.7}$$

where P_N is the FPN quality factor, S_{FW} is the signal at full charge capacity.

Figure 4.18 depicts the PTC measured for KALYPSO equipped with the TI-LGAD sensor at the highest gain setting. A linear fit has been performed on the measured curve. From the measurement, it is evident that shot noise dominates the detector. Fixed pattern noise is less evident or indistinguishable due to the short exposure time of 16 ns, as well as due to the CDS stage implemented in the Gotthard, which

accounts for the offset correction resulting from strip mismatching. From the formula (4.7), the dynamic range at this setting is calculated as follows,

$$DR(gain_2) = \frac{7250}{5} = 1450(DN) = 63.23 \text{ dB} \tag{4.8}$$
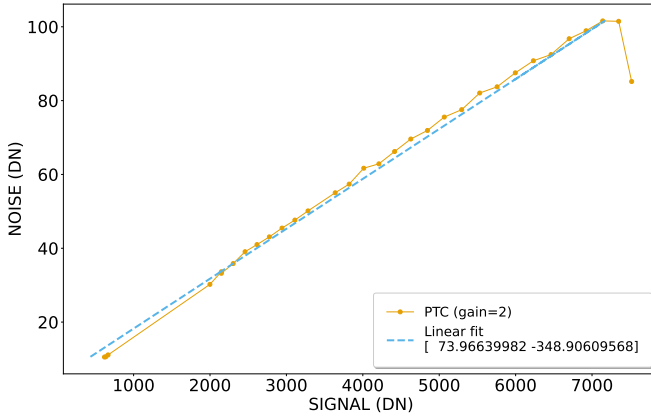
Figure 4.18: Linear fit applied to the PTC for the gain=2 setting. The difference in the slopes differentiates shot noise and FPN noise. The shot noise is the dominating noise source in this plot.

However, this system has three gain settings, with 2 being the highest[5]. Hence, the system sensitivity can be changed depending on the incoming light intensity. The measurements were then repeated for the three gain levels, and the PTC for the same is shown in Fig. 4.19.

Thanks to the high dynamic range of the detector at the $gain_0$, the full-well regime is not reached even at the maximum intensity setting of the light source. Hence it can be safely assumed that, if ever full-well is reached at $gain_0$, the maximum ADC count possible is 8192, making the ADC the limiting factor. Using the new full-well value, the overall output DR capability of the system is calculated to be 64.29 dB. Since a calibrated uniform light source is used to perform the PTC

---

[5]   The gain levels are in the ratio of 1:4:20.
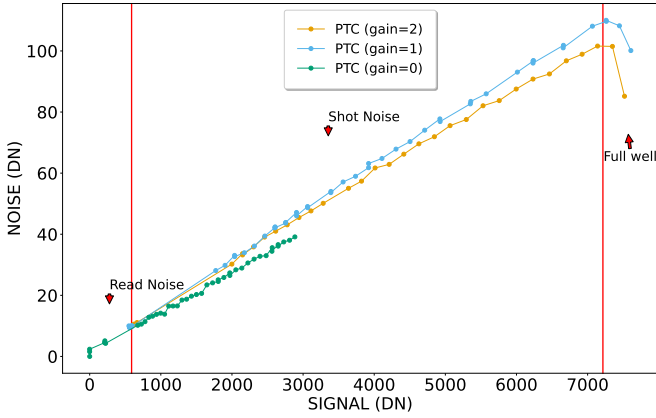
Figure 4.19: Photon transfer curve for all gain settings. This plot is used to calculate the overall dynamic range of the system.

measurement, it is possible to calculate the number of photons incident on the sensor. This can be done simultaneously by measuring the power of the varying light intensity with a power meter. The light output power is plotted against the corresponding ADC signal, and then applying a linear regression gives the relation between the light power P_i and ADC counts (in DN). The relation, thus, is found to be

$$ADC_{counts}(DN) = 15.2 \cdot P_i(\text{W}) + 171.4 \pm 5\% \tag{4.9}$$

In addition, a wavelength scan from a 400 nm to 600 nm was performed to select the wavelength with the highest intensity. The peak spectral component was measured as 450 nm. For this wavelength, a single photon has an energy of 4.4×10^{-19} W s. Using this, it is possible to calculate the theoretical responsivity R_{th} of the system at 450 nm, which is given by

$$R_{th}(\text{A W}^{-1}) = \frac{I}{P} = \frac{q_e \cdot \lambda}{h \cdot c} \tag{4.10}$$

For a wavelength of 450 nm, R_{th} is calculated to be 0.36 A W^{-1}. It can be concluded by definition that under ideal conditions when the external quantum efficiency (EQE) of the sensor is 100 %, the responsivity of the sensor is 0.36 A W^{-1} at 450 nm.

To subsequently measure the actual responsivity (R_{meas}) of the system, which is given by

$$R_{meas} = \frac{I_d}{P_i} \tag{4.11}$$

where I_d is the detector current and P_i is the power incident on the sensor. The I_d is calculated as follows: For an ADC code of 5700 DN, the analog voltage at the input of the ADC (V_{in}) is calculated as

$$V_{in} = \frac{V_{ref}}{2^{n-1}} ADC_{code} \tag{4.12}$$

V_{ref} is the ADC reference voltage equal to 1 V and n is the ADC resolution equal to 14. Hence V_{in} is calculated as 695 mV. This value can be converted to the charge seen at the input of the ASIC by the linear regression performed in subsection 4.4.3 and the gain of the Gotthard calculated to be 47.2 mV fC^{-1}. Using the calculated V_{in} in the gain of the Gotthard, the charge at the input of the Gotthard is calculated as 14.75 fC. The integration time set for these measurements is 16 ns. Thus the detector current I_d can be calculated as 0.9 A. The total light power incident on the sensor was 363.72 W and per microstrip element is 5.683 W which gives P_i. Finally, the R_{meas} can be calculated by substituting these values in equation 4.11 which results in an R_{meas} of 0.15 A W^{-1}[6].

The EQE for a photodiode is given by [67]

$$EQE = \frac{R_{meas}}{R_{th}} \tag{4.13}$$

---

[6] The Gotthard gain calculations were performed with the input signal being short pulse with a repetition rate of 2.7 MHz, in reality, the current generated by a microstrip detector follows a narrow Landau distribution.

Using the values calculated the EQE for a wavelength of 450 nm is measured to be 41.7 %.

To study the signal and noise response of the system with different exposure times, the average amplitude versus the integration time has been depicted in Fig. 4.20. The uniform light source had an output power of 113.63 W at a wavelength of 450 nm. A scan was performed at three gain levels to evaluate the linearity for each of these levels. The maximum integration time is limited to 68 ns, to accommodate the readout cycle of the ASIC. The minor fluctuations in the linearity beginning at 60 ns corresponds to the fact that the system is operating at the timing threshold of the readout cycle.
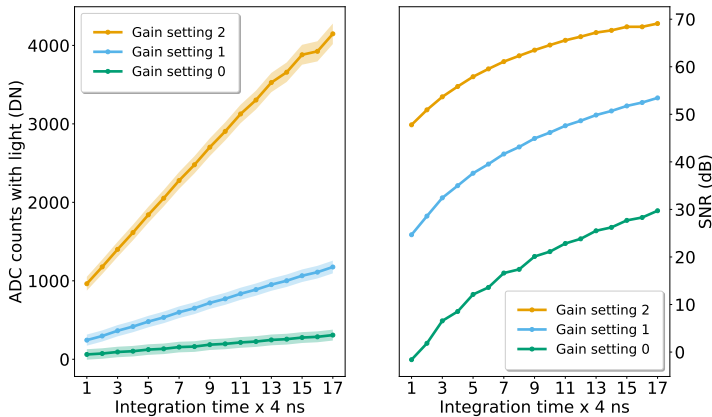
Figure 4.20: Evolution of signal amplitude versus increasing integration time. The sensor was uniformly illuminated with the same photon intensity for all three gain settings. The shaded region is the corresponding noise calculated for all gain levels.

Three gain settings can be activated by changing the feedback capacitance to either $20 \cdot C_f$ (gain 0), $4 \cdot C_f$ (gain 1) or $1 \cdot C_f$ (gain 2) where $C_f = 33$ fF. This is also a significant contributor to the system's overall dynamic range. The TI-LGAD sensor also has an internal gain, and the effect of this can be seen in Fig. 4.21. While studying the I-V characteristics, it is realised that keeping any of the microstrips floating leads to an unexpected sensor breakdown. With this system,

16 microstrips at the edge of the sensor were left floating due to the limited pads on the ASIC. Hence, the breakdown of this sensor is measured to be 60 V. Hence to be conservative, throughout this thesis, the measurements of TI-LGAD have been performed at a bias voltage of 45 V. On the plot, the first point highlighted refers to the point where the bulk of the sensor is depleted, and the second point is where the gain layer of the sensor is depleted. Hence the ratio between them gives an approximation of the gain at the working point (45 V) of the sensor. For the Gotthard gain setting 2, which is the highest setting, the working point of the sensor has a gain of 3. The factor between the lowest and highest Gotthard gain setting is 14.5. However, these values are just qualitative estimates, and to quantify the gain, a sensor structure similar to the one used for measurements, but without a gain layer needs to be used. But due to its unavailability during the measurements, only a qualitative estimate is reported.
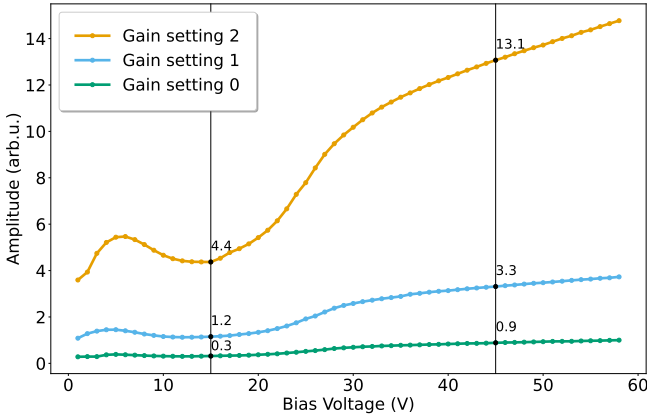
Figure 4.21: Scan of the signal amplitude for different bias settings, with uniform illumination.

4.4.3   Test characterization by charge injection

An alternate method of characterizing the system responsivity is by injecting a
test pulse into the ASIC to characterize the linearity and SNR. The Gotthard
has a dedicated test pulse connected to the input of the CSA of the Gotthard
in parallel to the sensor. A signal generator generates the test pulse with the
frequency of 2.7 MHz emulating the KARA signal. An internal test capacitor C_{in}
is implemented between the charge collection node and the test pulse input. If the
amplitude of the voltage injected is V_{in}, then the current at the input of the CSA is
given by $I_{in} = V_{in} \cdot C_{in}\delta(t)$. If C_{in} is 20 fF, and V_{in} is 200 mV, the injected charge
can be calculated to be Q_{in} = 4 fF. The voltage of the test pulse is increased from
200 mV to 1.2 V in increments of 100 mV. The digitized dataset with the sensor
biased and in a dark environment is taken for each voltage step. The measurements
were performed at the highest gain setting of the Gotthard.
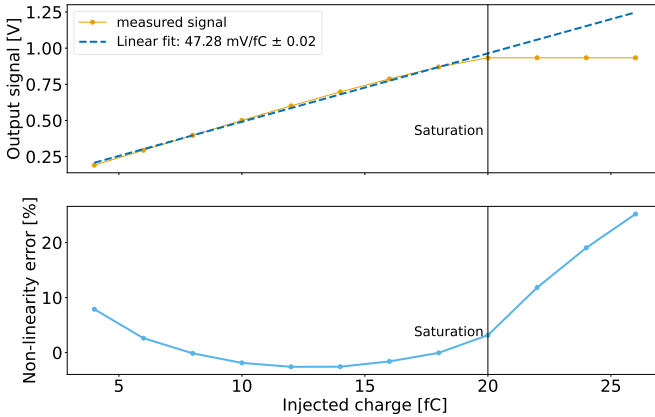
Figure 4.22: Test pulse characterization of the system: (top) Linearity of the system with the linear fit
plotted on top, gives a gain of 47.28 mV/fC. (bottom) The corresponding non-linearity error ranging
from 1 % to 5 % below saturation. The saturation is found to be 20 fC.

From Fig. 4.22, it can be seen that the output increases in a linear regime until
an injected charge of 20 fC, after which the Gotthard saturates. The gain of the
chip is calculated by linear regression and found to be $47.2{\pm}0.02$ mV fC^{-1}. The

corresponding non-linearity error[7] is calculated to be around 5 % for low charges and around 1 % for higher charges until saturation. The expected gain of the CSA is 33 mV fC^{-1} and the voltage gain on the output buffer is designed to be 1.5. Therefore the expected total gain is $33 \cdot 1.5 = 49.5$ mV fC^{-1}, which agrees well with the measured gain.

---

[7]   Non-linearity error is defined as the maximum deviation of the measured signal from the fitted curve/line.

4.5 Final integration of the Gotthard-KIT ASIC
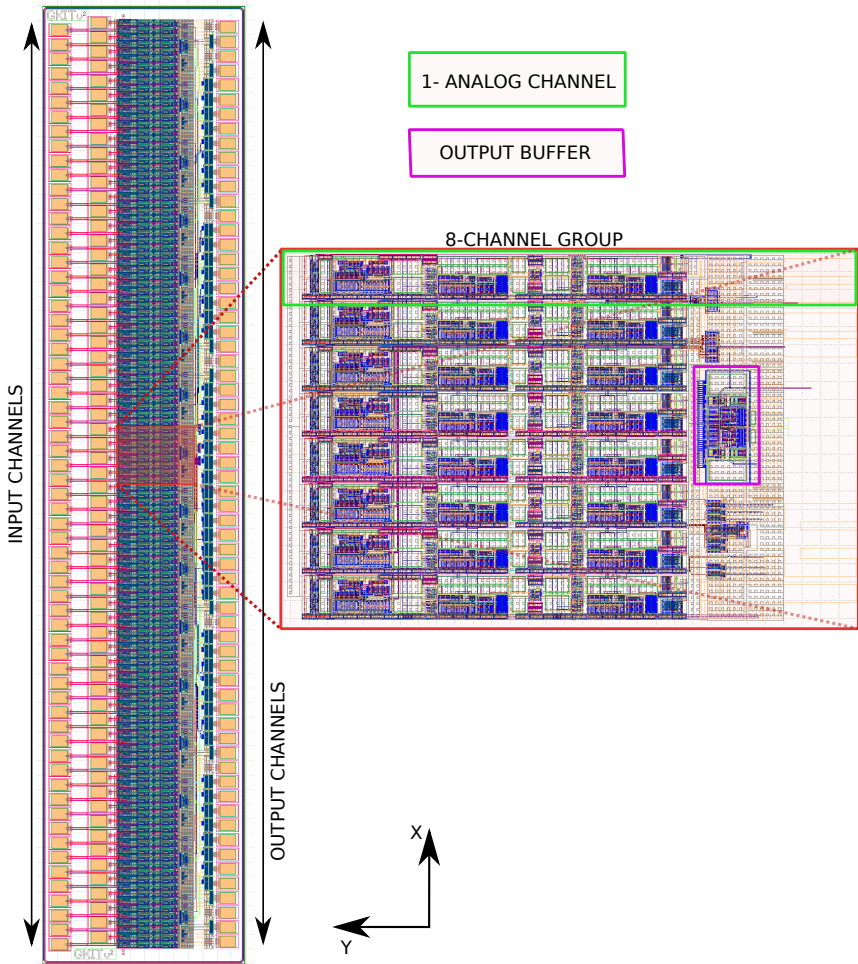
Figure 4.23: Complete layout of Gotthard-KIT (left). The highlighted window comprises a group of 8 channels shown on the right. A single channel is highlighted in the green box, the shared output driver is in the pink box.

A final version of the ASIC, developed during the thesis of L. Rota [31] using UMC (United Microelectronics Corporation) 110 nm process, has been completed to accommodate a larger microstrip sensor. The previously developed version, the Gotthard-proto, had 48 input channels and a maximum frame rate of 12 MHz. The new ASIC called the Gotthard-KIT version, consists of 128 input channels, 16 output channels, nine digital control pins, five analog bias pins and 15 pins for power supply and ground. The final chip features 16 groups of eight consecutive input channels each, see right of Fig 4.23. The analog readout chain has been implemented separately for each channel. In each channel group, the eight channels share a common output driver.

Figure 4.24 shows the layout of a single analog channel. The working principle of all stages has been described in section 3.3 of chapter 3. The gain-switching stage receives a digital control signal located in the region of the output channels, which switches between the three feedback capacitances implemented in the charge-sensitive amplifier (CSA). The output of the CSA is connected to the correlated double-sampling (CDS) stage. The output of the CDS is connected to the channel buffer. The D-type flip-flop at the output stage controls the flow of the analog signal from this channel to the output driver via an analog multiplexer. Each structure has been enclosed by p- and n-type guard rings that remove the parasitic superficial current path/leakages and prevent any latch-up occurrence. Decoupling between each channel is provided by placing an array of VAR capacitors along the analog chain. Metal-insulator-metal (MIM) capacitors have been implemented to filter the noise occurring in the power supply chain.

The last section of the ASIC are contact pads for interconnection either to the mezzanine card (on the right side) or to a microstrip sensor (on the left side). Compared to the previous Gotthard version, also developed in CMOS 110 nm technology, the number of output channels has been doubled. Hence custom pads have been implemented to arrange all signals in the final size of the chip. The pad size has been reduced to 150 x 88 m. Fig. 4.25 shows the layout of a single pad implemented in the ASIC. The input stage of the pad also has an ESD (Electrostatic Discharge) protection implemented by back-to-back diodes in CMOS.

The final fabricated chip from UMC was received in 2021, see Fig. 4.26. Unfortunately, due to a fabrication complication from the foundry, the Gotthard-KIT could not be tested. However, a new batch was received a few months into this thesis's writing and the test and characterization are foreseen to be continued, soon after.
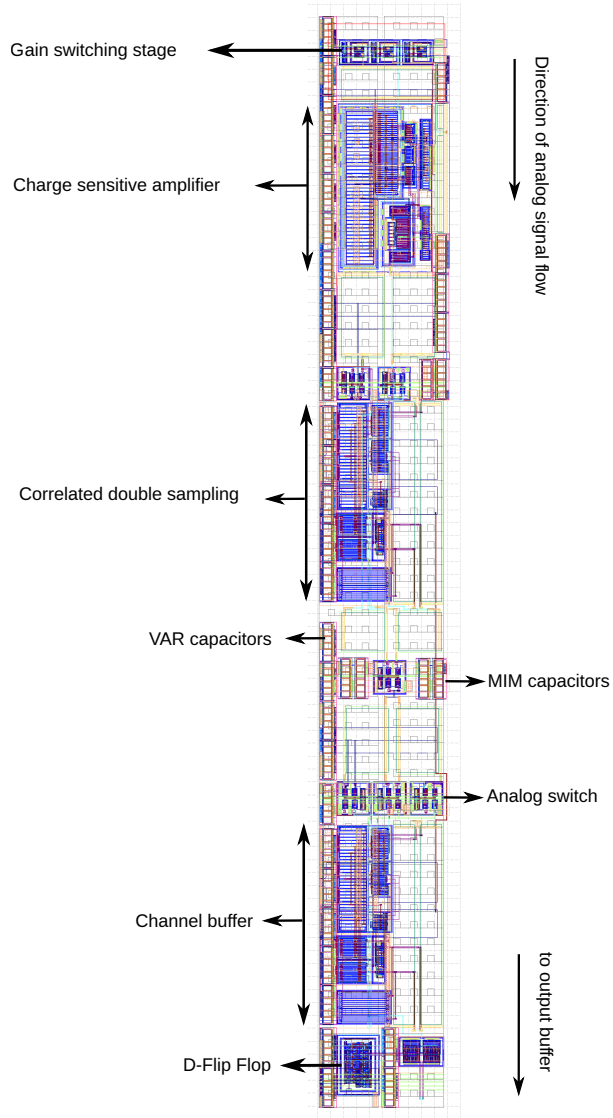
Figure 4.24: Layout of the analog readout chain of a single channel concluding with a digital D-flip flop for the channel transmission control.
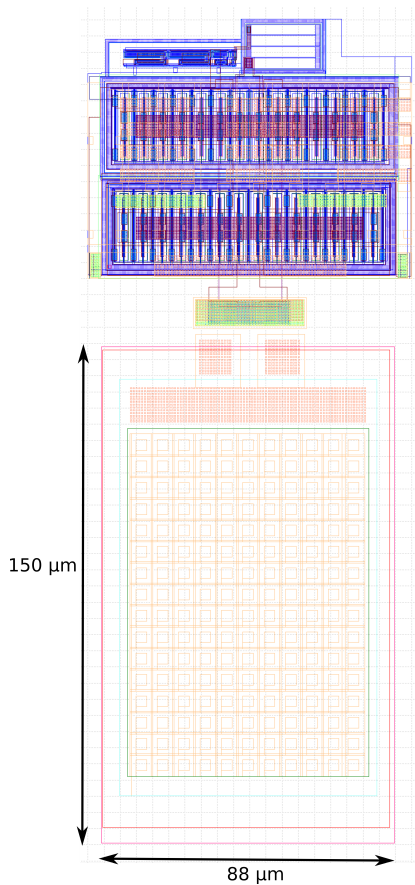
Figure 4.25: Layout of a single pad implemented for the output channel of the ASIC.
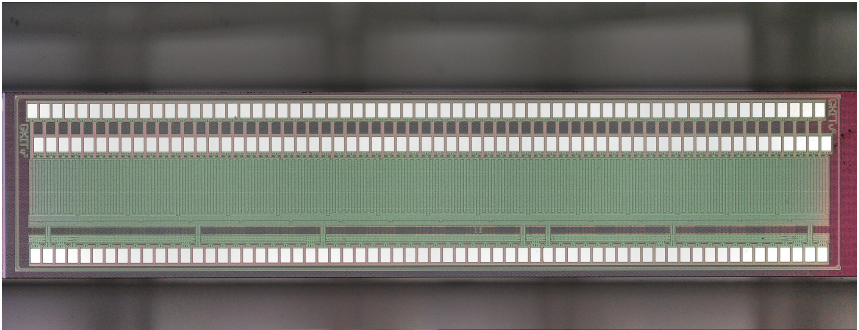
Figure 4.26: Micrograph of the fabricated Gotthard-KIT ASIC.

5   System Integration

KALYPSO is a hybrid microstrip detector that combines a high-granularity sensor with a low-noise and high-speed front-end ASIC to make an ultra-fast camera. Designing, producing and deploying such a detector requires various hardware and firmware developments. This chapter will explain the system integration process and how KALYPSO is brought to life.

5.1   KALYPSO detector

The current production version of KALYPSO version 2.5 can work at 3.1 MHz with a maximum of 1024 line arrays. KALYPSO version 3, working at 12 MHz, is under commissioning. This chapter will detail the detector card PCBs various sections, sensor to ASIC integration, ADC logic and its integration with an FPGA readout card. The readout card has been explained in detail in [68].

KALYPSO is a modular microstrip detector whose sensing element is a semiconductor microstrip sensor based on either Si, InGaAs, PbS, or PbSe. The front-end readout electronics are based on the technology of UMC 110 nm, which is suitable for applications that need radiation hardness. The rest of the elements on the PCB mezzanine card are designed using commercially available components and are assembled in-house at IPE (Institute for Data Processing and Electronics). The different elements of KALYPSO are explained in detail in the following sections.

The various versions of the KALYPSO family card have been depicted in table 5.1. The designing of the KALYPSO mezzanine card v2.5 and v3, decoding logic for output data, modifications for the Graphical User Interface (GUI), overall

Version	v2.1	v2.2	v2.5	v3
Frame rate	2.7MHz	12 MHz	2.7 MHz	12 MHz
ASIC	G-1.6	G-proto	G-1.6	G-KIT
No. of microstrips	256	48	1024/512	1024/512
Pitch	50 m	50 m	25 m	25 m
Type of semiconductor	Si, InGaAs, PbS, PbSe			

Table 5.1: Different versions of KALYPSO cards.

performance evaluation and final integration at the experimental setup was included as a part of the thesis[1].

5.1.1 Microstrip sensor

Figure 5.1 shows the KALYPSO mezzanine board. The board can consist of a microstrip sensor of either of the semiconductors described in chapter 3. The type of semiconductor employed depends on the application and wavelength to be detected. The sensor is connected to the ASIC Gotthard in an interleaved mode as described in Fig. 5.2a. This inherently allows the sensor to have a pitch of 25 m, while the pitch of the front-end ASIC pads is 50 m. However, it is also possible to use a single-sided sensor with a pitch of 50 m.

The sensor mounted on the detector card can be a dedicated silicon sensor, an InGaAs sensor from Hamamatsu, a PbSe sensor from Infrared [99] and PbS sensor from Trinamix [100], see Fig. 5.3.

The Si microstrip sensor mounted is a p-in-n type sensor with the possibility of front and back illumination. The front side of the microstrip sensor consists of minimized metalization to reduce the surface's reflectivity [69]. The surface has contact pads for bias to the sensor and the possibility of grounding the inner guard ring. A reverse bias of up to 140 Volts may be provided to the sensor to establish a strong and uniform internal electrical field. Figure 5.4 shows the I-V

---

[1]   v2.2 is a test version for evaluating sensors and ASICs.
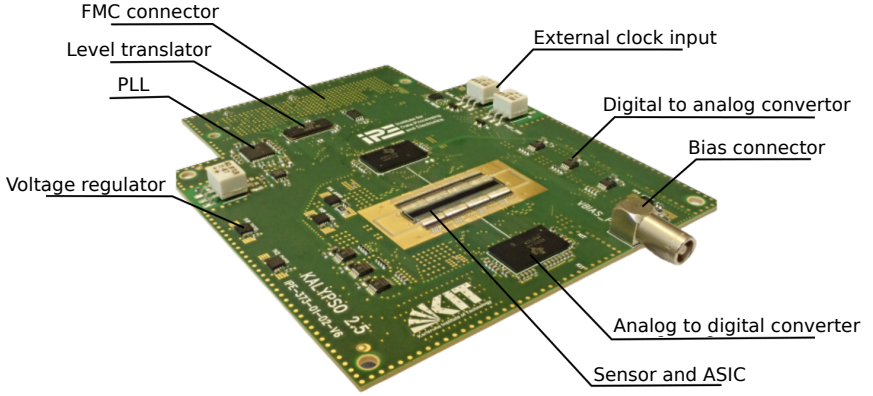
Figure 5.1: A fully assembled KALYPSO mezzanine board v2.5 with Si sensor and optimized sensitivity towards visible light.

characteristics of the sensor. The bulk of the sensor is completely depleted after a voltage of 45 Volts. Beyond the depletion voltage, the leakage current of the sensor remains almost constant, and at a voltage greater than 140 V enters into a breakdown region. The breakdown voltage of a microstrip detector depends on various factors, including the structure (strip geometry, guard ring design and their respective doping concentrations), the thickness of the bulk and the doping profiles of the P-N junction.

A custom Si wafer consisting of various structures is shown in Fig. 5.2b. This wafer has a diameter of 150 mm. Minimizing the surface's reflectivity is one of the most critical processes to improve the Si sensor's overall efficiency. This is performed during the sensor's fabrication with a Silicon Nitride (SiN_x) layer, which acts like an anti-reflection coating (ARC). SiN_x helps in not only optical transmission but is also very efficient in surface passivation. Figure 5.5 shows the absorption efficiency measurements performed on three Si diodes with ARC for different spectral sources along with their respective theoretical calculations. The measurements show that the absorption efficiency follows the regime of the corresponding theoretical calculations with an offset. The offset is accounted for by the thickness of the wafer taken into account for theoretical calculations. The

(a)   (b)
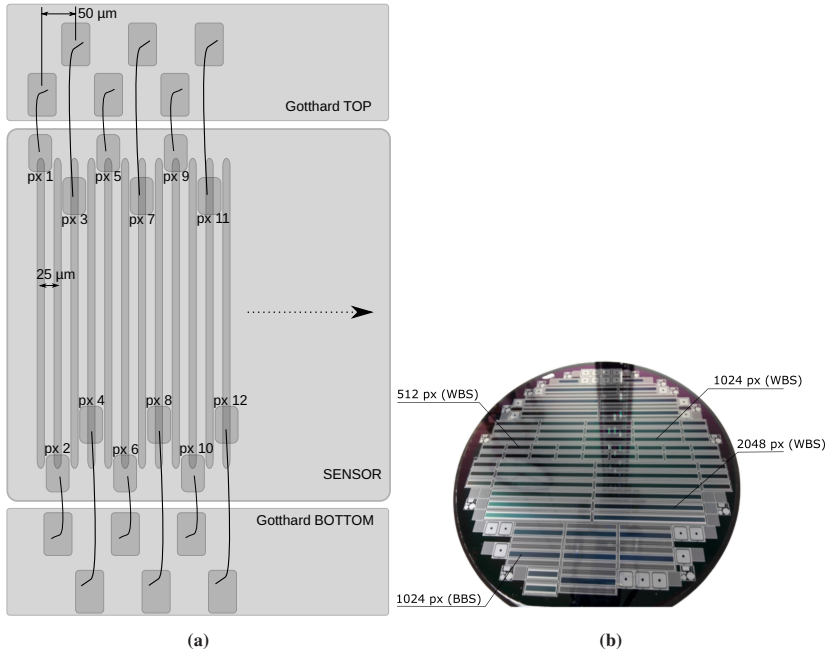
Figure 5.2: (a) Schematic for the microstrip sensor design, placement and wire-bonding plan. (b) Complete silicon wafer with the designed microstrip sensor topology.

NIR structures have an average of 90 % efficiency, the visible structures have an average of 85 % efficiency, while the NUV structures have a uniform efficiency of 72 % throughout the entire spectral range [70]. The Si microstrip part of the complete wafer was simulated and designed at the Institute of Data Processing and Electronics (IPE) by the author.

5.1.2 Front-end ASIC

The microstrip sensor is connected to the front-end ASIC Gotthard with a high-density aluminium wire-bonding process. The Gotthard works at a frame rate of 2.7 MHz. It features 128 input channels, eight analog output channels, digital control channels and analog bias channels. This ASIC is a modified version of the
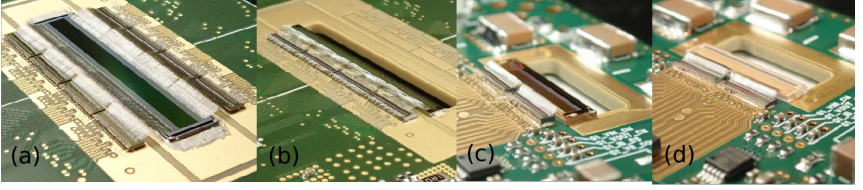
Figure 5.3: KALYPSO mounted with microstrip sensors based on (a) silicon, (b) indium gallium arsenide, (c) lead sulfide, (d) lead selenide.
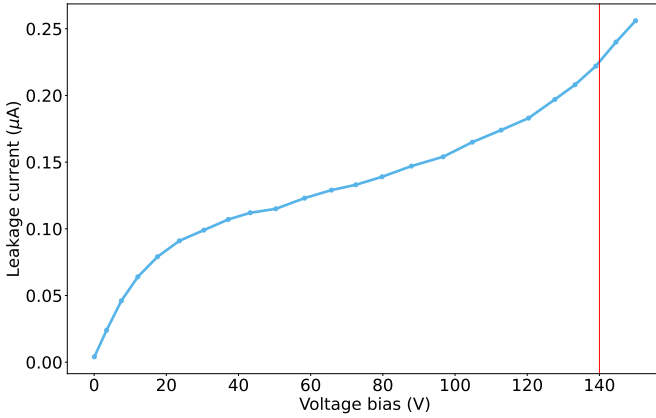
Figure 5.4: I-V curve measured for a 1024 microstrip Si sensor in dark conditions. The red line indicates the breakdown voltage of the sensor.

Gotthard chip designed at PSI [71]. The Kalypso v2.5 card mounts four/eight of these Gotthards, covering a sensor with 512/1024 channels. The readout sequence of the Gotthard is shown in Fig. 5.6. The operation logic is as follows:

- RESET acts on the CSA, and when set high (1), the charge on the feedback capacitance is reset. When set to low (0), the integration starts and waits for an event, i. e. laser pulse.

- DS_SW2 is set to low (0) to stop the integration and sample the analog signal at the output of the CSA before transmitting the signal to the analog multiplexer.
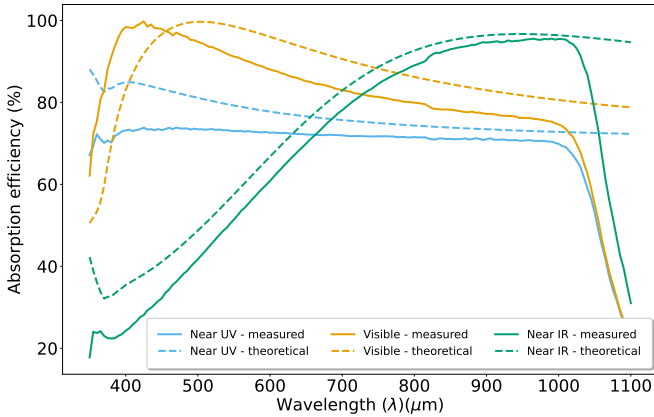
Figure 5.5: Absorption efficiency measurements performed on diodes with NUV, visible and NIR spectral regions.
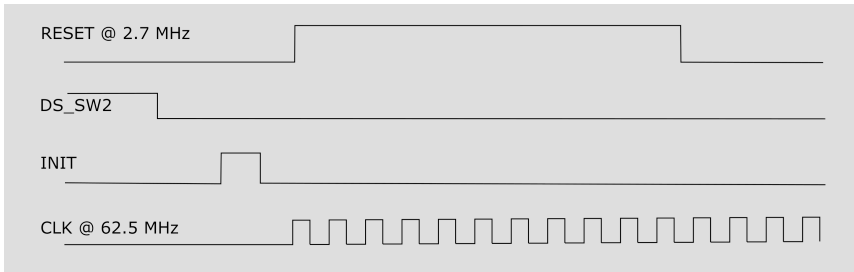
Figure 5.6: Readout logic sequence for the Gotthard ASIC.

- INIT is set to high (1) to start the initialization of the readout sequence. At every clock cycle, analog data from the 128 channels will be transmitted onto the differential output pair of the Gotthard.

- CLOCK: The frequency of the Gotthard clock decides the overall framerate of the device. For KARA, the clock is set to 62.5 MHz, which results in a maximum frame rate of $1/0.32$ s $= 3.1$ MHz. The clock is activated only during the readout phase to minimise the induced noise. A total of 16 clock cycles are needed to read out all the 128 input channels of the Gotthard.
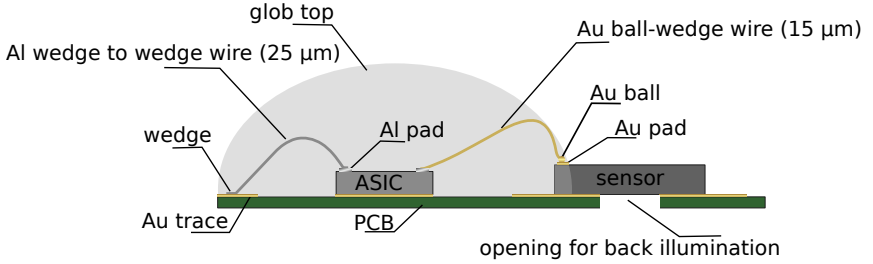
Figure 5.7: Schematic of different types of interconnection and packaging technologies.

5.1.3 Wire-bonding techniques

Wire-bonding is a technique used extensively for electrical interconnection between semiconductor chips. It is a method by which a soft wire of small length and diameter is attached to a metallic surface without solder or flux. Metals compatible with wir-bonding include Gold (Au), Copper (Cu), Aluminum (Al), etc.

In KALYPSO the high-density connections between the readout ASIC and a semiconductor microstrip sensor are performed by a wire-bonding process. The ASIC and the sensor are glued to the mezzanine card with electrically conductive epoxy glue (PC3001 Heraeus). Optionally, a two-component adhesive (Araldite) could also be employed to keep the silicon bulk insulated from the PCB ground. The choice of glue depends on the backplane conductivity of the sensor as well as the maximum temperature the sensor can be subjected to for curing the glue. Silicon and InGaAs sensors can have metalized backplanes and be subjected to high curing temperatures of 120 °C. Hence conductive glue is used. However, PbS and PbSe cannot be subjected to temperatures above 70 °C. Hence the two-component glue with curing at room temperature has been used.

There are two types of wire-bonding processes: thermosonic bonding and ultrasonic bonding. Figure 5.7 illustrates two types of bonding techniques utilized for KALYPSO. The first is a thermosonic process by gold (Au) ball-wedge bonding process, where a gold ball is deposited on the metal pads of the sensor. A gold wire bond is created between the ball and the corresponding destination pad, where a wedge shape bond is formed. Such a process is utilized, especially where there
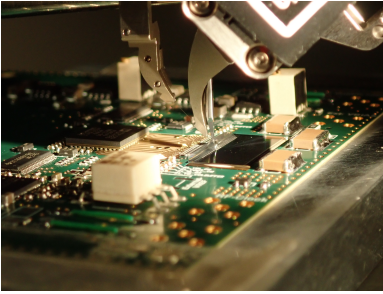
Figure 5.8: KALYPSO under wirebonding process.
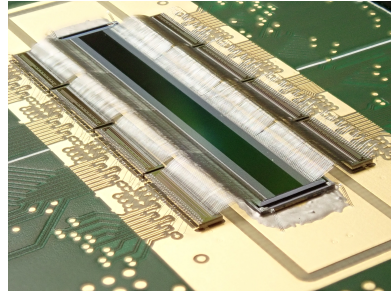
Figure 5.9: Fully bonded KALYPSO with a total of 1024 microstrip channels.
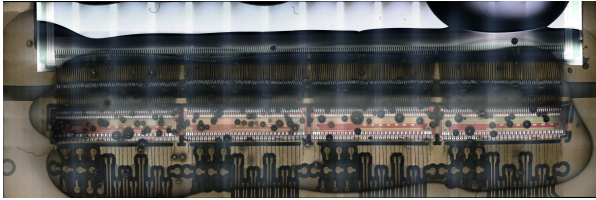
Figure 5.10: Glob top encapsulation to protect high-density interconnects.

is a high risk of lift-off of the metal pads. The second type is a ultrasonic bonding is aluminum wedge-wedge bonding, which relies on ultrasonics to form bonds, see Fig. 5.8.

Figure 5.9 shows a KALYPSO card mounted with a Si microstrip sensor with 1024 strips and 4 Gotthard ASICs. The wire used for the Al wedge-wedge bonding is 25 m. This allows for such a high-density interconnection for the sensor with a pitch of 25 m. With 1144 bonds per KALYPSO, handling sensitive wire bonds becomes a challenge. To protect the bonds from damage during testing or transportation, a glob top made of an epoxy sealing compound is applied [101]. See Fig. 5.10.

5.1.4 Analog to digital conversion

The analog signals from the Gotthard ASIC are connected to the inputs of an ultra-fast ADC. KALYPSO mounts a commercial ADC from Texas Instruments

ADS52J90 [102]. This ADC can sample 16 parallel channels or 32 channels in a time-interleaved mode. The analog signals are sampled at a sampling rate of 62.5 MHz with a resolution of 14 bits. The ADC can be equipped with up to 16 parallel LVDS outputs interface or up to 8 JESD serial output interface each one operating up to 5 Gbps. The serial JESD interface is employed in the current design as the former is impossible due to the limited LVDS connections on the FMC banks. Since each Gotthard has eight outputs and 128 inputs, for the readout of a microstrip sensor with 1024 channels, it is necessary to integrate 8 Gotthards and 2 ADCs. Due to the compactness of the JESD interface only 8 CML output channels are routed to the FMC, four JESD for each of the two ADCs.

5.1.5 PCB layout design

The PCB layout has been designed considering several mixed-signal circuits integral to the board's overall performance with respect to susceptibility to noise and crosstalk. The PCB consists of 12 layers with both analog and digital circuitry. Figure 5.11 shows the complete routing design for KALYPSO depicting the complex nature of the PCB design. Good layout design practice requires the analog and digital sections to be isolated to reduce capacitive cross talks and emissions due to electromagnetic interference/radio-frequency interference (EMI/RFI) noise.

Figure 5.12 shows the 'analog ground plane island' that includes the microstrip sensor, Gotthard ASIC, input signal of the ADC, analog voltage supplies, and analog voltage/currents references, i. e. bias output generated by the DACs. The 'digital ground plane' includes the digital output signal of the ADC, the Phase Locked Loop (PLL), the level translator, digital power supply blocks, and the FMC+ connector. A ferrite bead is used to provide a DC connection between the analog and digital plane and isolate them at high frequencies where the ferrite bead presents a high impedance.

Other layout practices that have been followed in the design are as follows:
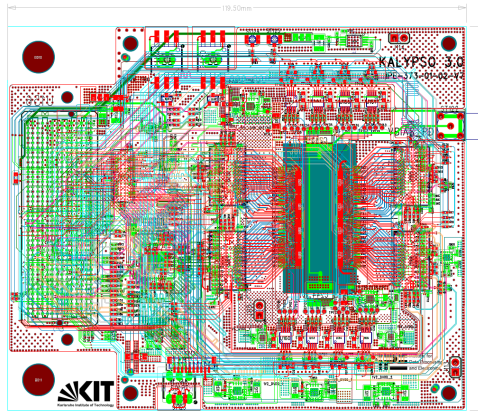
Figure 5.11: A composite layout of KALYPSO depicting the routing performed in the 15 layers of the PCB. Each colour is associated with an individual layer.
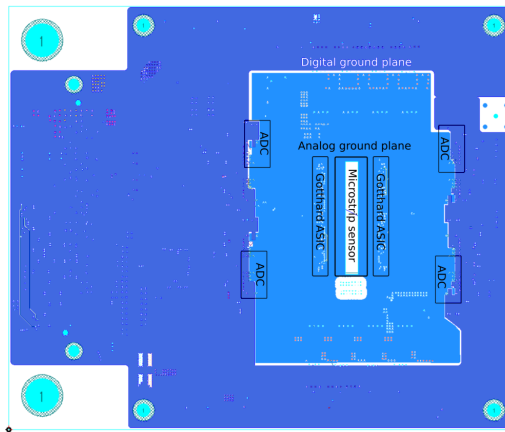
Figure 5.12: Analog and digital ground plane distribution for low noise interference.

- Follow the current return path: Currents flow from source to load and then back via a return path, and this return path is often the ground. Hence every trace is ensured to have a corresponding ground plane underneath it to ensure the best signal integrity.
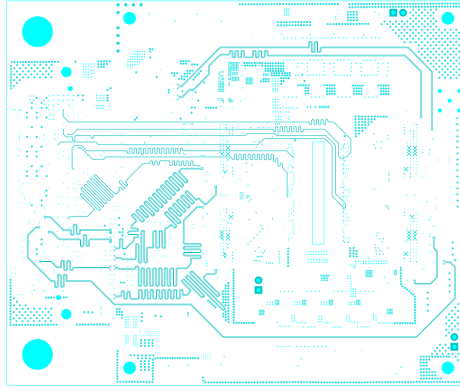
Figure 5.13: High-speed differential signal routing of KALYPSO.

- Bypass capacitor: Each power supply pin has been allocated a bypass capacitor, which is placed close to their assigned pins to reduce the noise generated during the digital or analog operation of the ASIC.

- Trace isolation: the digital and analog traces are isolated from each other to avoid cross-coupling.

- Length matching: groups of high-speed differential lines and clock lines are routed with equal lengths with none to minimum tolerance to reduce the time skew and terminated with a $100\,\Omega$ differential impedance, see Fig 5.13.

- Power supply: The digital and analog power supplies are separately placed in their respective regions and along the outer edge of the PCB.

5.1.6 FPGA firmware

An FPGA-based readout card, 'Hi-flex' performs the data processing of KALYPSO. This readout card is based on a Virtex-7 FPGA by Xilinx. KALYPSO is connected to Hi-flex by a standard FMC-vita connector. The data and control signal flow from Hi-flex to KALYPSO and vice-versa is shown in Fig. 5.14.

The accelerator timing distribution provides timing signals for synchronising the system's data acquisition. At KARA, the revolution signal is 2.7 MHz. The signal *FT-Fast Trigger* defines the rate at which samples are acquired by the Kalypso detector system. At startup, a delay time scan is performed to find the synchronization between the incoming light pulse and the integration time interval of KALYPSO. The best delay is selected by the user, which is then applied as a phase change to the *Fast trigger*.

When several detectors are mounted at different experimental stations, a dedicated timing signal called *ST-Slow Trigger* synchronises their data acquisition. The *ST* at KARA is 0.1 Hz. When *ST* is enabled, every acquisition cycle will begin with its rising edge. Every acquisition cycle has a certain number of samples, from 100 to 10 million, which the user can set. Each of these samples in one cycle is acquired at the rate of *FT*.
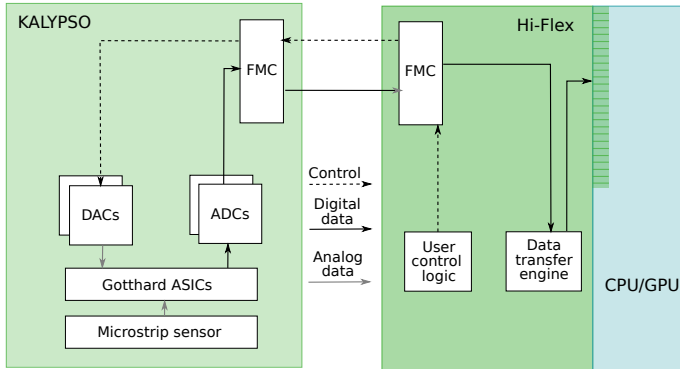
Figure 5.14: Data, timing, and control signal flow implemented in the firmware logic of KALYPSO.

Figure 5.14 shows an overview of the timing, data, and control signal distribution within KALYPSO and through the Hi-flex interface.

- The FT, ST, and the global RF signal (62.5 MHz) are fed into the KALYPSO card or can also be directly connected to the IO pins of the Hi-flex. The

RF signal is provided as an input to the onboard PLL, which distributes phase-synchronized outputs to various board sections.

- The control signals like Gotthard control, SPI (Serial Peripheral Interface) for ADC/PLL, and I2C (Inter-Integrated Circuit) for DACs are provided by dedicated logic and FSM (Finite state machine) modules implemented in the FPGA.

- The raw analog data is converted to digital format and then transferred to the CPU (Central Processing Unit)/GPU (Graphical Processing Unit)/Memory by a DMA (Direct Memory Access) engine implemented in the FPGA [72, 73].

The timing distribution is explained in detail in Fig. 5.15. It is an example schematic which is satisfies the timing requirements of KARA.
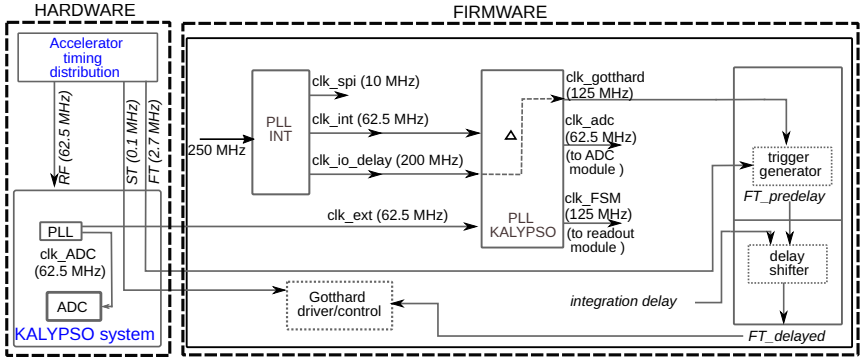
Figure 5.15: A detailed timing distribution scheme for the operation of KALYPSO.

The accelerator timing distribution provides three signals, namely RF signal (62.5 MHz), which is the central clock that synchronizes the accelerator to KA-LYPSO, FT (2.7 MHz) is the rate at which single shot measurements are acquired, ST (0.1 Hz) is the rate at which the single-shot auto acquisition mode occurs. The onboard PLL distributes the synchronized signal (62.5 MHz) to the ADCs on board. It also provides the signal (125 MHz) for the Xilinx GTH transceivers located on

Hi-flex. Additionally, a feedback clock clk_ext (62.5 MHz) is provided to the FPGA. The FPGA firmware consists of two MMCMs (Mixed-Mode Clock Manager). The two MMCMs can work independently or in a master-slave configuration. The 'PLL INT' is driven by the user clock which is also the reference clock that drives the entire user logic with a frequency of 250 MHz. ADC and PLL work based on the SPI interface and are provided with a 10 MHz signal. The 'PLL KALYPSO' drives the firmware's ADC, Gotthard control, and FSM (Finite State Machine) modules. The clk_adc and clk_gotthard need to be aligned with a specific phase delay to ensure the ADC samples the data precisely. Hence the phase of the clk_gotthard is tunable by the user with a picosecond precision.
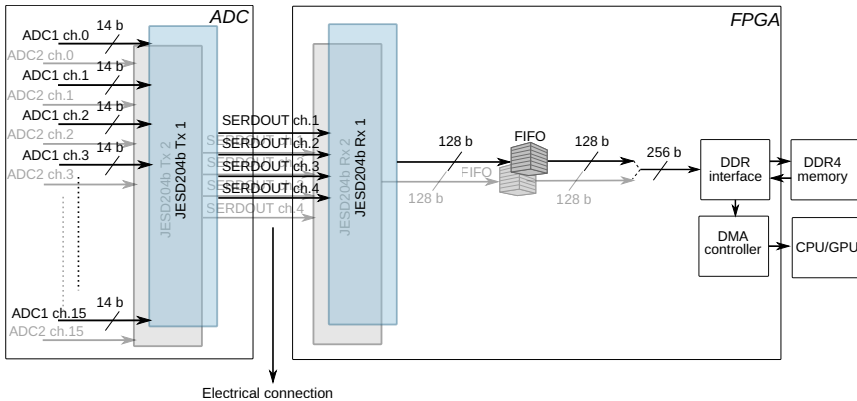
Figure 5.16: Schematic of the digital data flow from KALYPSO to the FPGA.

The digital data readout stage is illustrated in Fig. 5.16.

- The ADC ADS52J90 has 16/32 analog inputs that are converted to 14-bit data. The digitized data are processed by the JESD204b Tx engine, which converts the parallel data into high-speed serial data.

- This serial data are transferred to the FPGA by four CML differential lanes.

- The JESD204b Rx engine, located at the FPGA, de-serializes this data into 128-bit parallel data that are stored in the local FIFO memories. Since

there are two ADCs mounted on KALYPSO, the total data that needs to be transferred is 256 bits per physics event.

- This is transferred to the DDR memory, which stores the data temporarily until they are transferred to the DMA controller.

- The DMA controller then transmits the data to external memory, CPU/GPU for further processing and decoding.

The internal structure of the JESD204b Tx/Rx engine is shown in Fig. 5.17. For simplicity, only a single input channel is shown.

- Each analog differential pair input is converted to a 14-bit digital data.

- This is packed into octets (8x2 words).

- Scrambling can be optionally enabled to reduce EMI (Electromagnetic interference) effects by distributing the spectral peaks.

- The (8x2 words) octets are then encoded into 10x2 words by the 8b/10b encoder. This step adds additional overhead but provides DC-balanced output.

- The serializer converts the (10x2 words) data into serial data transmitted to the JESD204b Rx engine by a CML transmission line.

- At the JESD204b Rx engine located in the FPGA, the data is processed through the amplifier/equalizer, CDR (Clock and Data Recovery), De-serialize/Decode/Descramble blocks, and finally transmitted for further processing or storage.

The lane rate is the bit rate for a single lane of the ADC interface can be calculated as follows,

$$Lane\,rate = \frac{M \times N' \times [\frac{10}{8}] \times F_s}{L} \qquad (5.1)$$

where M is the total number of ADC converters, N' is the total number of data bits, F_s is the device clock, L is the total number of CML output lanes, the factor $10/8$ reflects the factor due to 8b/10b encoding [103].
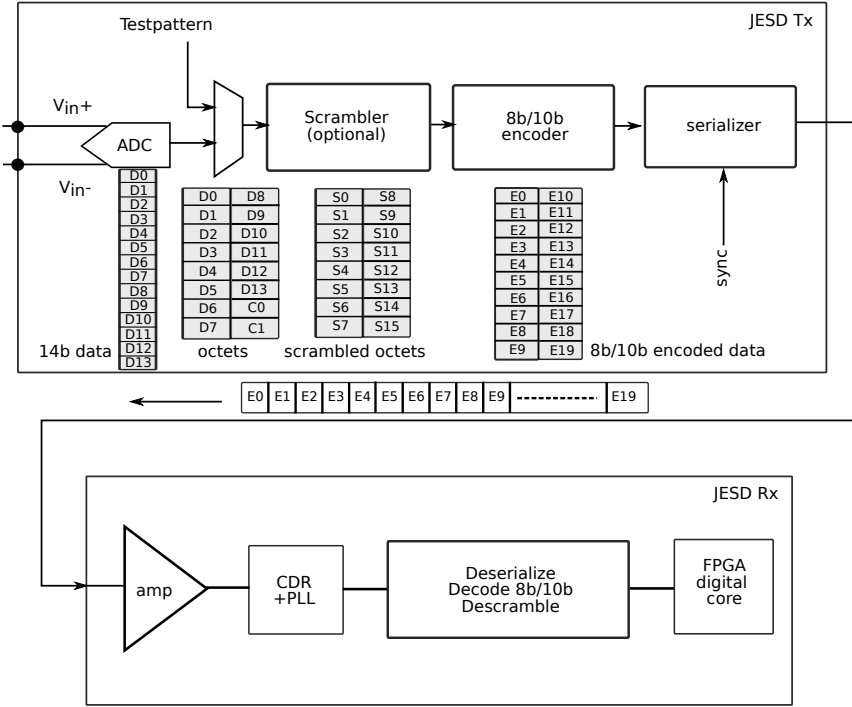
Figure 5.17: Schematic of the JESD serialiser/deserializer. Adapted from [103].

In the case of 512-pixel mode where 16 channels per ADC is used, $F_s = 62.5\,\text{MHz}$, M is 16, N' is 16, L is 4, which gives a *lane rate* of 5 Gbps. In total, with 2 ADCs, the total throughput is 40 Gbps.

5.1.7 Graphical User Interface

The KALYPSO detector can be controlled, and the data acquired visualized in real-time by a custom Graphical User Interface (GUI). This GUI has been designed within the framework of PyQt3 [104], and the visualization is based on pyqtgraph [105]. The user can also store the data in the working system through this interface. In the background, the GUI performs actions by executing the bash commands for

control and acquisition. The data acquired can be visualized in 1D and 2D modes. Unlike its predecessor, KALYPSO v2.5 does not have a data sorter implemented in the readout sequence. Instead, the data sorter has been included in the data acquisition part of the GUI.

The interpretation of the data converted by the JESD interface and generated by the KIT-DMA interface can be seen in Fig. 5.19. The first two rows of the data called the **'HEADER'** are made of 256 bits, each consisting of a 16-bit start and end flag, the firmware version, default data acquisition settings, and the error status register. Next follows the **'PAYLOAD'** or the raw undecoded dataset of the preset size. A **'TAIL'** sequence flags the end of one data set. The PAYLOAD from the two ADCs alternates of 128 bits of data (1 row). A total of 64 rows comprises a single sample from 512 pixels. The data from the ADCs does not come in a sequential manner; their order is depicted in Fig. 5.19. The data decoder implemented in GUI follows the following algorithm,

- Find the **HEADER** flag from the data set. If found, slice the **HEADER** from the data set. If not, the data set has a consistency error and would require resetting the card.

- Search the **TAIL** from the back of the dataset and slice this section as well.

- Reorder the rest of the **PAYLOAD** from each ADC separately and then interleave them to form an ordered sample from pixel 0 to pixel 511.

(a) (b)
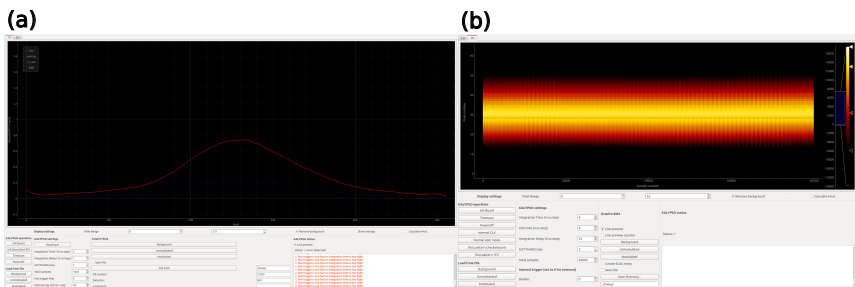
Figure 5.18: (a) The Graphical user interface for live viewing of the data acquisition in 1D format. (b) The graphical user interface for live viewing the data acquisition in 2D format.

- Rearrange the array in the form of microstrip n samples.

- Pass this on to the GUI for display, processing and storage.

```
0x00000000   0xf1111111        0x80000001        0x00000000        0x00000000              HEADER
0x00000010   0x00000000        0x00100010        0xf7777777        0xf8888888
0x00000020   0x34213421 (14,15) 0x34213421 (10,12) 0x34213421 (6,7) 0x34213421 (2,3)       ADC 0
0x00000030   0x00000000        0x00000000        0x00000000        0x00000000              ADC 1
0x00000040   0x34213421 (12,13) 0x34213421 (8,9)  0x34213421 (4,5) 0x34213421 (0,1)
0x00000050   0x00000000        0x00000000        0x00000000        0x00000000
0x00000060   0x34213421        0x34213421        0x34213421        0x34213421
0x00000070   0x00000000        0x00000000        0x00000000        0x00000000
0x00000080   0x34213421        0x34213421        0x34213421        0x34213421         1 row consists of 8 pixel
0x00000090   0x00000000        0x00000000        0x00000000        0x00000000           samples each of 16 bit
0x000000a0   0x34213421        0x34213421        0x34213421        0x34213421
0x000000b0   0x00000000        0x00000000        0x00000000        0x00000000
0x000000c0   0x34213421        0x34213421        0x34213421        0x34213421
0x000000d0   0x00000000        0x00000000        0x00000000        0x00000000         Data rows alternating
0x000000e0   0x34213421        0x34213421        0x34213421        0x34213421        between ADC 0 and ADC 1
0x000000f0   0x00000000        0x00000000        0x00000000        0x00000000
0x00000100   0x34213421        0x34213421        0x34213421        0x34213421
     *            *
     *            *
0x00000340   0x34213421        0x34213421        0x34213421        0x34213421
0x00000350   0x00000000        0x00000000        0x00000000        0x00000000
0x00000360   0x34213421        0x34213421        0x34213421        0x34213421
0x00000370   0x00000000        0x00000000        0x00000000        0x00000000
0x00000380   0x34213421        0x34213421        0x34213421        0x34213421
0x00000390   0x00000000        0x00000000        0x00000000        0x00000000
0x000003a0   0x34213421        0x34213421        0x34213421        0x34213421
0x000003b0   0x00000000        0x00000000        0x00000000        0x00000000
0x000003c0   0xfedcba98        0xfedcba98        0xfedcba98        0xfedcba98              TAIL
     *
0x00000400   0x00000000        0x00000000        0x00000000        0x00000000
     *
```

Figure 5.19: Raw data converted to digital by the ADC and transmitted by the JESD interface. Each alternating row contains the data of a single ADC. The numbers in blue indicate the corresponding microstrip number associated.

6 Experimental setup and results

The KALYPSO systems mentioned in chapter 5 and chapter 4 have been integrated into the experimental setups at KARA for longitudinal bunch size measurements (EOSD) and horizontal bunch size measurements (VLD). A KALYPSO system has also been commissioned for the first time at the SOLEIL light source in France for transverse beam diagnostics. The data presented in this chapter correspond to the measurements performed by the author.

6.1 Electro optical spectral decoding at KARA

The measurements were conducted during single short bunch operation mode at KARA with a beam energy of 1.3 GeV. The beam parameters at the time of the measurement are shown in the table 6.1.

Table 6.1: KARA beam parameters in short bunch mode used during the EOSD measurements.

Energy (E)	1.3 GeV
Beam current (I_b)	up to 3 mA
RF frequency (f_{RF})	499.744 MHz
Synchrotron frequency (f_s)	10.2 kHz
Momentum compaction factor (α_c)	6.5×10^{-4}
RF Voltage (V_{RF})	956 kV

The measurement procedure involves using a 35-meter-long fiber as a pulse stretcher. Chirped laser pulses produced by a self-built ytterbium-doped (Yb-doped) fiber laser (central wavelength around 1060 nm) are transported into the storage ring. The spectrum of this laser pulse at the oscillator's output measured by a commercial spectrometer[1] is shown in Fig. 6.1. The laser pulse is reflected at the back of the EO crystal which is moved inside the beam pipe close to the electron bunch. A transitory birefringence proportional to the electric field is induced as the electron bunch and laser pulse co-propagate (Pockels effect) [22]. Thus, by switching the polarization from linear to elliptical, the bunch profile is imprinted on the laser spectrum. The laser pulse is sent through polarization optics to encode the information, thus changes in polarization caused by the Pockels effect of the crystal are converted into intensity modulations of the spectral components, which can be decoded using a grating spectrometer.
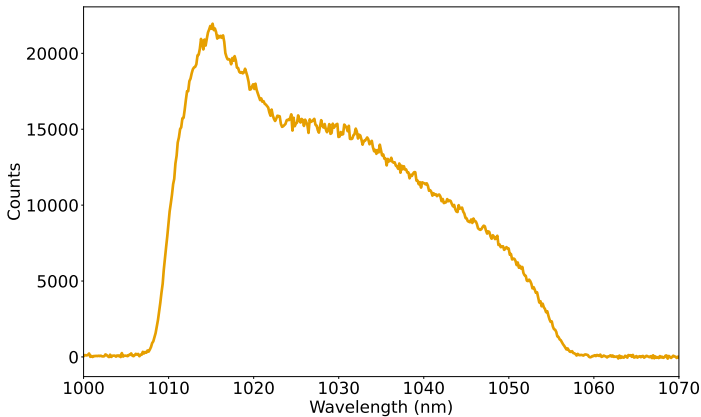
Figure 6.1: Spectrum of Yb-doped laser at the oscillator's output after mode-lock as measured by a commercial spectrometer.

An EOS (Electro-optic sampling) scan is performed to locate the phase of the laser at which the laser pulse and the Coulomb field of the electron bunch passing

---

[1]   Avantes AvaSpec-3648

by the GaP crystal are in sync, this is also called the temporal overlap. To find
the temporal overlap between the laser and the electron beam, a high-speed fibre-
coupled photodiode determines the temporal position of the laser peak intensity,
which is modulated by the Coulomb field of the electron bunch. An oscilloscope[2]
is used to obtain the maximum of the average signal from the photodiode[3] to
measure the EOS signal (average of 100 sweeps in Fig. 6.2).
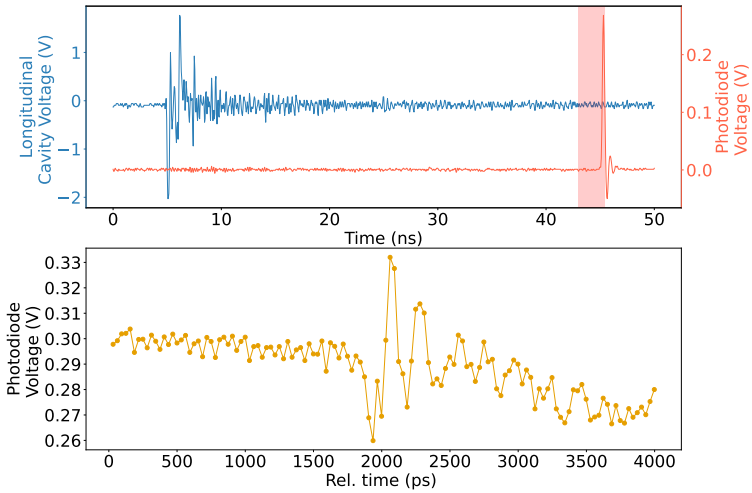
Figure 6.2: EOS scan measured using a photodiode. The upper plot corresponds to the time delay
measurement between the amplitude of the laser pulse back from the EO crystal and the longitudinal
cavity voltage by a BPM (Beam Position Monitor) located near the EO monitor. The shaded region
corresponds to the possible region of temporal overlap between the laser pulse and the electron bunch.
The bottom plot corresponds to sampling traces measured using a fast photodiode combined with
an oscilloscope and clearly shows the wakefield of the electron bunches. The x-axis corresponds to
the delay of the laser pulse in picoseconds, achieved by changing the delay of the laser pulse and the
y-axis to the maximum of the photodiode amplitude (red signal) detected with an oscilloscope (sample
average of 100 sweeps). Image and caption from [74].

The EOS signal depends on the relative delay between the laser pulse and the
electron bunch. The delay can be modified using a vector modulator (VM), which

---

2   LeCroy HDO9494-MS
3   ET-3010 from Electro-Optics Technology, Inc.

controls the timing of the laser pulse [23]. The region of interest for the delay is approximately defined by calculating the free space propagation delay between the BPM and the EO monitor and the delay introduced by the additional optical fiber and coaxial cables used for the measurement and has been currently estimated from previous measurements. A MATLAB script is used to acquire the data samples from the oscilloscope and as well access the EO control unit that controls both the oscilloscope and VM readings. The bottom of Fig. 6.2 shows one such measurement. This measurement measures the photodiode voltage's peak versus the laser pulse's system delay. This measurement gives an approximate delay of the laser pulse to measure the encoded Coulomb field. The relative modulation, as seen by the photodiode, depends on the bunch current and the distance between the crystal and the electron bunch. The modulation can be improved by a higher bunch current or by decreasing the distance to the electron bunch. Both have their inherent disadvantages, as they can result in damage to the EO crystal. The optimal settings for this have been investigated in the thesis of N. Hiller [23]. The temporal delay for the modulated (with Coulomb field) and unmodulated (without Coulomb field) signal is extracted from this plot which will be used later while acquiring EOSD data using KALYPSO.
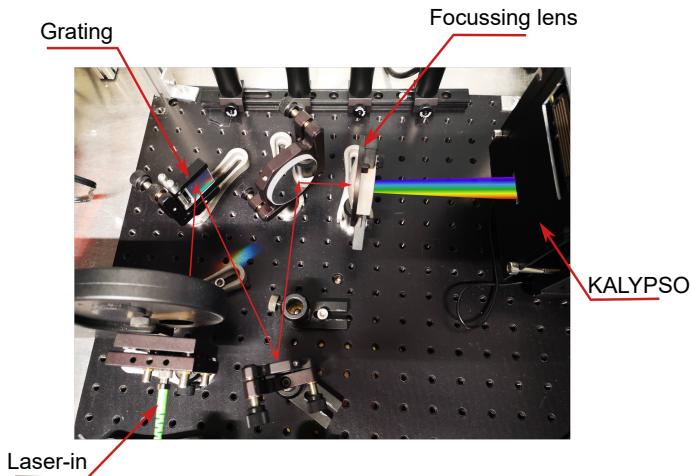
Figure 6.3: EO grating spectrometer setup with KALYPSO.

To measure the EOSD signal and thus the longitudinal bunch profile, the laser pulses are sent through a grating spectrometer and focused onto the Si-sensor (NIR coating) of KALYPSO using a lens, see Fig. 6.3. KALYPSO is operated at a frame rate equal to and synchronized with the revolution frequency of 2.7 MHz at KARA.
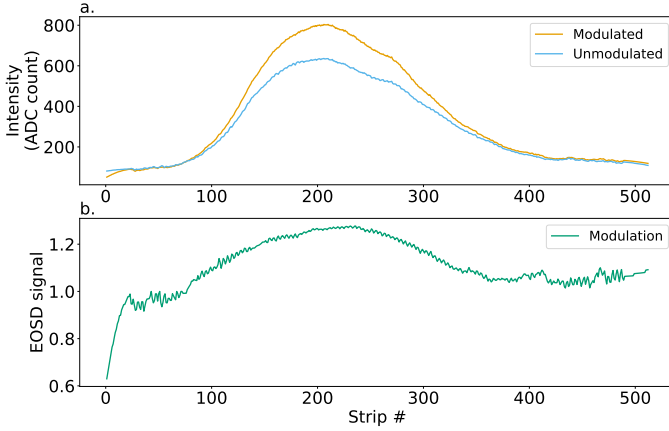
Figure 6.4: Measured EOSD signal by KALYPSO. (a) the yellow waveform corresponds to the laser pulse with modulation, and the blue waveform is without modulation. (b) corresponds to the EOSD signal given by the ratio of the above two waveforms. Image and caption from [74].

To measure the bunch profile on a linear array, a background signal is acquired by blocking any kind of light on the line array. Next the signal of a laser pulse propagating through the EO (GaP) crystal that does not contain the electron bunch profile information is recorded, i.e. the unmodulated signal. Then the laser pulse that overlaps with the electron bunch is recorded, i.e. the modulated signal. To perform these steps, the phase of the laser synchronization mechanism has been altered so that the laser pulse arrives at the EO crystal before the electron bunch does. Removing all the sensor background signals in both the modulated and the unmodulated samples is necessary to obtain the modulated and unmodulated signals. Figure 6.4 shows an example of such measurement.
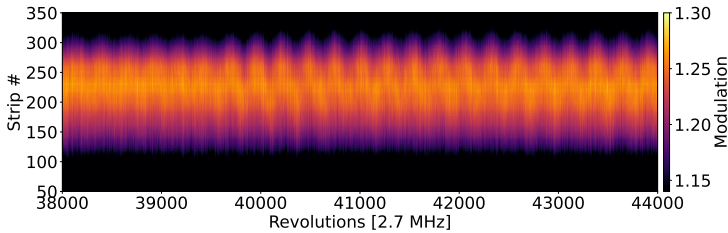
Figure 6.5: A section of 5,500 samples of the 100,000 continuously acquired bunch profiles spanning 36.8 ms. The x-axis corresponds to the revolution number with each revolution spanning 368 ns, and the y-axis corresponds to the EOSD signal calculated from Fig. 6.4. The z-axis (colour code) corresponds to the intensity of the EOSD signal. Image and caption from [74].

Figure 6.5 shows the evolution of the EOSD signal shown in 6.4 throughout a period of 2.2 ms. The oscillations visible correspond to the synchrotron frequency. Depending on the machine settings, these oscillations are usually in the kHz range. This oscillation is caused by the electron bunches oscillating in the longitudinal plane, which are present when the longitudinal feedback of the machine is turned off and can be calculated using eq. 1.39 in [75].

The improvement in the resolution of the new KALYPSO system compared to the previous KALYPSO versions mentioned in chapter 5 is yet to be determined. Due to the fluctuating laser power, which could have been caused by overheating of the EO crystal, and misaligned waveplates, it has not been easy to achieve better EOSD signals. However, investigations are being carried out, and the EO crystal is scheduled to be replaced soon. This might already improve the EOSD signal, and the detector can be further characterized for its performance.

6.2 Visible light diagnostic port at KARA

As described in chapter 2, measuring the horizontal bunch profile of the incoherent synchrotron radiation makes it possible to quantify the energy spread of short electron bunches. A dedicated optical setup located at the VLD port of KARA is shown in Fig. 6.6. An optical elevator transports the visible radiation to the optical table where a filter then transports the radiation with wavelengths 400 nm − 550 nm to the FGC or KALYPSO setup (red path)[4], and wavelengths > 550 nm to the streak camera (blue path). Cylindrical lenses with focal lengths of 200 mm and 100 mm are employed to focus the horizontal and vertical plane, respectively. Measurements shown in this section were performed with the machine parameters noted in Tab. 6.2.
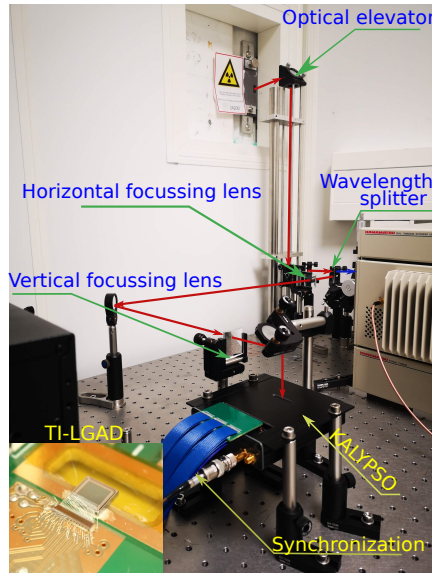
Figure 6.6: Optical setup for energy-spread measurement at the VLD port. In the inset is the mounted TI-LGAD sensor combined with the Gotthard ASIC. Image from [76].

---

4   The current setup does not allow for simultaneous measurements using FGC and KALYPSO.

Previously, a KALYPSO system based on a standard Si microstrip sensor was used to measure the horizontal bunch size [77]. Although the system improved compared to the FGC, its one drawback was its lack of sensitivity towards low bunch charges. The SNR of the system had been too low for such low bunch charge measurements. One solution to overcome this was for the front-end electronics (microstrip + ASIC) to have a higher SNR. This has been realized using the sensor based on LGAD with trench isolation (Refer to chapter 4 for simulations of standard LGAD structure and characterization of TI-LGAD). The initial measurements performed with this system have shown immense improvement regarding sensitivity (the input dynamic range of the system > 63.23 dB) and SNR. An example of the improvement can be seen in Fig. 6.7. The measurements shown depict the profile of the ISR as seen at the VLD port at KARA at the same bunch current of 1 mA (368 pC)[5]. The signal acquired by TI-LGAD-based KALYPSO is of the order of thirty times higher than that acquired by a conventional Si-based KALYPSO, thus enabling the measurement of radiation with very low intensity [78].

Table 6.2: KARA beam parameters in short bunch mode used during the energy spread measurements.

Energy (E)	1.3 GeV
Beam current (I_b)	0.1 to 3 mA
RF frequency (f_{RF})	499.744 MHz
Synchrotron frequency (f_s)	7.04 kHz
Momentum compaction factor (α_c)	3.4×10^{-4}
RF Voltage (V_{RF})	884.3 kV

Since KALYPSO enables continuous single-shot measurements, acquiring long data sets to study the bunch profile's evolution is possible. A data set is shown in Fig. 6.8. The first row of the figure shows the raw data of 80 000 revolutions covering a time range of 29 ms. The second row is a Gaussian fit performed on the raw data. The third and fourth rows are the horizontal bunch position and size

---

[5] To quantify the gain in the right way it is necessary to have the replica of the system without gain for the TI-LGAD. As this was not available at the time of the thesis, only a comparison with the previous system is shown.
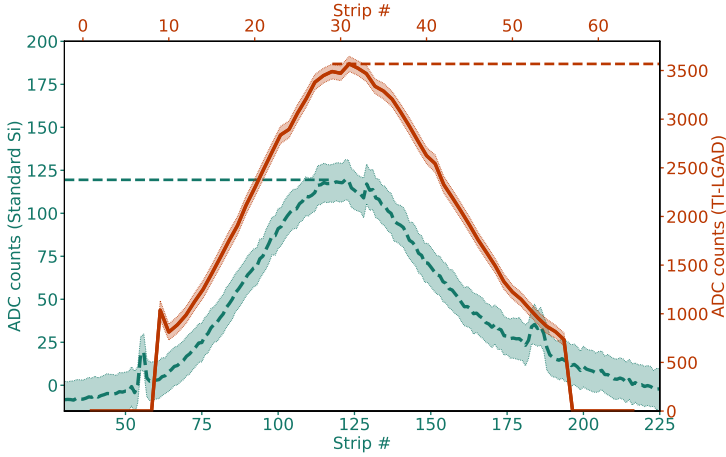
Figure 6.7: Comparison between the horizontal profiles measured using standard Si microstrip versus TI-LGAD based KALYPSO. The shaded region corresponds to the deviation margin [78].

extracted from the fit. This dataset shows the sawtooth evolution of bunch size correlated with THz bursting in low alpha operation mode. In the zoomed version of the highlighted window, see Fig. 6.9, it is possible to see the oscillation of the horizontal bunch position. The frequency of this oscillation corresponds to the synchrotron frequency and is due to the coherent motion of an electron bunch's center of mass.

An FFT (Fast Fourier Transform) can be performed on the horizontal bunch size to extract and analyze the underlying frequency components. Figure 6.10 depicts the FFT on the horizontal bunch size calculated from 80 000 revolutions. The main frequency components correspond to the synchrotron frequency at 7.05 kHz and its harmonics, and the low-frequency sawtooth bursting.

The calculated FFT for the bunch size can be measured for the decaying bunch current, and a so-called bursting spectrogram can be produced. These spectrograms have been previously generated for the CSR intensity measurements performed using KAPTURE [80, 79, 81] for different machine settings and have proven beneficial for analyzing the bursting dynamics. As explained in the introductory
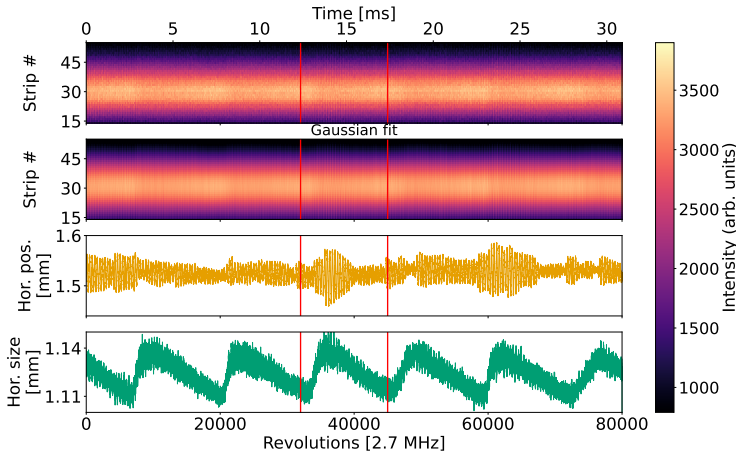
Figure 6.8: Incoherent synchrotron radiation measurement dataset acquired with KALYPSO-LGAD. The first row corresponds to the raw data for 80 000 revolutions acquired, the second row displays the Gaussian fit applied to the raw data, the third shows the horizontal position extracted from the fit and the fourth the horizontal bunch size extracted from the fit. Figure 6.9 gives the zoomed-in content between the red window [78].
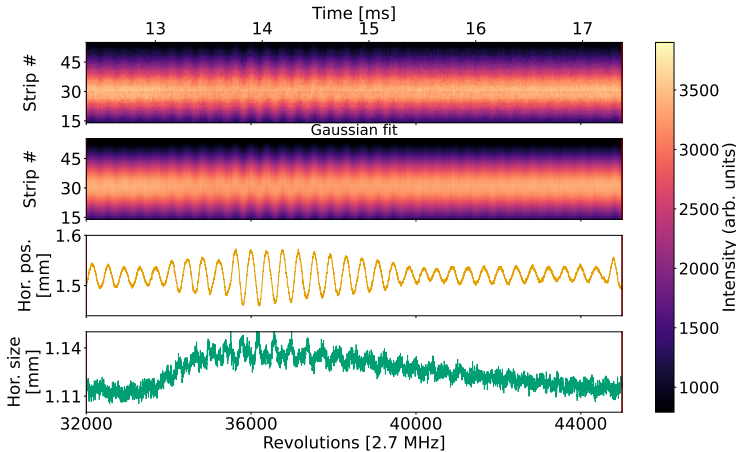
Figure 6.9: A zoomed-in representation of the highlighted window (between the two vertical red lines) in Fig. 6.8 showing the synchrotron oscillations with a frequency of 7.05 kHz [78].
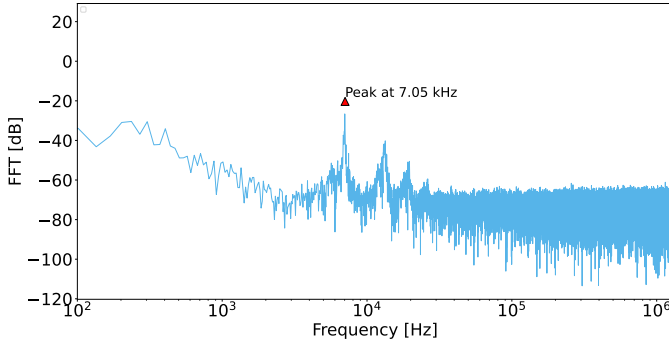
Figure 6.10: Fast Fourier Transform performed on the horizontal bunch size shown in 6.8. The peak at 7.05 kHz is highlighted, being the synchrotron frequency during the time of the measurement.
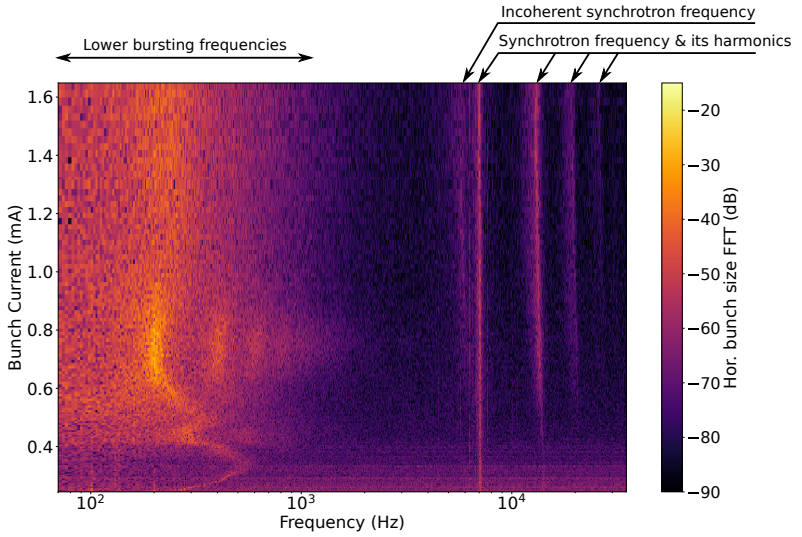
Figure 6.11: A spectrogram for horizontal bunch size with logarithmic frequency axis, to highlight both the low frequencies corresponding to the bursting dynamics and high frequencies corresponding to the synchrotron oscillations and its harmonics [78].

chapter 2 for beam diagnostics, the microbunching instability can be seen in the fluctuating CSR intensity. The fluctuating CSR intensity follows a sawtooth pattern, frequently referred to as *bursting pattern*. This *bursting pattern* changes

with the decaying bunch current over time. The bursting dynamics start to be visible at bunch currents lower than 1 mA and are prominent around the bursting threshold, which is around a bunch current of 0.2 mA at KARA.

Due to the improved sensitivity of KALYPSO, it is possible to measure these dynamics in correlation with the energy spread (horizontal bunch size) for the first time. Figure 6.11 shows one such analysed measurement. Spectrograms are fingerprints for a particular machine setting and can be reproduced under the same settings. Unlike the spectrograms generated from CSR intensity [80, 79, 81], the finger frequency [80], used to determine the bursting threshold [82] and which is higher than the synchrotron frequency, is not visible in the spectrogram generated for the horizontal bunch size. This is also correlated to the fact that it has not been possible to observe microstructures formed due to microbunching instability in the horizontal bunch size. What, however, are visible are the lower bursting frequencies. These frequencies follow a pattern similar to what was observed for the CSR intensity spectrogram. The lower bursting frequency here appears to increase and decrease over a range of bunch currents and, just like the CSR intensity spectrogram, seems to disappear slightly at higher bunch currents. Also, a characteristic visible is the constant synchrotron frequency which does not fluctuate over the bunch current. The frequency component corresponding to the incoherent synchrotron radiation, corresponding to the incoherent motion of single electrons is below the coherent synchrotron frequency. The incoherent synchrotron frequency deviates towards lower frequency values with the increasing bunch current, also visible in Fig. 6.11. This has been explained in detail in [35].

The overall performance of KALYPSO-LGAD concerning its sensitivity and dynamic range has been tested with a calibrated light source (in chapter 4) and in actual beam conditions. As seen in Fig. 6.12, it has proven that the system is capable of resolving the bunch profile of the incoherent synchrotron radiation even at very low bunch charges down to 0.05 mA. The experiment proved that LGAD is a positive addition as a detector for photon sciences. The current prototype will be upgraded to a broader TI-LGAD sensor in the following engineering run to improve the spatial resolution as the current sensor is a prototype of size 3000 x 3000 m
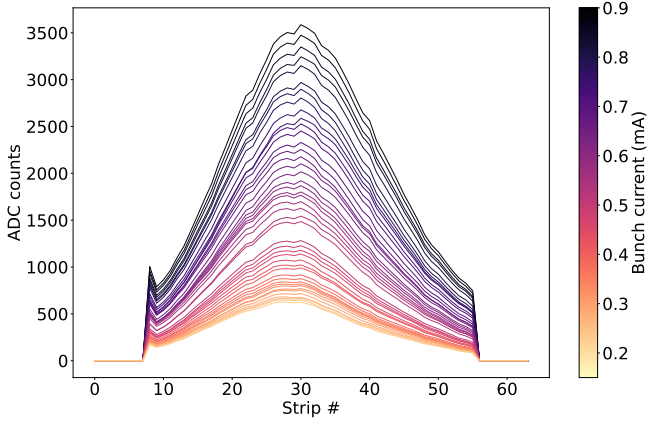
Figure 6.12: Horizontal bunch profiles measured during bunch current decay. This shows that KALYPSO-LGAD can resolve the bunch profiles even at low bunch currents.

At KARA, it is possible to implement both low-alpha as well as negative-alpha modes. This mode of operation has been implemented in the thesis P. Schreiber [81]. In brief, the negative values for α_c given by equation 2.2 have been investigated [83]. This method has allowed for bunch lengths lower than what could be achieved by positive low α_c, which could, in turn, result in stronger CSR emission [84]. According to the present status, a single bunch with a bunch current of 0.3 mA can be stored in the storage ring. Using conventional Si-based KALYPSO has been challenging due to the detector's low sensitivity and noise performance at such low bunch currents. Hence, once KALYPSO-LGAD was ready, the first energy spread measurements were performed at the VLD port of KARA at negative alpha mode. The first measurement results are shown in Fig. 6.13 and 6.14. The bursting regime can be seen in the extracted horizontal bunch size. Since this is the first measurement, the energy spread has to be studied in detail which is beyond the scope of this thesis. Nevertheless, the first measurement results have been shown here.
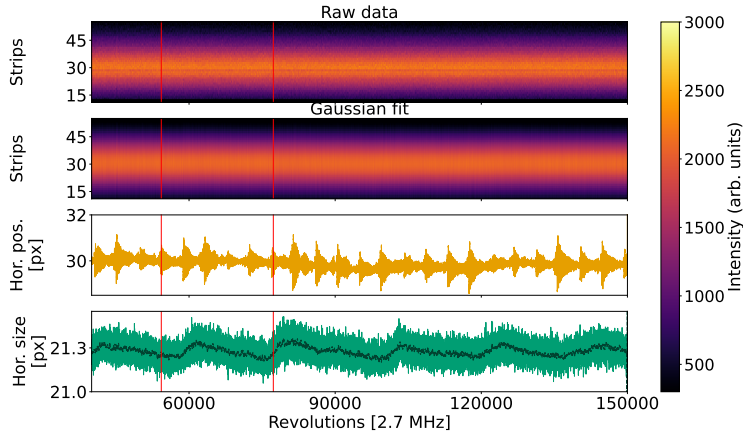
Figure 6.13: The first horizontal bunch size measurements acquired by KALYPSO-LGAD for negative α_c. The red window is expanded in Fig. 6.14.
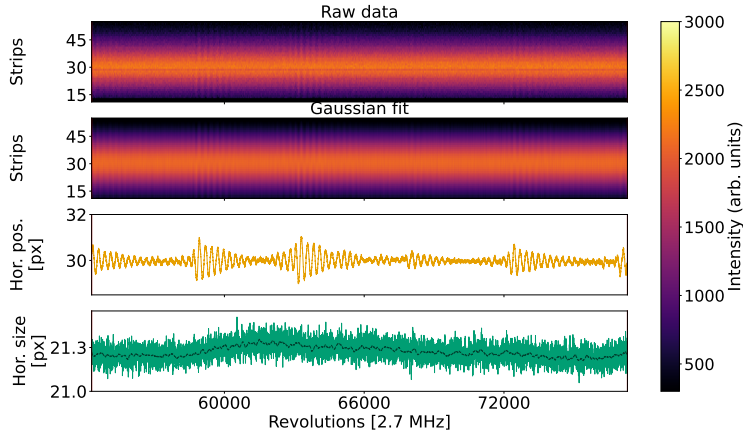
Figure 6.14: Zoomed in perspective of the data shown in Fig. 6.13, showing the oscillations corresponding to the synchronous motion of the electron bunches.

6.3 Transverse beam diagnostics at Soleil

SOLEIL (Source optimisée de lumière d'énergie intermédiaire du LURE) is a synchrotron light source facility located near Paris, France. At SOLEIL, a new beamline for measuring synchrotron radiation has been implemented. The optical setup splits the incoming SR into vertically and horizontally polarized light.

The horizontal and vertical component is measured using KALYPSO [85]. The KALYPSO detector used is a 1024 microstrip version with AR coating for visible light developed by the author during this thesis. The turn-by-turn measurements have been performed at 846 kHz. The initial remote commissioning was performed in 2021 by IPE and has been since then used to study the effect of injection for maintaining a constant bunch charge by the machine group at SOLEIL. The position displacement in the horizontal and vertical plane due to the kickers used for injection can be seen in Fig. 6.15. The installed system now allows for shot-to-shot measurements at SOLEIL, which was previously not possible with a commercial camera.
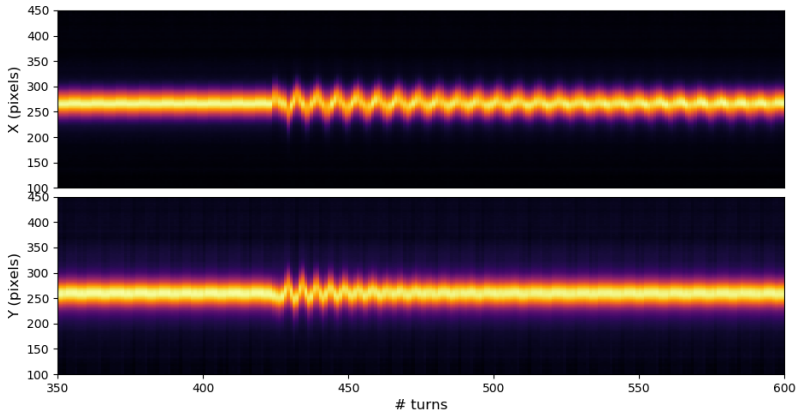
Figure 6.15: Kalypso raw datasets recorded at MRSV (Moniteur de Rayonnement Synchrotron Visible) beamline in SOLEIL. Recording launched a few hundred revolutions before injection time. Imaging of (top) the horizontal and (bottom) the vertical distribution of the beam. Image and caption taken from [85].

7   Conclusion

With the recent technological advances, accelerator and synchrotron light sources worldwide are capable of emitting radiation with high brilliance with tunability. The radiation can be used in many applications ranging from biological sample analysis, medical imaging and treatment to material sciences, etc. Modern detectors are hence crucial for beam diagnostics in synchrotron light sources, to optimize the radiation emitted and for it to be more stable with high brilliance. A detector's characteristics must match the requirements to keep up with the high repetition rate of synchrotron light sources. These requirements include *high acquisition rates (*MHz*), good spatial resolution (<*25 m*), wide dynamic range (>*60 dB*), broad spectral sensitivity (350 to* 5000 nm*), low noise (SNR > 60 dB*), and good time resolution (picoseconds)*.

KALYPSO is one such detector capable of fulfilling all the above requirements. The first version of KALYPSO was capable of frame rates of 2.7 MHz. It had a total of 256 channels with pitch 50 m and was incorporated with a microstrip sensor based on Si (designed at Paul Scherrer Institute (PSI)), and InGaAs (from Xenics). With these specifications, KALYPSO has already been the fastest line camera.

As part of this thesis, the author has worked on the following topics:

- To improve the spatial resolution and spectral sensitivity of KALYPSO, a custom Si microstrip sensor has been designed during the Master thesis [70] and fabricated during the Doctoral thesis. The sensor was optimized for the requirements requested by several accelerator facilities, including KARA, DESY, SOLEIL etc. The customized sensor has several geometries suited for specific applications and features from 512 to up to 1024 channels

with pitch 25 m. It has an optimized ARC based on Si_xN_y for improving the quantum efficiency (up to 90%) in the NUV (350-450 nm), visible (450-850 nm) and NIR (850-1050 nm) range. A KALYPSO system based on this microstrip sensor has been tested at the EOSD setup at KARA (NIR based) for longitudinal bunch size measurements, at the VLD port of KARA (visible) for energy spread measurements, and at SOLEIL (visible) for transverse bunch size measurements.

- To extend the spectral sensitivity of KALYPSO to an even longer wavelength, commercial microstrip sensors based on InGaAs (950-2000 nm), PbS (1200-3000 nm), PbSe (1200-5000 nm) have been utilized. The systems based on these sensors have been assembled and tested with a laser source at 1560 nm. A spectrometer set up to investigate the laser spectrum has been installed. A broadband light source with spectral emission up to 5 m is foreseen to be used in the future for characterizing the different microstrip sensors [69, 77, 76, 74].

- To understand the performance of the LGAD-based microstrip sensors TCAD simulations of LGAD sensors have been performed and studied to understand the charge collection behaviour. Structures have been simulated with different gain implant depths and concentrations. The electric field distribution, charge collection, and gain of these structures have been studied by simulation and are found to agree with the theoretical concept of the design. The simulations allow for finalising the design parameters required for an engineering run.

- To study the behaviour and performance for photon science applications, TI-LGAD sensors fabricated as a part of the RD50 collaboration[1] have been tested and characterized extensively. Several design structures and models were tested. The I-V characteristics of the sensors were measured, and they agree with the independent testing performed at FBK. Additionally, PTC measurements were performed to study the sensitivity and dynamic

---

[1] https://rd50.web.cern.ch/

range of the sensors. The results from the characterization have led to the conclusion that the sensors have better noise performance and dynamic range compared to conventional PDs.

- Measuring low-intensity radiation with standard Si microstrip sensors is challenging due to the inherent noise contribution. Although KALYPSO with standard silicon microstrip has been able to measure the incoherent synchrotron radiation at the VLD port, low bunch current measurements around the bursting threshold of the micro-bunching instability have not been possible. Hence, to improve the SNR, a KALYPSO system equipped with a TI-LGAD was assembled. The TI-LGAD sensor was read out by a custom-made ASIC Gotthard, capable of working up to 12 MHz. The KALYPSO-LGAD has now been produced, tested, characterized, and integrated into the VLD port at KARA for energy spread studies. It has been used as a proof of concept experiment for using LGAD sensors for visible light diagnostics and not only for high energy physics. The measurements now allow users to measure incoherent synchrotron radiation for bunch currents down to 0.05 mA (20 pC). Due to the significant improvement in the detector's sensitivity, an engineering run is planned with TI-LGAD with a wider active region and better spatial resolution. Another interesting improvement of the system is the 12 MHz repetition rate. This is useful for studying beam dynamics in a single bunch and a multi-bunch environment. Initial tests for multi-bunch studies are ongoing and will be tested at the VLD port in the following months.

- To improve the sensitivity to NIR sources, a KALYPSO version with 512 microstrips with a pitch of 25 m, with an ARC coating to improve the absorption efficiency towards NIR radiation has been commissioned at the EOSD experiment at KARA. The first measurements with the systems have been reported. A more detailed study is ongoing.

In brief, the KALYPSO detector has been upgraded or rather branched to various versions. The systems developed have improved spatial and timing resolutions. The throughput of the system is higher than the previous detectors, i.e., from

$5\,\mathrm{GB\,s^{-1}}$ to $21\,\mathrm{GB\,s^{-1}}$. KALYPSO-LGAD has been the major improvement with its capability to measure bunch charges as low as 20 pC.

Several upgrades are ongoing to improve the system further. A few are listed below,

- A dedicated engineering run to fabricate TI-LGADs with a larger area is planned in the ongoing year. The current system has only 48 microstrips, making optimising the optical setup tricky.

- Design of an LGAD sensor with a thickness of a few hundred microns is also in preparation. This is to overcome the disadvantages posed by the current LGAD version, which is only 45 m in thickness. This makes the sensor less sensitive to NIR sources, especially those used for EOSD.

- The next version of KALYPSO will employ the GOTTHARD-KIT ASIC in combination with a wide range of sensors. This version is currently in the firmware testing phase.

- And finally KALYPSO based on InGaAs is planned to be installed for measuring the CSR spectrum at the Far-field EOSD setup currently under commission.

List of Figures

List of Tables

Abbreviations

AC	Alternating Current
ADC	Analog to Digital Converter
APD	Avalanche Photodiode
ARC	Anti-reflection Coating
ASIC	Application Specific Integrated Circuit
BB	Broadband
CCE	Charge Collection Efficiency
CDS	Correlated Double Sampling
CML	Common Mode Logic
CMOS	Complementary metal–oxide–semiconductor
CPU	Central Processing Unit
CSA	Charge Sensitive Amplifier
CSR	Coherent Synchrotron Radiation
DAQ	Data Acquisition
DC	Direct Current
DDR	Double Data Rate

DESY	Deutsches Elektronen-Synchrotron
DMA	Direct Memory Access
EMI	Electro-magnetic Interference
EO	Electro Optical
EOSD	Electro Optic Spectral Decoding
ESD	Electro Static Discharge
FBK	Fondazione Bruno Kessler
FBSF	Filament Beam Spread Function
FEM	Finite Element Method
FGC	Fast Gated Camera
FIFO	First in First out
FMC	FPGA Mezzanine Card
FOV	Field of view
FPGA	Field-programmable gate array
FPN	Fixed Pattern Noise
FSM	Finite State Machine
FT	Fast Trigger
GTH	Gigabit transceivers
GPU	Graphical Processing Unit
GUI	Graphical User Interface

I2C	Inter-Integrated Circuit
INFN	Istituto Nazionale di Fisica Nucleare
InP	Indium Phosphide
IPE	Institute for data processing
IR	Infrared
KALYPSO	KArlsruhe Linear arraY detector for MHz rePetition-rate SpectrOscopy
KAPTURE	Karlsruhe Pulse Taking Ultra-Fast Readout Electronics
KARA	Karlsruhe Research Accelerator
KIT	Karlsruher Institut für Technologie
LED	Light Emitting Diode
LGAD	Low Gain Avalanche Detectors
LVDS	Low-voltage differential signaling
LWIR	Long-wave Infrared
MIP	Minimum Ionising Particle
MIM	Metal Insulator Metal
MMCM	Mixed-Mode Clock Manager
MWIR	Mid-wavelength Infrared
OAP	Off Axis Paraboloid
PCB	Printed Circuit Board
PD	Photodiode

PSD   Phase Space Distribution

PSF   Point Spread Function

PTC   Photon Transfer Curve

QE   Quantum Efficiency

RFI   Radio Frequency Interference

RMS   Root mean square

SNR   Signal-to-Noise Ratio

SOLEIL   Source optimisée de lumière d'énergie intermédiaire du LURE

SPC   Single Photon Counter

SPI   Serial Peripheral Interface

TCAD   Technology Computer-Aided Design

TCT   Transient Current Technique

TCSPC   Time-correlated Single Photon Counter

VIS   Visible

VLD   Visible Light Diagnostics

VM   Vector Modulator

UMC   United Microelectronics Corporation

Bibliography

Main references

[1] F. R. Elder, A. M. Gurewitsch, R. V. Langmuir, *et al.*, "Radiation from Electrons in a Synchrotron", *Physical Review*, vol. 71, no. 11, pp. 829–830, Jun. 1947. [Online]. Available: http://dx.doi.org/10.1103/physrev.71.829.5.

[2] J. S. Nodvick and D. S. Saxon, "Suppression of Coherent Radiation by Electrons in a Synchrotron", *Physical Review*, vol. 96, no. 1, pp. 180–184, Oct. 1954. [Online]. Available: http://dx.doi.org/10.1103/physrev.96.180.

[3] G. Stupakov and S. Heifets, "Beam instability and microbunching due to coherent synchrotron radiation", *Physical Review Special Topics - Accelerators and Beams*, vol. 5, no. 5, May 2002. [Online]. Available: http://dx.doi.org/10.1103/physrevstab.5.054402.

[4] M. Venturini and R. Warnock, "Bursts of Coherent Synchrotron Radiation in Electron Storage Rings: A Dynamical Model", *Physical Review Letters*, vol. 89, no. 22, Nov. 2002. [Online]. Available: http://dx.doi.org/10.1103/physrevlett.89.224802.

[5] J. M. Byrd, W. P. Leemans, A. Loftsdottir, *et al.*, "Observation of Broadband Self-Amplified Spontaneous Coherent Terahertz Synchrotron Radiation in a Storage Ring", *Physical Review Letters*, vol. 89, no. 22, Nov. 2002. [Online]. Available: http://dx.doi.org/10.1103/physrevlett.89.224801.

[6]   G. Carr, S. Kramer, J. Murphy, *et al.*, "Observation of coherent synchrotron radiation from the NSLS VUV ring", *Nuclear Instruments and Methods in Physics Research Section A: Accelerators, Spectrometers, Detectors and Associated Equipment*, vol. 463, no. 1-2, pp. 387–392, May 2001. [Online]. Available: http://dx.doi.org/10.1016/s0168-9002(01)00521-6.

[7]   C. Evain, J. Barros, A. Loulergue, *et al.*, "Spatio-temporal dynamics of relativistic electron bunches during the micro-bunching instability in storage rings", *EPL (Europhysics Letters)*, vol. 98, no. 4, p. 40 006, May 2012. [Online]. Available: http://dx.doi.org/10.1209/0295-5075/98/40006.

[8]   W. Shields, R. Bartolini, G. Boorman, *et al.*, "Microbunch Instability Observations from a THz Detector at Diamond Light Source", *Journal of Physics: Conference Series*, vol. 357, p. 012 037, May 2012. [Online]. Available: http://dx.doi.org/10.1088/1742-6596/357/1/012037.

[9]   C. A. Thomas, J. I. Botman, C. Bruni, *et al.*, "Storage ring free electron laser dynamics in presence of an auxiliary harmonic radio frequency cavity", *The European Physical Journal D*, vol. 32, no. 1, pp. 83–93, Jan. 2005. [Online]. Available: http://dx.doi.org/10.1140/epjd/e2004-00200-6.

[10] P. Schütze, A. Borysenko, E. Hertle, *et al.*, "A fast gated intensified camera setup for transversal beam diagnostics at the anka storage ring", *Proc. IPAC'15*, pp. 872–875, 2015. [Online]. Available: https://accelconf.web.cern.ch/ipac2015/papers/mopha039.pdf.

[11] M. Brosi, E. Blomley, E. Bründermann, *et al.*, "Systematic studies of short bunch-length bursting at ANKA", *IPAC : proceedings of the 7th International Particle Accelerator Conference : Busan, Korea, May 8-13, 2016. Ed.: W. Namkung*, pp. 1662–1665, Jun. 2016. DOI: 10.18429/jacow-ipac2016-tupor006.

[12] B. Kehrer, M. Brosi, J. L. Steinmann, *et al.*, "Synchronous detection of longitudinal and transverse bunch signals at a storage ring", *Physical Review Accelerators and Beams*, vol. 21, no. 10, Oct. 2018. [Online]. Available: http://dx.doi.org/10.1103/physrevaccelbeams.21.102803.

[13] A. Svetlitza, M. Slavenko, T. Blank, *et al.*, "THz Measurements and Calibration Based on a Blackbody Source", *IEEE Transactions on Terahertz Science and Technology*, vol. 4, no. 3, pp. 347–359, 2014. DOI: 10.1109/tthz.2014.2309003.

[14] A. S. Müller, N. Hiller, A. Hofmann, *et al.*, "Experimental aspects of csr in the anka storage ring", *ICFA Beam Dynamics Newsletter*, vol. 57, no. 57, pp. 154–164, 2012, 55.98.30; LK 02.

[15] E. Bründermann, H.-W. Hübers, and M. Kimmitt, *Terahertz Techniques*. Springer Nature, Jan. 2012. [Online]. Available: https://doi.org/10.1007/978-3-642-02592-1.

[16] A.-S. Müller, "Accelerator-Based Sources of Infrared and Terahertz Radiation", *Reviews of Accelerator Science and Technology*, vol. 03, no. 01, pp. 165–183, 2010. DOI: 10.1142/s1793626810000427.

[17] N. Hiller, "Determination of the Synchrotron Radiation Pulse Length at the ANKA Storage Ring - Bestimmung der Synchrotronstrahlungspulslänge am ANKA-Speicherring", Jan. 2009. [Online]. Available: https://publikationen.bibliothek.kit.edu/1000022016.

[18] H. Wiedemann, *Particle accelerator physics*. Springer Nature, 2015. [Online]. Available: http://library.oapen.org/handle/20.500.12657/23641.

[19] P. Schönfeldt, M. Brosi, M. Schwarz, *et al.*, "Parallelized Vlasov-Fokker-Planck solver for desktop personal computers", *Physical Review Accelerators and Beams*, vol. 20, no. 3, Mar. 2017. [Online]. Available: http://dx.doi.org/10.1103/physrevaccelbeams.20.030704.

[20] G. Kassier, K. Haupt, N. Erasmus, *et al.*, "A compact streak camera for 150 fs time resolved measurement of bright pulses in ultrafast electron diffraction", *Review of Scientific Instruments*, vol. 81, no. 10, p. 105103, 2010. DOI: 10.1063/1.3489118.

143

[21] N. Hiller, A. Hofmann, E. Huttel, *et al.*, "Status of bunch deformation and lengthening studies at the anka storage ring", *IPAC 2011 - 2nd International Particle Accelerator Conference*, pp. 2951–2953, 2011. [Online]. Available: https://www.scopus.com/inward/record.uri?eid=2-s2.0-84885781662&partnerID=40&md5=277d91b374286a9ef13dfa861aff6072.

[22] I. Wilke, A. MacLeod, W. Gillespie, *et al.*, "Single-Shot Electron-Beam Bunch Length Measurements", *Physical Review Letters*, vol. 88, no. 12, 2002. DOI: 10.1103/physrevlett.88.124801.

[23] N. Hiller, "Electro-optical bunch length measurements at the anka storage ring", PhD thesis, 2013. DOI: 10.5445/IR/1000041159.

[24] B. Steffen, S. Casalbuoni, E.-A. Knabbe, *et al.*, "Spectral decoding electro-optic measurements for longitudinal bunch diagnostics at the desy vuv-fel", Jan. 2005. [Online]. Available: https://accelconf.web.cern.ch/f05/papers/thpp039.pdf.

[25] B. E. A. Saleh, M. C. Teich, and R. E. Slusher, *Fundamentals of Photonics*. Apr. 2016, pp. 3–34. [Online]. Available: https://doi.org/10.1201/b13065-1.

[26] G. Niehues, E. Bründermann, M. Caselle, *et al.*, "Electro-optical diagnostics at kara and flute – results and prospects", in *12th International Particle Accelerator Conference : virtual edition, May 24th-28th, 2021, Brazil : proceedings volume / IPAC2021. Ed.: R. Picoreti*, (Online, May 24–28, 2021), 54.11.11; LK 01, JACoW Publishing, 2021, pp. 927–930, ISBN: 978-3-95450-214-1. DOI: 10.18429/JACoW-IPAC2021-MOPAB293.

[27] F. Müller, S. Hunziker, V. Schlott, *et al.*, "Ytterbium fiber laser for electro-optical pulse length measurements at the swissfel", in *Proceedings DIPAC*, vol. 9, 2009. [Online]. Available: https://accelconf.web.cern.ch/d09/papers/tupd31.pdf.

[28] B. R. Steffen and DESY, "Electro-Optic Methods for Longitudinal Bunch Diagnostics at FLASH.", Univ. Hamburg, Diss., 2007, PhD thesis, Univ.

Hamburg, Hamburg, 2007. [Online]. Available: https://bib-pubdb1.desy.de/record/84041.

[29] E. Collett, *Field Guide to Polarization*. Sep. 2005. [Online]. Available: https://doi.org/10.1117/3.626141.

[30] L. Rota, M. Balzer, M. Caselle, *et al.*, "Kalypso: A mfps linear array detector for visible to nir radiation", *Proceedings of the 5th International Beam Instrumentation Conference, IBIC 2016*, pp. 740–743, 2016. [Online]. Available: https://www.scopus.com/inward/record.uri?eid=2-s2.0-85072036177&partnerID=40&md5=b1a37f70148cd84fb25f2686c80d1bec.

[31] L. Rota, "Kalypso, a novel detector system for high-repetition rate and real-time beam diagnostics", 54.02.02; LK 01, PhD thesis, Karlsruher Institut für Technologie (KIT), 2018, 166 pp. DOI: 10.5445/IR/1000082349.

[32] S. Funkner, E. Blomley, E. Bründermann, *et al.*, "High throughput data streaming of individual longitudinal electron bunch profiles", *Physical Review Accelerators and Beams*, vol. 22, no. 2, Feb. 2019. [Online]. Available: http://dx.doi.org/10.1103/physrevaccelbeams.22.022801.

[33] S. Funkner, G. Niehues, M. J. Nasse, *et al.*, "Revealing the dynamics of ultrarelativistic non-equilibrium many-electron systems with phase space tomography", *Scientific Reports*, vol. 13, no. 1, Dec. 2019. [Online]. Available: https://doi.org/10.1038/s41598-023-31196-5.

[34] M. Brosi, M. Caselle, E. Hertle, *et al.*, "Online Studies of THz-radiation in the Bursting Regime at ANKA", pp. 882–884, Jun. 2015. [Online]. Available: http://jacow.org/ipac2015/papers/mopha042.pdf.

[35] B. Kehrer, "Time-resolved studies of the micro-bunching instability at kara", 54.01.01; LK 01, PhD thesis, Karlsruher Institut für Technologie (KIT), 2019, 143 pp. DOI: 10.5445/IR/1000098584.

[36] W. Becker, *Advanced Time-Correlated Single Photon Counting Applications*. Springer Science+Business Media, Jan. 2015. [Online]. Available: https://doi.org/10.1007/978-3-319-14929-5.

[37] B. Kehrer, A. Borysenko, E. Hertle, *et al.*, "Visible light diagnostics at the anka storage ring", *6th International Particle Accelerator Conference, IPAC 2015*, pp. 866–868, 2015. [Online]. Available: https://www.scopus.com/inward/record.uri?eid=2-s2.0-84994663307&partnerID=40&md5=495ccb6d264630f3d4a4ea81f2d03ec2.

[38] Å. E. Andersson, V. Schlott, M. Rohrer, *et al.*, "ELECTRON BEAM PROFILE MEASUREMENTS WITH VISIBLE AND X- RAY SYN-CHROTRON RADIATION AT THE SWISS LIGHT SOURCE", Jan. 2006. [Online]. Available: http://epaper.kek.jp/e06/papers/tupch090.pdf.

[39] G. Lutz, *Semiconductor Radiation Detectors*. Springer, Jun. 2007. [Online]. Available: https://doi.org/10.1007/978-3-540-71679-2.

[40] R. F. Pierret, *Semiconductor device fundamentals*. Jan. 1996. [Online]. Available: http://ci.nii.ac.jp/ncid/BA29598058.

[41] A. Khan, *Introduction to Electrical , Electronics and Communication Engineering*. Firewall Media, Dec. 2005, ISBN: ISBN 978-81-7008-639-0.

[42] G. F. Knoll, *Radiation Detection and Measurement*. Mar. 2013, pp. 489–522. [Online]. Available: https://doi.org/10.1002/9783527667062.ch12.

[43] A. H. Compton, "A quantum theory of the scattering of x-rays by light elements", *Phys. Rev.*, vol. 21, pp. 483–502, 5 1923. [Online]. Available: https://link.aps.org/doi/10.1103/PhysRev.21.483.

[44] M. F. L'Annunziata, "3 - gamma- and x-radiation — photons", in *Radioactivity*, Amsterdam: Elsevier Science B.V., 2007, pp. 187–215, ISBN: 978-0-444-52715-8. [Online]. Available: https://www.sciencedirect.com/science/article/pii/B9780444527158500062.

[45] A. Rogalski, "Infrared Detectors", *CRC Press eBooks*, Nov. 2010. DOI: 10.1201/b10319.

[46] R. Turchetta, "Spatial resolution of silicon microstrip detectors", *Nuclear Instruments and Methods in Physics Research*, vol. 335, no. 1-2, pp. 44–58, Oct. 1993. [Online]. Available: https://doi.org/10.1016/0168-9002(93)90255-g.

[47] F. Hartmann, *Evolution of Silicon Sensor Technology in Particle Physics*. Springer Science+Business Media, Jan. 2017. [Online]. Available: https://doi.org/10.1007/978-3-319-64436-3.

[48] M. Krammer *et al.*, "Silicon detectors", *Institute of High Energy Physics, Vienna, Austria*, 2011. [Online]. Available: https://indico.cern.ch/event/124392/contributions/1339904/attachments/74582/106976/IntroSilicon.pdf.

[49] W. R. Leo, *Techniques for Nuclear and Particle Physics Experiments: A How-To Approach*. Nov. 1987. [Online]. Available: https://cds.cern.ch/record/302344/files/0387572805_TOC.pdf.

[50] M. Baselga Bacardit, T. Bergauer, A. H. Dierlamm, *et al.*, "Front-side biasing of n-in-p silicon strip detectors", CERN, Geneva, Tech. Rep., 2018. [Online]. Available: https://cds.cern.ch/record/2316596.

[51] I. Cortés, P. Fernńdez-Martínez, D. Flores, *et al.*, "Gain estimation of rt-apd devices by means of tcad numerical simulations", in *Proceedings of the 8th Spanish Conference on Electron Devices, CDE'2011*, 2011, pp. 1–4. DOI: 10.1109/SCED.2011.5744152.

[52] M. Ferrero, R. Arcidiacono, M. Mandurrino, *et al.*, *An Introduction to Ultra-Fast Silicon Detectors (Series in Sensors)*, 1st ed. CRC Press, 2021.

[53] R. Van Overstraeten and H. De Man, "Measurement of the ionization rates in diffused silicon pn junctions", *Solid State Electronics*, vol. 13, no. 5, pp. 583–608, 1970. DOI: 10.1016/0038-1101(70)90139-5.

[54] D. Massey, J. P. R. David, and G. Rees, "Temperature Dependence of Impact Ionization in Submicrometer Silicon Devices", *IEEE Transactions on Electron Devices*, vol. 53, no. 9, pp. 2328–2334, Aug. 2006. [Online]. Available: https://doi.org/10.1109/ted.2006.881010.

[55] M. Valdinoci, D. Ventura, M. Vecchi, *et al.*, "Impact-ionization in silicon at large operating temperature", in *1999 International Conference on Simulation of Semiconductor Processes and Devices. SISPAD'99 (IEEE Cat. No.99TH8387)*, 1999, pp. 27–30. DOI: 10.1109/SISPAD.1999.799251.

[56] Y. Okuto and C. R. Crowell, "Ionization coefficients in semiconductors: A nonlocalized property", *Phys. Rev. B*, vol. 10, pp. 4284–4296, 10 1974. [Online]. Available: https://link.aps.org/doi/10.1103/PhysRevB.10.4284.

[57] W. Shockley, "Currents to conductors induced by a moving point charge", *Journal of Applied Physics*, vol. 9, no. 10, pp. 635–636, 1938. [Online]. Available: https://doi.org/10.1063/1.1710367.

[58] S. Ramo, "Currents induced by electron motion", *Proceedings of the IRE*, vol. 27, no. 9, pp. 584–585, 1939. DOI: 10.1109/JRPROC.1939.228757.

[59] N. Cartiglia, "Signal formation and timing with LGAD sensors", Jun. 2016. [Online]. Available: https://indico.cern.ch/event/468478/contributions/2135146/attachments/1290321/1921375/LGA_Signal_Cartiglia.pdf.

[60] M. F. Snoeij, A. J. P. Theuwissen, K. A. A. Makinwa, *et al.*, "A CMOS Imager With Column-Level ADC Using Dynamic Column Fixed-Pattern Noise Reduction", *IEEE Journal of Solid-State Circuits*, vol. 41, no. 12, pp. 3007–3015, Dec. 2006. [Online]. Available: http://dx.doi.org/10.1109/jssc.2006.884866.

[61] G. Giacomini, "Fabrication of Silicon Sensors Based on Low-Gain Avalanche Diodes", *Frontiers in Physics*, vol. 9, Apr. 2021. [Online]. Available: https://www.frontiersin.org/articles/10.3389/fphy.2021.618621/pdf.

[62] E. Chernyavskiy, "Junction termination extension (JTE) with variation lateral doping (VLD) optimization method", 2016. arXiv: 1611.10352 [physics.ins-det].

[63] V. Temple, "Junction termination extension (jte), a new technique for increasing avalanche breakdown voltage and controlling surface electric fields in p-n junctions", in *1977 International Electron Devices Meeting*, 1977, pp. 423–426. DOI: `10.1109/IEDM.1977.189277`.

[64] N. Cartiglia, *The effect of temperature and irradiation on the lgad gain mechanism*, 2019. [Online]. Available: `https://indico.cern.ch/event/812761/contributions/3459057/attachments/1860679/3062357/Effect_of_temperature_and_fluence.pdf`.

[65] J. Deutsch, "Development and characterization of novel lgad sensors for the next generation of detectors", 2022.

[66] J. R. Janesick, *Photon Transfer Curve*. Aug. 2007, pp. 49–78. [Online]. Available: `https://doi.org/10.1117/3.725073.ch5`.

[67] P. Kennedy, *Calculating quantum efficiency - Ibsen Photonics*, Feb. 2022. [Online]. Available: `https://ibsen.com/resources/detector-resources/calculating-quantum-efficiency/`.

[68] M. Caselle, S. Chilingaryan, A. Herth, *et al.*, "Ultrafast Streaming Camera Platform for Scientific Applications", *IEEE Transactions on Nuclear Science*, vol. 60, no. 5, pp. 3669–3677, Jun. 2012. [Online]. Available: `https://doi.org/10.1109/tns.2013.2252528`.

[69] M. M. Patil, M. Caselle, L. Rota, *et al.*, "Novel p-in-n si-sensor technology for high resolution and high repetition-rate experiments at accelerator facilities", in *Topical Workshop on Electronics for Particle Physics (TWEPP2018) - Posters: 17-21 September 2018, Antwerp, Belgium*, (Antwerp, Belgium, Sep. 17–21, 2018), ser. Proceedings of Science (PoS), 54.01.01; LK 01, vol. 343, 2019. DOI: `10.22323/1.343.0045`.

[70] M. M. Patil, M. Caselle, E. Bründermann, *et al.*, "An ultra-fast and wide-spectrum linear array detector for high repetition rate and pulsed experiments", in *Proceedings of the 10th International Particle Accelerator Conference (IPAC 2019), Melbourne, AUS, May 10-24, 2019. Ed.: M. Boland*, (Melbourne, Australia, May 19–24, 2019), 54.01.01; LK 01,

JACoW Publishing, 2019, pp. 2504–2506, ISBN: 978-3-95450-208-0. DOI: `10.18429/JACoW-IPAC2019-WEPGW018`.

[71] A. Mozzanica, A. Bergamaschi, R. Dinapoli, *et al.*, "The GOTTHARD charge integrating readout detector: design and characterization", *Journal of Instrumentation*, vol. 7, no. 01, p. C01019, Jan. 2012. [Online]. Available: `https://doi.org/10.1088/1748-0221/7/01/c01019`.

[72] L. Rota, M. Vogelgesang, L. A. Perez, *et al.*, "A high-throughput readout architecture based on PCI-Express Gen3 and DirectGMA technology", *Journal of Instrumentation*, Feb. 2016. [Online]. Available: `https://doi.org/10.1088/1748-0221/11/02/p02007`.

[73] L. Rota, M. Caselle, S. Chilingaryan, *et al.*, "A PCIe DMA Architecture for Multi-Gigabyte Per Second Data Transmission", *IEEE Transactions on Nuclear Science*, vol. 62, no. 3, pp. 972–976, May 2015. [Online]. Available: `https://doi.org/10.1109/tns.2015.2426877`.

[74] M. M. Patil, E. Bründermann, M. Caselle, *et al.*, "Ultra-fast line-camera kalypso for fs-laser-based electron beam diagnostics", in *Proc. IBIC'21. Ed.: C. Kim*, (Online, Sep. 13–17, 2021), ser. International Beam Instrumentation Conference, 54.11.11; LK 01, JACoW Publishing, 2021, pp. 1–6, ISBN: 978-3-9545023-0-1. DOI: `10.18429/JACoW-IBIC2021-MOOB01`.

[75] M. G. Minty and F. Zimmermann, "Measurement and Control of Charged Particle Beams", *Particle Acceleration and Detection*, 2003. [Online]. Available: `http://dx.doi.org/10.1007/978-3-662-08581-3`.

[76] M. M. Patil, M. Caselle, G. Niehues, *et al.*, "Application of kalypso as a diagnostic tool for beam and spectral analysis", in *12th International Particle Accelerator Conference : virtual edition, May 24th-28th, 2021, Brazil : proceedings volume / IPAC2021. Ed.: R. Picoreti*, (Online, May 24–28, 2021), 54.11.11; LK 01, JACoW Publishing, 2021, pp. 3451–3454, ISBN: 978-3-95450-214-1. DOI: `10.18429/JACoW-IPAC2021-WEPAB331`.

[77] M. M. Patil, E. Bründermann, M. Caselle, *et al.*, "Modern ultra-fast detectors for online beam diagnostics", in *12th International Particle Accelerator Conference : virtual edition, May 24th-28th, 2021, Brazil :*

proceedings volume / IPAC2021. Ed.: R. Picoreti, (Online, May 24–28, 2021), 54.11.11; LK 01, JACoW Publishing, 2021, pp. 4540–4544, ISBN: 978-3-95450-214-1. DOI: `10.18429/JACoW-IPAC2021-FRXC03`.

[78] M. M. Patil, E. Bründermann, M. Caselle, *et al.*, "Status and upgrade of the visible light diagnostics port for energy spread measurements at kara", in *Proc. IPAC'23*, (Venice, Italy), ser. IPAC'23 - 14th International Particle Accelerator Conference, JACoW Publishing, Geneva, Switzerland, May 2023, pp. 4764–4767, ISBN: 978-3-95450-231-8. DOI: `10.18429/JACoW-IPAC2023-THPL123`. [Online]. Available: `https://indico.jacow.org/event/41/contributions/2526`.

[79] J. L. Steinmann, "Diagnostics of short electron bunches with thz detectors in particle accelerators", 54.01.01; LK 01, PhD thesis, Karlsruher Institut für Technologie (KIT), 2019, 226 pp., ISBN: 978-3-7315-0889-2. DOI: `10.5445/KSP/1000090017`.

[80] M. Brosi, "In-depth analysis of the micro-bunching characteristics in single and multi-bunch operation at kara", 54.01.01; LK 01, PhD thesis, Karlsruhe Institute of Technology (KIT), 2020, 198 pp. DOI: `10.5445/IR/1000120018`.

[81] P. Schreiber, "Negative momentum compaction operation and its effect on the beam dynamics at the accelerator test facility kara", PhD thesis, Karlsruhe Institute of Technology (KIT), 2022, 131 pp. DOI: `10.5445/IR/1000148354`.

[82] M. Brosi, J. Steinmann, E. Blomley, *et al.*, "Fast mapping of terahertz bursting thresholds and characteristics at synchrotron light sources", *Physical review accelerators and beams*, Nov. 2016. [Online]. Available: `https://doi.org/10.1103/physrevaccelbeams.19.110701`.

[83] P. Schreiber *et al.*, "Status of Operation With Negative Momentum Compaction at KARA", in *Proc. 10th International Particle Accelerator Conference (IPAC'19), Melbourne, Australia, 19-24 May 2019*, (Melbourne, Australia), ser. International Particle Accelerator Conference, Geneva, Switzerland: JACoW Publishing, Jun. 2019, pp. 878–881, ISBN:

978-3-95450-208-0. [Online]. Available: http://jacow.org/ipac2019/papers/mopts017.pdf.

[84]   P. Schreiber, T. Boltz, M. Brosi, *et al.*, "Effect of Negative Momentum Compaction Operation on the Current-Dependent Bunch Length", in *Proc. IPAC'21*, (Campinas, SP, Brazil), ser. International Particle Accelerator Conference, JACoW Publishing, Geneva, Switzerland, Aug. 2021, pp. 2786–2789, ISBN: 978-3-95450-214-1. [Online]. Available: https://jacow.org/ipac2021/papers/wepab083.pdf.

[85]   M. Labat, A. Bence, E. Bründermann, *et al.*, "Fast measurements of the electron beam transverse size and position on soleil storage ring", in *Proc. IBIC'21. Ed.: C. Kim*, (Online, Sep. 13–17, 2021), ser. International Beam Instrumentation Conference, 54.11.11; LK 01, JACoW Publishing, 2021, pp. 235–238, ISBN: 978-3-9545023-0-1. DOI: 10.18429/JACoW-IBIC2021-TUPP17.

[86]   K. Will, *Physics of Particle Accelerators and Synchrotron Radiation Sources: An Introduction (English Edition)*, 1992nd ed. Vieweg+Teubner Verlag, 1992.

[87]   A. Borysenko, N. Hiller, A.-S. Müller, *et al.*, "Electron Bunch Shape Measurements Using Electro-optical Spectral Decoding", *Physics Procedia*, vol. 77, pp. 3–8, 2015. DOI: 10.1016/j.phpro.2015.11.002.

[88]   R. H. Helm, M. J. Lee, P. L. Morton, *et al.*, "Evaluation of synchrotron radiation integrals", *IEEE Transactions on Nuclear Science*, vol. 20, no. 3, pp. 900–901, 1973. DOI: 10.1109/TNS.1973.4327284.

Datasheets and online documents

[89]   Andor Oxford Instruments. (2020). iDus 1.7m InGaAs - Andor, [Online]. Available: https://andor.oxinst.com/products/idus-spectroscopy-cameras/idus-1-7-ingaas.

[90] Avantes. (Nov. 2020). AvaSpec-NIR256/512-1.7-HSC-EVO, [Online]. Available: https://www.avantes.com/products/spectrometers/nirline/avaspec-nir256-512-1-7-hsc-evo/.

[91] Teledyne Technologies. (2023). Piranha4 | Teledyne DALSA, [Online]. Available: http://www.teledynedalsa.com/en/products/imaging/cameras/piranha4/.

[92] Xenics. (Jul. 2020). Short-Wave Infrared Imagers, [Online]. Available: https://www.xenics.com/short-wave-infrared-imagers/.

[93] Hamamatsu Photonics. (2020). Streak camera - hamamatsu photonics, [Online]. Available: https://www.hamamatsu.com/us/en/product/photometry-systems/streak-camera.html.

[94] Poul Riis. (2023). Gamma interaction, [Online]. Available: https://texample.net/tikz/examples/gamma-interaction/.

[95] J. H. Hubbell and S. E. Seltzer, "XCOM : Photon Cross Sections Database", Jun. 2023. [Online]. Available: https://ci.nii.ac.jp/naid/20000797424/.

[96] Synopsys. (2018). Tcad - technology computer aided design (tcad) | synopsys, [Online]. Available: https://www.synopsys.com/silicon/tcad.html.

[97] Weightfield2. (2018). Weightfield2: a freeware 2D simulator for silicon and diamond detector, [Online]. Available: http://personalpages.to.infn.it/~cartigli/Weightfield2/index.html.

[98] Edmund Optics. (2022). Advanced illumination led backlights: Edmund optics, [Online]. Available: https://www.edmundoptics.com/f/advanced-illumination-led-backlights/14058/.

[99] Infrared. (Feb. 2021). PbS PbSe Arrays - Infrared Materials Inc., [Online]. Available: https://infraredmaterials.com/pbs-pbse-arrays/.

[100] Trinamix. (2021). Trinamix ir detectors | line array / trinamix, [Online]. Available: https://trinamixsensing.com/ir-detectors/ir-detectors-overview/line-array/.

[101] Dow. (Oct. 2023). SYLGARD 186 Silicone Elastomer, [Online]. Available: https://www.dow.com/documents/en-us/productdatasheet/11/11-12/11-1253-sylgard-186-silicone-elastomer.pdf.

[102] Texas Instruments. (2020). ADS52J90 data sheet, product information and support | TI.com, [Online]. Available: https://www.ti.com/product/ADS52J90.

[103] Analog devices. (2020). Jesd204b survival guide - analog devices, [Online]. Available: https://www.analog.com/media/en/technical-documentation/technical-articles/JESD204B-Survival-Guide.pdf.

[104] PyQt. (2020). Pyqt reference guide, [Online]. Available: http://www.riverbankcomputing.com/static/Docs/PyQt4.

[105] PyQtGraph. (2020). Scientific graphics and gui library for python, [Online]. Available: http://www.pyqtgraph.org/.

Own Publications

[69] M. M. Patil, M. Caselle, L. Rota, *et al.*, "Novel p-in-n si-sensor technology for high resolution and high repetition-rate experiments at accelerator facilities", in *Topical Workshop on Electronics for Particle Physics (TWEPP2018) - Posters: 17-21 September 2018, Antwerp, Belgium*, (Antwerp, Belgium, Sep. 17–21, 2018), ser. Proceedings of Science (PoS), 54.01.01; LK 01, vol. 343, 2019. DOI: 10.22323/1.343.0045.

[70] M. M. Patil, M. Caselle, E. Bründermann, *et al.*, "An ultra-fast and wide-spectrum linear array detector for high repetition rate and pulsed experiments", in *Proceedings of the 10th International Particle Accelerator Conference (IPAC 2019), Melbourne, AUS, May 10-24, 2019. Ed.: M. Boland*, (Melbourne, Australia, May 19–24, 2019), 54.01.01; LK 01, JACoW Publishing, 2019, pp. 2504–2506, ISBN: 978-3-95450-208-0. DOI: 10.18429/JACoW-IPAC2019-WEPGW018.

[74] M. M. Patil, E. Bründermann, M. Caselle, *et al.*, "Ultra-fast line-camera kalypso for fs-laser-based electron beam diagnostics", in *Proc. IBIC'21. Ed.: C. Kim*, (Online, Sep. 13–17, 2021), ser. International Beam Instrumentation Conference, 54.11.11; LK 01, JACoW Publishing, 2021, pp. 1–6, ISBN: 978-3-9545023-0-1. DOI: 10.18429/JACoW-IBIC2021-MOOB01.

[76] M. M. Patil, M. Caselle, G. Niehues, *et al.*, "Application of kalypso as a diagnostic tool for beam and spectral analysis", in *12th International Particle Accelerator Conference : virtual edition, May 24th-28th, 2021, Brazil : proceedings volume / IPAC2021. Ed.: R. Picoreti*, (Online, May 24–28, 2021), 54.11.11; LK 01, JACoW Publishing, 2021, pp. 3451–3454, ISBN: 978-3-95450-214-1. DOI: 10.18429/JACoW-IPAC2021-WEPAB331.

[77]   M. M. Patil, E. Bründermann, M. Caselle, *et al.*, "Modern ultra-fast detectors for online beam diagnostics", in *12th International Particle Accelerator Conference : virtual edition, May 24th-28th, 2021, Brazil : proceedings volume / IPAC2021. Ed.: R. Picoreti*, (Online, May 24–28, 2021), 54.11.11; LK 01, JACoW Publishing, 2021, pp. 4540–4544, ISBN: 978-3-95450-214-1. DOI: `10.18429/JACoW-IPAC2021-FRXC03`.

[78]   M. M. Patil, E. Bründermann, M. Caselle, *et al.*, "Status and upgrade of the visible light diagnostics port for energy spread measurements at kara", in *Proc. IPAC'23*, (Venice, Italy), ser. IPAC'23 - 14th International Particle Accelerator Conference, JACoW Publishing, Geneva, Switzerland, May 2023, pp. 4764–4767, ISBN: 978-3-95450-231-8. DOI: `10.18429/JACoW-IPAC2023-THPL123`. [Online]. Available: `https://indico.jacow.org/event/41/contributions/2526`.